Energetic Ions at Earth's Quasi-Parallel Bow Shock

Dissertation
der Fakultät für Geowissenschaften
der Ludwig-Maximilians-Universität
zur Erlangung des Grades eines Doktors
der Naturwissenschaften

vorgelegt von
Arpad Kis
aus Klausenburg (Cluj, Rumänien)

16. September 2005

1. Gutachter: Prof. Dr. M. Scholer

2. Gutachter: Prof. Dr. R. Treumann

Tag der mündlichen Prüfung: 18. November 2005

to my Family

Contents

Chapter 1

Introduction

1.1 Collisionless Shocks

1.1.1 About Shocks in General

The everyday notions about shock waves originate in our knowledge and experience related to supersonic airplanes and blasts of explosion. In an ordinary gas the collisions between the gas particles transfer the momentum and energy, and allow the sound wave to exist. The sound wave propagation through a medium is an adiabatic process. After the sound wave has passed, the medium (the gas) regains its original state since the process is reversible. The velocity of the sound wave is determined by the parameters of the medium (i.e., density and pressure).

On the other hand, when a disturbance (an object or a blast wave for example) travels through the medium with a velocity larger than the speed of the sound, a shock wave is generated. A shock wave differs significantly from the sound wave because it affects the medium irreversibly. Every shock wave rises the temperature and density of the medium, while the supersonic flow is decelerated to subsonic flow regarded from the frame of the shock

wave.

The study of shock waves began at the end of the nineteenth century with gas dynamics. In the 1940's the understanding of shock waves improved substantially when the aircraft jet engine was developed. Interest in fusion plasmas and (thermo)nuclear explosions in the upper atmosphere during the 1950's gave new impulse to shock wave research.

Later, when spacecraft were developed, the study of the space surrounding our planet became possible by means of in-situ measurements. It was discovered that the interplanetary space is dominated by a magnetized, tenuous, high-velocity plasma flow: the solar wind. The solar wind is a neutral mixture of dissociated electrons and nucleii (mostly protons). Because of its very low density, direct collisions between the particles are extremely rare. This kind of plasma, as the solar wind, is called *collisionless plasma*.

The discovery of the Earth's bow shock (Ness et al., 1964) demonstrated that shock waves can exist in collisionless plasmas. When the supersonic solar wind reaches the Earth's magnetosphere (i.e., a magnetic cavity in the interplanetary space, which is dominated by Earth's magnetic field), a shock wave, the bow shock is formed. The bow shock slows down the solar wind to subsonic speed, while the plasma is heated and its density and the magnetic field magnitude increases. Since the solar wind flow is continuous, the Earth's bow shock is a "standing" shock wave regarded from our planet.

The main challenge posed by the existence of a collisionless bow shock is to understand how the dissipation takes place in a practically collision-free medium, i.e., where the mean free path for Coulomb collisions is larger than the size of the system. Other planets in the solar system were also reached by spacecraft and the existence of bow shocks in front of these planets was demonstrated. The shocks, however, are not limited to the solar system, since the Universe is dominated by plasma flows. Wherever there are plasma flows, there are also shock waves. Supernovae explosions also produce shocks.

A hot topic these days is the heliospheric termination shock, where the solar wind meets the interstellar medium. There is now increasing evidence that Voyager reached the termination shock in 2004.

Collisionless shocks have their scientific importance in their own right, but also because they are involved in a very wide range of phenomena. In addition, collisionless shocks are known to accelerate ions to high energies.
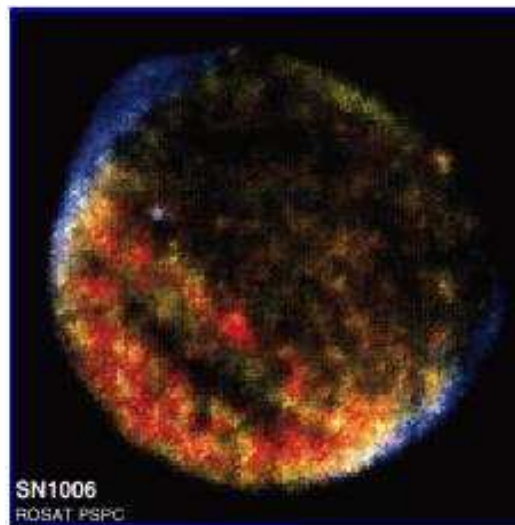
SUPERNOVAE
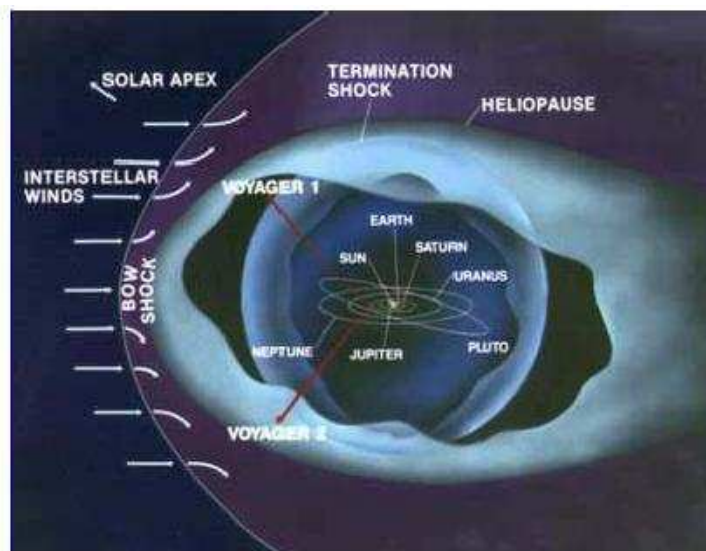
TERMINATION SHOCK

Figure 1.1: Shock waves can be found anywhere in the Universe: from the remote and exotic location of a novae explosion to the close vicinity of our home planet shocks are common phenomena. The top figure shows the X-ray image of supernova SN1006 (ROSAT PSPC image). The lower figure shows an artist's conception of the solar system and its boundary region, where the termination shock is.
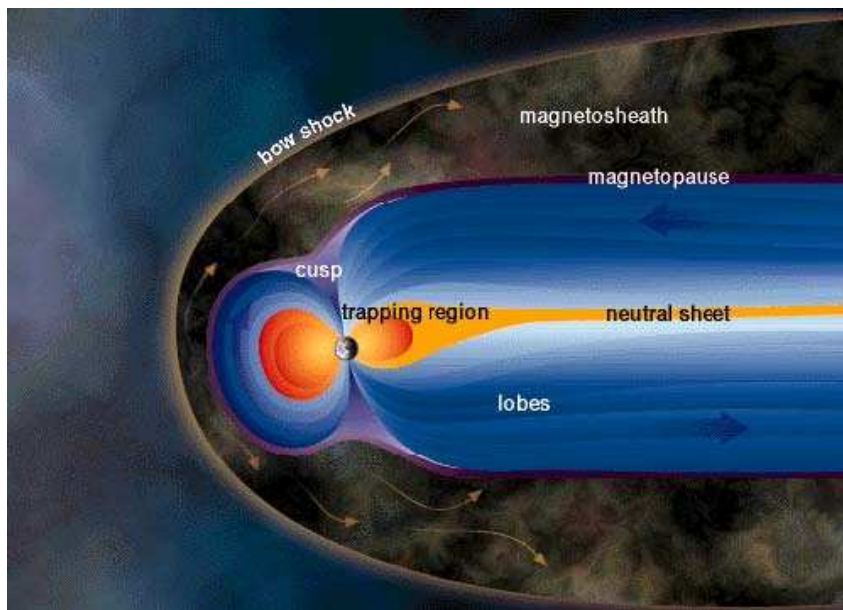
Figure 1.2: A schematical picture of Earth's bow shock and magnetosphere. As the solar wind plasma encounters the terrestrial magnetosphere a shock wave is generated. At the shock the solar wind is decelerated to subsonic velocity. The plasma is heated and compressed, while the magnetic field magnitude increases.

1.1.2 The Earth's Bow Shock and its Foreshock Region

The Earth's bow shock is a natural laboratory where the physics of collisionless plasma can be investigated under ideal conditions. The conditions are ideal because the bow shock is always present and its distance from the Earth's center at the subsolar point is ~ 15 R_e (where R_e is the Earth radius; $1R_e$=6370 km). This distance can be relatively easily reached by spacecraft orbiting around the Earth. Therefore we can accumulate enough data about the plasma and the electromagnetic fields at the bow shock to investigate it in detail. Since the laws of physics are valid all over the Universe, the understanding of processes at the Earth's bow shock can help us to understand processes in regions unavailable for direct (i.e., in-situ) measurements.

Because of its scientific importance the Earth's bow shock is the most intensively studied nonlinear wave. Despite the fact that it has been under investigation for more than three decades and a substantial amount of data and knowledge has been gathered, there are still unanswered fundamental questions. One of these questions is related to the ability of the bow shock to accelerate particles. The exact mechanism of how the ions are accelerated, and which ions are involved in the acceleration process is not fully understood. The goal of this thesis is to contribute to the understanding of ion acceleration processes at Earth's bow shock.

Even at an early stage of bow shock investigation it became clear that the shock encounters fall into two groups. In one group the shock encounters were identified as clean, localized, well defined transitions between the upstream and downstream regions. (The term upstream refers to the supersonic plasma, while the term downstream refers to the slowed, heated and shocked turbulent plasma state.) Sometimes shock transitions presented a turbulent and noisy appearance, characterized by the presence of large amplitude magnetic fluctuations (e.g. Fairfield, 1969; Greenstadt et al., 1970a,b) which made it difficult to identify a well defined transition between downstream and

upstream regions. A correlation was found between the two appearances and the Θ_{BN} angle (i.e. the angle between the shock surface normal direction and the magnetic field direction). Results showed that a quasi-parallel shock (i.e. when $\Theta_{BN} \leq 45°$) presents an extended, turbulent transition, while a quasi-perpendicular shock (i.e. when $\Theta_{BN} \geq 45°$) shows a clean, localized jump of plasma parameters between the upstream and downstream regions (Fairfield, 1974). Because of its clean structure most of the researchers focused their efforts on the quasi-perpendicular shock, while the quasi-parallel shock became a hostage of its complexity (Greenstadt, 1985).

Figure 1.3 presents the geometrical configuration of the region in front of the bow shock in the GSE (Geocentric Solar Ecliptic) coordinate system. The GSE coordinate system has its x axis pointing from Earth towards the Sun, its y axis is chosen to be in the ecliptic plane pointing towards dusk (thus opposing planetary motion). Its z axis is parallel to the ecliptic pole. Relative to an inertial system, this has a yearly rotation.

Because of the bow shock curvature, the quasi-parallel and the quasi-perpendicular shocks are simultaneously present, independent of the interplanetary magnetic field direction. The region of space upstream of the bow shock, magnetically connected to the shock and filled with particles backstreaming from the shock is known as the foreshock (1.3).
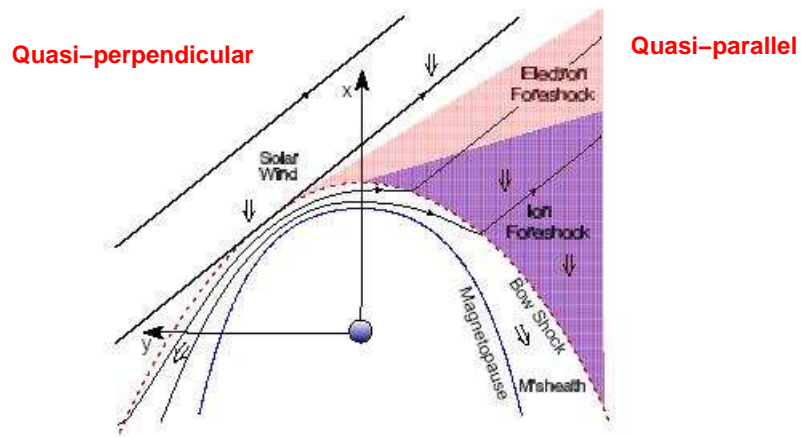
Figure 1.3: The most common geometrical structure of the region in front of the Earth's bow shock in the GSE (Geocentric Solar Ecliptic coordinate system) x-y plane. The x axis points to the Sun, while the y axis is in the ecliptic plane. Both types of shocks are present simultaneously.

Before discussing in detail the foreshock region, we need to introduce a few concepts related to ion motion in a magnetic field.

In a homogenous electromagnetic field the ion motion is determined by the Lorentz force (in the following we use SI units):

$$\vec{F}_L = q(\vec{E} + \vec{v} \times \vec{B}) \tag{1.1}$$

where $\vec{F}_L$ is the Lorentz force, q is the ion charge, $\vec{v}$ is the ion velocity, $\vec{E}$ and $\vec{B}$ are the electric and magnetic fields, respectively.
The conductivity of a plasma is very high. Therefore the electric field vanishes, i.e. $\vec{E}=0$. The ion velocity ($\vec{v}$) has two components, one component is parallel, the other is perpendicular to the magnetic field:

$$\vec{v} = \vec{v_{\parallel}} + \vec{v_{\perp}} \tag{1.2}$$

where $\vec{v_{\parallel}}$ is the parallel and $\vec{v_{\perp}}$ is the perpendicular component. Taking into consideration $\vec{E}=0$ and Equation 1.2, the Lorentz force can be written as:

$$\vec{F}_L = q((\vec{v_{\parallel}} + \vec{v_{\perp}}) \times \vec{B}) \tag{1.3}$$

where

$$\vec{v_{\parallel}} \times \vec{B} = 0 \tag{1.4}$$

Solving this, we find that the ion gyrates around the magnetic field line with a radius

$$r_L = \frac{mv_{\perp}}{qB} \tag{1.5}$$

where r_L is the Larmor radius and B is the magnetic field magnitude. In addition, the ion can move parallel to the magnetic field with $v_{\parallel}$. The combination of the two movements results in a helicoidal trajectory around the magnetic field line while the absolut velocity of the ion remains constant.

An important parameter of the ion movement is the pitch angle, the angle between the magnetic field direction and the ion velocity vector:

$$\tan\alpha = \frac{v_\perp}{v_\parallel} \qquad (1.6)$$

where α is the pitch angle. The pitch angle shows the ratio of the velocity components perpendicular and parallel to the magnetic field.

In order to understand the ion processes in the foreshock region, we need to introduce the concept of the frozen-in magnetic field. In a plasma with very high conductivity the magnetic field is swept away by the plasma flow; the magnetic field is "frozen-in" in the plasma. This concept can be applied to the solar wind: the interplanetary magnetic field is carried away by the supersonic plasma flow. As a result, the ions move on a helicoidal trajectory around the magnetic field while the magnetic field is convected by the solar wind.

First observations of energetic ions with energies up to 30 keV in the upstream region of Earth's bow shock were reported by Asbridge et al. (1968) based on Vela instrument data and later by Lin et al. (1974) based on IMP 6 measurements. Since then, energetic ions, ranging from just above the solar wind energy ($\sim$ 2 keV) to about 300 keV, have been under investigation for more than three decades. It has been established that the energetic ions in the region upstream of Earth's bow shock can be divided in two distinct groups according to their source of origin: the magnetospheric bursts and the bow shock associated particles. Sarris et al. (1976, 1978) and Krimigis et al. (1978) demonstrated that particles with energies above 300 keV are of magnetospheric origin. Scholer et al. (1981) showed that sometimes lower energy ions may also escape into the upstream region. With the ISEE-1/3 (International Sun-Earth Explorers) missions considerable evidence has been accumulated that below 200 keV the bow shock itself is the major source of energetic ions (Gosling et al., 1978). Gosling et al. (1978) showed that

the bow shock associated ions can be divided into two different groups: the reflected and the diffuse ion populations. The reflected ions present the characteristics of a beam-like distribution, streaming away from the shock along the magnetic field lines, while the diffuse ion component is a generally more isotropic, broad, ring-like distribution with an upstream oriented bulk velocity in the solar wind frame. Scholer et al. (1980) demonstrated that at energies larger than 30 keV the bow shock related particles in general belong to the high energy tail of the diffuse ion component. Each energetic ion population has a number density of ∼1 % of the incoming solar wind number density (Bonifazi and Moreno, 1981). A third group of energetic ions has been identified, showing characteristics of a transitional ion distribution between beam and diffuse ions. This distribution of ions was called "intermediate".

It has been established that a fundamental role is played by solar wind ions reflected at the shock front on the quasi-perpendicular side. At high Mach number (the Mach number is the ratio of the solar wind bulk velocity to the Alfvén speed) shocks, i.e. $M_A \geq 3$ (typical of the Earth's bow shock), about 25% of the incident ions are specularly reflected at the shock. The exact fraction depends on upstream conditions (Paschmann and Sckopke, 1983; Wilkinson and Schwartz, 1990). These ions, due to the large Θ_{BN} value, gyrate in the immediate upstream region and pass downstream afterwards. On the downstream side they occupy a different region in the phase space than ions which were directly transmitted through the shock front (Gosling et al, 1982; Sckopke et al., 1983). A characteristic feature of the quasi-perpendicular shock is the distinctive foot-ramp overshoot in the magnetic field profile, which is also due to reflected-gyrating ions (Leroy et al.,1981, 1982; Leroy, 1983; Sckopke et al., 1983; Burgess et al., 1989).

The quasi-parallel side of the shock presents a far more complex structure. The collisionless nature of the plasma and the magnetic field orientation (i.e. Θ_{BN} less than 45°) allows, in principle, for the ions propagating in the up-

stream direction along the magnetic field to reach to large distances from the shock front. These ions affect the incoming solar wind plasma flow through a number of possible plasma instabilities and wave generation mechanisms, giving rise to the foreshock region. Therefore the foreshock region in front of a quasiparallel shock is a vast region dominated by different particle populations, ions and electrons, and a "zoo" of associated magnetohydrodynamic waves. The upstream edge of the foreshock is defined by the presence of high energy (tens of keV) field-aligned beams (Lin et al., 1974). These low-density (less than 1% of the incident solar wind) ion beams are most probably produced by shock-drift acceleration (Armstrong et al., 1985) out of the incoming solar wind ions at the quasi-perpendicular side of the bow shock. Lower-energy (few keV) field-aligned beams can be observed deeper in the foreshock region (Sonnerup, 1969). These contain in greater part reflected ions at the quasiperpendicular side of the shock with a velocity of roughly twice the solar wind bulk speed (in the solar wind frame). The lower-energy field-aligned beams excite low frequency monochromatic waves, which propagate in the upstream direction with Alfvén velocity and are convected by the faster solar wind flow. Another characteristic ion population, the diffuse ions, can be found even deeper in the foreshock region. These ions present a broad, nearly isotropic angular distribution in velocity space and their energy extend up to 200 keV (Scholer et al., 1979, Thomsen, 1985). Figure 1.4 shows the field-aligned and the diffuse ion distributions in velocity space.
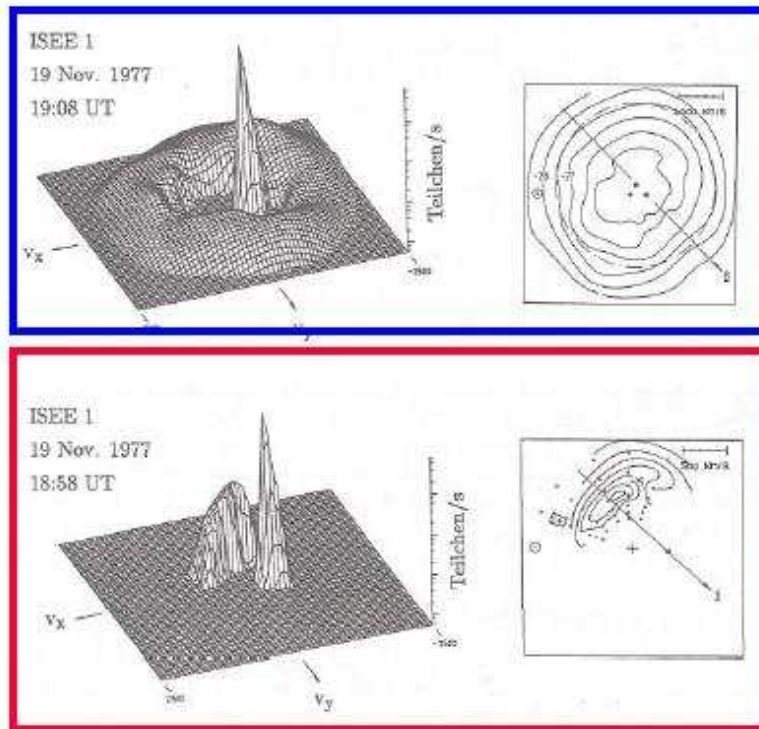
Figure 1.4: The figure shows the two distinctive ion distributions in velocity space which can be observed in the foreshock region. The lower panel is the distribution of a beam, while the upper panel presents the almost isotropic, broad, ring-like distribution of the diffuse ions. The "spike" in both panels around the middle of the velocity space represents the solar wind ion distribution.

1.2 The Cluster mission

1.2.1 Scientific Objectives of Cluster

Together with SOHO (Solar and Heliospheric Observatory), the Cluster mission form the first 'Cornerstone' of ESA's Horizon 2000 Programme, the Solar Terrestrial Science Programme (STSP). The interaction between the solar wind and the magnetosphere is the main element in the STSP. SOHO, located at the Lagrangian point 1, at ~ 240 R_e from the Earth in the sunward direction, records continuously the activity of the Sun, the solar wind, and the flux of high-energy particles in the energy range of ~ 100 keV to GeV (Domingo et al., 1995). Cluster, with its four identical spacecraft, was designed to study the physical processes involved in key regions of the near-Earth environment; i.e., at the bow shock, the polar cusp and the magnetotail. The main purpose of the Cluster mission is to investigate the plasma structures contained in the key regions. By using 4 spacecraft, it is possible for the first time to separate the spatial variation of the plasma parameters from the temporal evolution. In addition, the four spacecraft allow us to derive differential plasma quantities.

After the failure of the first launch and the destruction of Cluster in 1996, it was decided to rebuild the four spacecraft and to relaunch the Cluster mission. The rebuilt four spacecraft were launched by two Soyuz rockets on 16 July, 2000, and on 9 August, 2000. Each rocket carried two satellites. The orbit was designed to provide a tetrahedron formation between the four spacecraft. The start of the data phase was on 1 February, 2001.

The main goal of the Cluster mission is to investigate the small-scale plasma structures and their evolution in space and time in near-Earth regions as:

-the solar wind and the bow shock

-the magnetopause

-the polar cusp

-the magnetotail

-the auroral zone

(Escoubet et al., 1997)

1.2.2   Orbit and Separation Strategy

In order to meet the scientific objectives of the mission, the orbit with a perigee at $4R_e$, an apogee at $19.6R_e$ and an inclination of 90° was chosen. The orbital period is about 57 hours. The polar orbit is fixed in the interstellar coordinate system. Therefore as the Earth makes one orbit around the Sun, the Cluster spacecraft is able to "sweep" all regions of interest in 12 months. Figure 1.5 presents the Cluster orbit in the time period when the apogee is in the solar wind around local noon. As the Cluster spacecraft move along their orbit, the nominal tetrahedron formation changes according to the position at the trajectory. Special emphasis in terms of separation has been put on the northern cusp and the southern bow shock and magnetosphere. When the apogee is around local noon, the regions crossed are the nightside auroral zone, the northern cusp, the magnetopause, the bow shock, the solar wind, and then again the same regions in the southern hemisphere, in reverse order. At the northern cusp and at the southern bow shock and magnetopause a perfect tetrahedron is preserved. The advantage of this configuration is that throughout the solar wind and magnetopause the configuration stays close to a tetrahedron, while near to perigee the tetrahedron becomes elongated, and the spacecraft cross the auroral zone as a string of pearls. Figure 1.6 presents the concept of interspacecraft constellation during one orbit. The size of the tetrahedron (i.e., the separation distance of the Cluster spacecraft) can be changed during the mission. Thus different physical processes with different length scales can be investigated. Figure 1.7 presents the interspacecraft
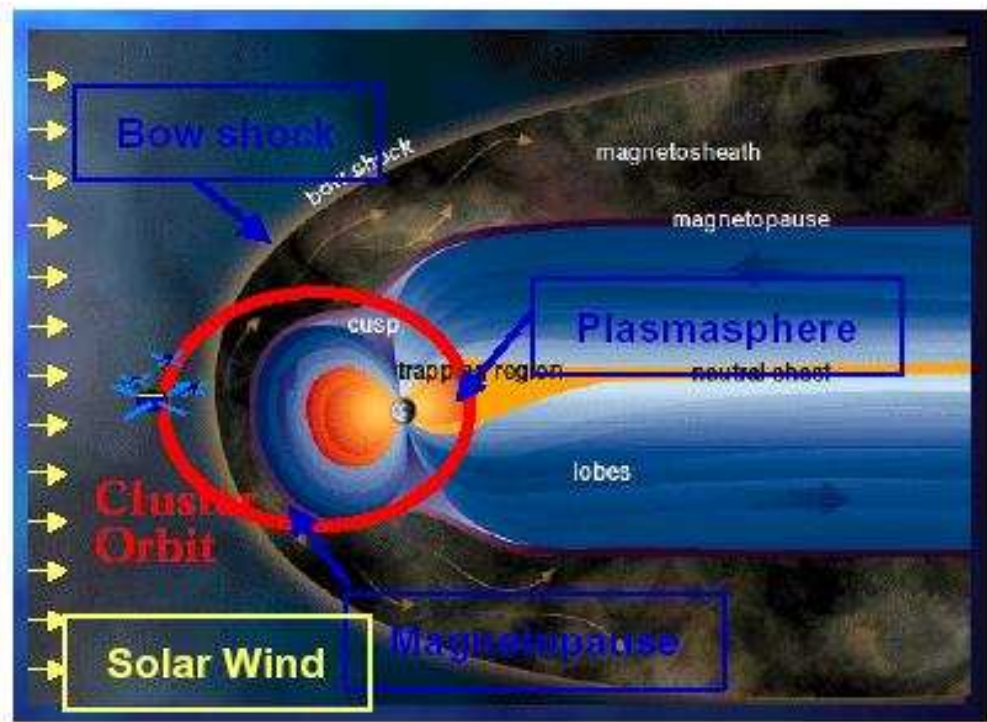
Figure 1.5: The figure shows the Cluster orbit when the apogee is in the solar wind around local noon.

separation distance between 2000 and 2005. This thesis focuses on the time period when the apogee was in the solar wind around the time of local noon with separation distances of $\sim 1 - 1.5$ R$_e$. These conditions are fullfilled between December 2002 and April 2003, the most favorable time period being around February-March, 2003.
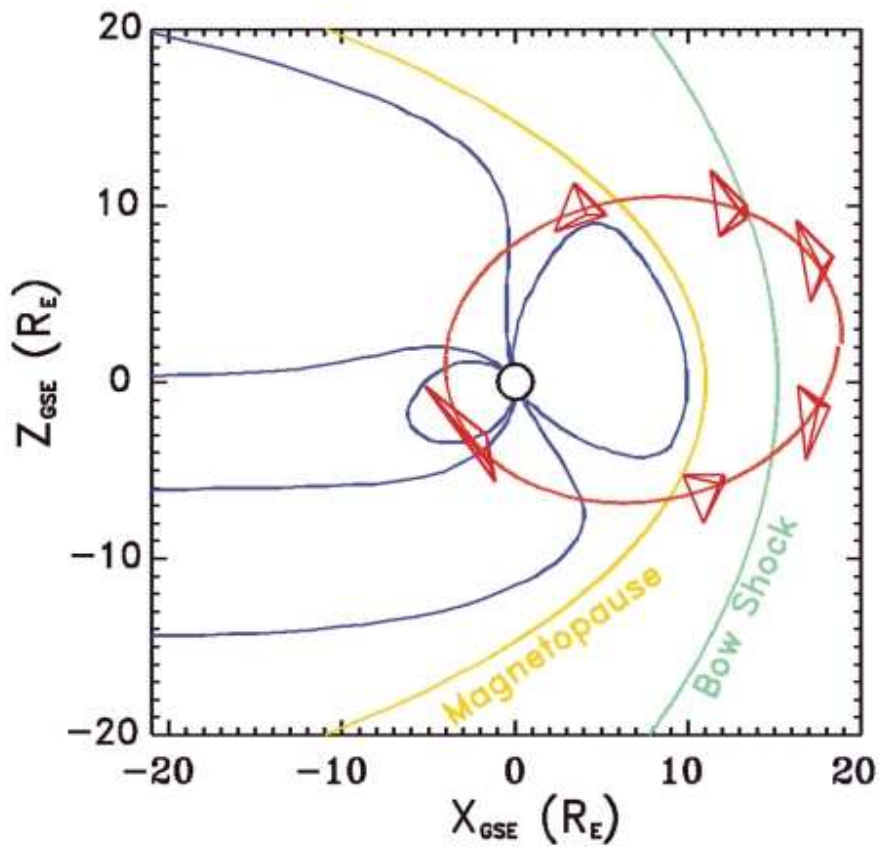
Figure 1.6: The changing of the Cluster nominal tetrahedron formation during one complete orbit. (The inter-spacecraft separation distance is magnified for better visibility.)
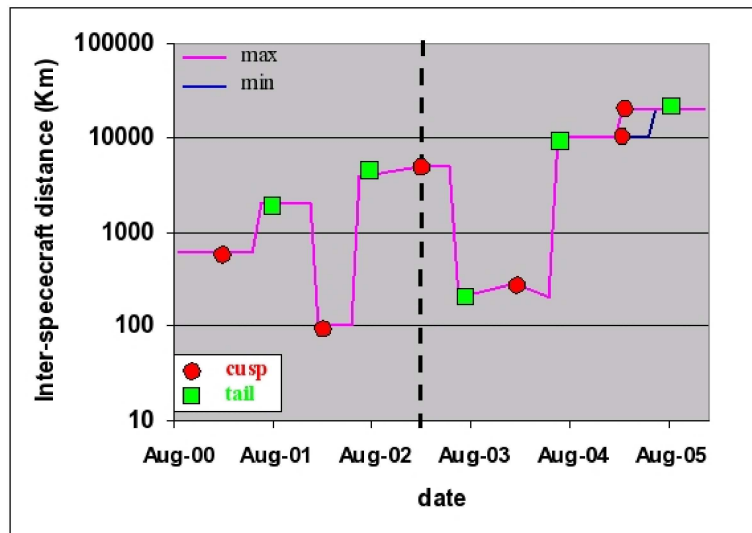
Figure 1.7: The Cluster nominal inter-spacecraft separation distance between 2000-2005. The flexibility in the tetrahedron scale allows the plasma processes to be studied on different spatial scales.

1.2.3 Scientific Objectives of this Thesis

This thesis focuses on the bow shock, in particular on energetic ion processes at the quasi-parallel side. For other topics under investigation see the Proceedings of the Cluster Workshop on Physical Measurements and Mission Oriented Theory (Mattok, 1995).

The state-of-the-art instrumentation of Cluster makes possible the measuring of the electromagnetic field and the electron and ion distributions with high resolution. A very important topic is the acceleration of ions at the bow shock, since the exact physical mechanism through which ions are able to reach high energies is not fully understood. With its multipoint measurements, Cluster is capable to provide new details about the energetic ion behavior in front of the bow shock, at the bow shock, and behind the shock in the magnetosheath. By using multispacecraft data, we are able to measure the energetic ion density at different distances from the bow shock simultaneously and separate the spatial evolution of these ions from the temporal evolution. Cluster provides high-resolution particle data which makes the detailed analysis of the different energetic ion populations as a function of distance from the bow shock possible. The high-resolution data might also help to answer the question of the origin of these energetic ions. In other words, where these ions come from and what makes them to be "picked out" from the ion population for further energization processes. By combining the particle data with the magnetic field measurements we are able to investigate the connection between the energetic ions and the associated magnetohydrodynamic waves.

1.3   Cluster Instruments

1.3.1   The Cluster Instrument Package

The four Cluster spacecraft are identical, each of them containing 11 instruments. In the following we provide a short description of each of the instruments.

(1) FGM. The FGM (Fluxgate Magnetometer) measures the magnetic field vector components. It consist of two, tri-axial fluxgate magnetometers and an on-board data processing unit on each spacecraft (Balogh et al. 1997). It has a high vector sample rate (up to 67 vectors s^{-1}) with a resolution of up to 8pT.

(2) STAFF. The STAFF (Spatio-Temporal Analysis of Field Fluctuations experiment) consists of a boom-mounted three-axis search coil magnetometer and two complementary data-analysis packages: a digital spectrum analyser and an on-board signal-processing unit. The latter permits the observation of the three magnetic waveforms up to either 10 Hz or 180 Hz, depending upon mode. The spectrum analyser also receives the signals from the four electric field probes of the EFW experiment, which are used to form a pair of orthogonal electric field dipole sensors. All five inputs are used to compute in real time the 5×5 Hermitean cross-spectral matrix at 27 frequencies distributed logarithmically in the frequency range 8 Hz to 4 kHz (Cornilleau-Wehrlin et al., 1997). The dynamic range is about 96 dB in both waveform and spectral power, so allowing for the study of waves near plasma boundaries.

(3) EFW. The EFW (Electric Field and Wave experiment) is designed to measure the electric field and density fluctuations with sampling rates up to 36000 samples s^{-1}. The sensor system of the instrument consists of four orthogonal cable booms carrying spherical sensors and are deployed to 50 m in the spin plane of the spacecraft. The potential differences between two opposite spherical sensors provide the average electric fields in two directions.

Among the most important scientific objects of the experiment are studies of nonlinear wave phenomena and large- and small-scale interferometric measurements. By using four spacecraft for large-scale differential measurements and several Langmuir probes on one spacecraft for small-scale interferometry, it becomes possible to study motion and shape of plasma structures in a wide range of spatial and temporal scales (Gustafsson et al., 1997).

(4) WHISPER. The WHISPER (Waves of HIgh frequency and Sounder for Probing of Electron density by Relaxation) sounder is primarily designed to provide an absolute measurement of the total plasma density within the range of 0.2-80 cm^{-3}. The principle of a relaxation sounder is similar to that of a classical radar flown in a plasma. Inside the active period of a frequency step a radio wave transmitter sends a wave train over a limited time period at a fixed frequency f. Such a burst will excite natural resonances of the plasma in the frequency range it covers. After this active period a radio receiver is connected to a double-sphere dipole electric sensor and listens to the signal around f. Then the process is repeated at a new frequency step. A succession of such steps constitutes a sweep, which allows the properties of the neighbouring plasma to be explored throughout the range of interest. In addition, the wave analysis function of the instrument is provided by FFT (Fast Fourier Transformation) calculation (Décréau et al., 1997).

(5) WBD. The WBD (Wide-Band) plasma wave investigation is designed to provide high-resolution measurements of both electric and magnetic fields in selected frequency bands from 25 Hz to 577 kHz. The instrument processes signals from the two electric antennas of the EFW and of the STAFF search coil magnetometer. The four selectable inputs consist of two electric-field signals (E_y and E_z) and two magnetic-field signals (B_x and B_y). Continuous waveforms are digitised and transmitted, while the recorded data are stored in the spacecraft solid-state recorder for later playback (Gurnett et al., 1997).

(6) DWP. Since the plasmas investigated by Cluster contain waves with

a frequency range from DC to over 100 kHz, it is essential that the on-board control system for the wave-experiment instruments to be flexible in order to make effective use of the limited spacecraft resources of power and telemetric bandwidth. This task is performed by the DWP (Digital Wave Processing experiment). The DWP instrument employs a novel architecture based on the use of transputers with parallel processing and re-allocatable tasks to provide a high-reliability system (Woolliscroft et al., 1997).

(7) EDI. The EDI (Electron Drift Instrument) measures the drift of a weak beam of test electrons emitted in certain directions. The basis of the electron drift technique is the injection of test electrons from a common source in a plane normal to the local magnetic field and the registration of their gyrocenter displacements after one or more gyrations in the magnetic field. This drift is related to the electric field and the gradient in the ambient magnetic field. Measurement of the beam displacement allows to determine the electric field perpendicular to the magnetic field. By use of different electron energies the magnetic field gradient can be determined separately (Paschmann et al., 1997).

(8) ASPOC. The floating potentials for magnetospheric satellites (typically from +1 to several tens of volts in sunlight) make it practically impossible to measure the cold (several eV) component of the ambient plasma. Effects of spacecraft charging are reduced by active charge neutralisation. In order to achive this, the Cluster spacecraft are instrumented with ASPOC (Active Spacecraft POtential Control), an ion emitter of the liquid-metal ion-source type, producing indium ions at 5 to 8 keV energy. The operating principle is field evaporation of indium in the apex field of a needle (Riedler et al., 1997).

(9) CIS. The CIS (Cluster Ion Spectrometry) experiment is a comprehensive ionic plasma spectrometry package capable of obtaining full three dimensional ion distributions with mass per charge composition determina-

tion (Rème et al., 2001). For a detailed description of the CIS experiment see the following section.

(10) PEACE. The PEACE (Plasma Electron And Current Experiment) experiment is an electron analyser to measure the three dimensional velocity distribution of electrons in the energy range from 0.59 eV to 26.4 keV. The instrument consists of two sensors with hemispherical electrostatic energy analysers with position-sensitive microchannel plate detectors. They are placed to view radially on opposite sides of the spacecraft. The dynamic range of the instrument is sufficient to provide accurate measurements of the main known electron populations from the tail to the plasmasheath and solar wind (Johnstone et al., 1997).

(11) RAPID. The RAPID (Research with Adaptive Particle Imaging Detectors) spectrometer is an advanced particle detector for the analysis of suprathermal plasma distributions in the energy range of 40 keV-1500 keV for hydrogen, and 10 keV nucl^{-1}-4000 keV for heavier ions (Wilken et al., 1997). The instrument uses two different and independent detector systems for the detection of nuclei and electrons. The Imaging Ion Mass Spectrometer (IIMS) determines energy and nuclear mass of incident ions or neutral atoms by a time-of-flight and energy measurement. Electrons with energies from 20-400 keV are measured with the novel Imaging Electron Spectrometer (IES) consisting of advanced microstrip solid-state detectors in combination with pin-hole acceptance.

All the investigations described in this thesis are based on ion data provided by the CIS instrument; in addition we also use magnetic field data provided by the FGM instrument.

1.3.2   CIS: the Plasma Instrument

The dynamic range of the differential plasma energy flux at different energies encountered by Cluster in the course of one year is presented in Figure 1.8. The wide range of differential energy flux values, varying from $\sim 10^3$ to $\sim 10^{10}$ $(\text{cm}^2\cdot\text{s}\cdot\text{sr})^{-1}$, requires a large dynamic range of the plasma experiment. This requirement is fulfilled by using two sensors with two different geometric factors in each sensor. These sensors are the time of flight ion COmposition and Distribution Function sensor (CODIF) and the Hot Ion Analyser (HIA).

CIS is capable of measuring both the hot and cold ion populations (for example ion beams) from the magnetosheath and solar wind with sufficient mass, angular and energy resolution in order to meet the scientific objectives (Escoubet et al., 1997). The instrument has a time resolution of 1 spin, i.e. 4 s. This time resolution is sufficiently high to follow flux or density fluctuations at the gyrofrequency of H^+ ions in a magnetic field of 7 nT or less, since the proton gyroperiod is about $\sim$10 s in a magnetic field of 7 nT.

The HIA instrument analyses incoming ions based on energy/charge by using electrostatic deflection in a quadrispherical, symmetrical analyser. The analyser has a uniform energy-angle response with a fast imaging particle detection system. The particle imaging uses microchannel plate (MCP) electron multipliers and position encoding discrete anodes. The symmetric quadrisphere, known also under the name of "top hat" geometry has been used previously with great success on many rocket flights and on several spacecraft (AMPTE/IRM, Giotto and WIND; Paschmann et al., 1985; Rème et al., 1987; Lin et al.,1995).

The HIA instrument has $2 \times 180°$ field of view (FOV) sections, situated in a parallel plane with the spin axis of the spacecraft. In order to cover the large dynamic range, the two FOV sections have different geometric factors, with a factor of $\sim$25 difference between the "high G" (high geometrical factor) and "low g" (low geometrical factor) sections. Figure 1.9 shows the cross-section
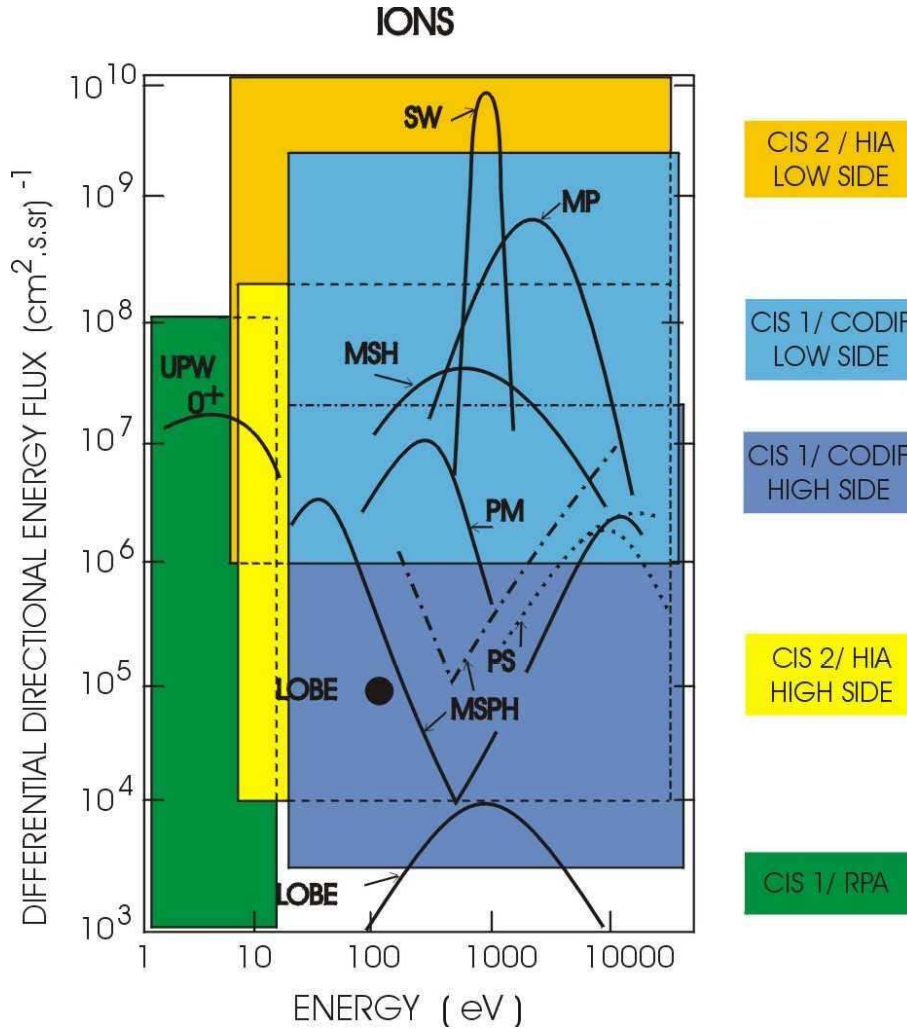
Figure 1.8: Typical ion fluxes encountered by Cluster spacecraft along its orbit. The abbreviations are: SW for solar wind, MP for the magnetopause, MSH for the magnetosheath, PM for the plasma mantle, MSPH for the magnetosphere, PS for the plasma sheath and UPW for the lobe and upwelling ions. The different colours represent the range of different sensitivities of CIS1/CODIF (Low Side, High Side and RPA, and CIS2/HIA (Low g and High G).
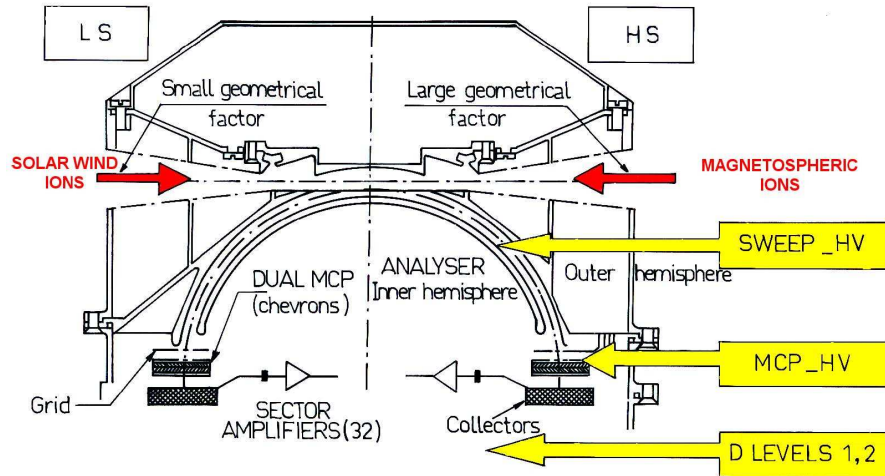
Figure 1.9: Cross section of the HIA analyser.

of the HIA analyser. The low g section (LS) makes possible the detection of the solar wind. The required high angular resolution in the polar direction is achieved through the use of $8 \times 5{,}625°$ central anodes, with the remaining 8 sectors having a $11.25°$ resolution. The high G section (HS) is divided into 16 anodes, $11.25°$ each sector. Figure 1.10 present the principle of the HIA anode sectoring.

A full description of the HIA experiment can be found in Rème et al., (2001). The energy range of HIA is 5 eV/e to 32 keV/e, with 64 energy sweeps per spin and logarithmic steps in energy. Thus, a 2D distribution is sampled every 62.5 milliseconds (i.e., $5.625°$ in azimuth) and a full 3D distribution is obtained every 4 seconds. The energy channel distance and wideness (i.e. in energy) is growing exponentially from the lowest energy to the highest, the analyser constant (i.e., the ratio between voltage and energy) being ~ 6.70.

The CODIF sensor provides compositional information of the most abun-
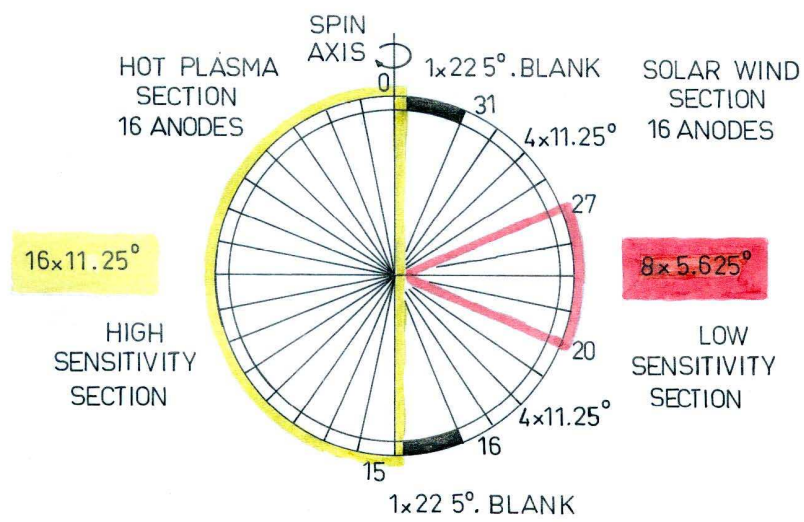
Figure 1.10: Principle of the HIA anode sectoring.

dant ions in the near-Earth environment, i.e., H^+, He^{++}, He^+ and O^+. CODIF is a mass per charge, high-sensitivity spectrometer, with a $360 \times 8°$ field of view (FOV), capable to measure the complete 3D distribution function of the major ion species during one spin. To adequately cover the large dynamic range encountered from the low-density plasma of the magnetotail to the dense plasma in the magnetosheath (see Figure 1.8), CODIF also utilizes two different geometric factors.

In order to compute the basic plasma parameters, the minimum number of counts in a distribution is about 100. The counts need to be accumulated over one spin in order to provide the necessary time resolution. On the other hand the maximum count rate which the time-of-flight (TOF) system is able to process is $\sim 4 \times 10^5$ counts per spin. This results in a dynamic range for one sensitivity (i.e., one geometric factor) of only 4×10^3. In order to extend the dynamic range to $\sim 10^5$, CODIF incorporates two geometric factors differing by a factor of ~ 100, each section with a $180°$ field of view. Figure 1.11 presents a cross section of the analyser. Basically the CODIF instrument utilises a combination of energy/charge selection by deflection in a rotationally symmetric toroidal electrostatic analyser with a subsequent time-of-flight (TOF) analysis after post-acceleration to ≥ 15 keV/e, covering the wide energy range between 0.02 and 38 keV/charge. The uniform response in the polar angle by the analyser is provided by a complete cylindrical symmetry. The full angular range of the analyser is divided into 16 channels of $22.5°$ each. An attenuation grid covers the entrance; the grid is kept at spacecraft ground. The grid is designed to provide a 1% transmission over half of the analyser entrance and more than 95% over the other half of the entrance. The high transmission portion covers the azimuthal angle range from $0°$ to $180°$. The active entrance of the low transmission part extends from $22.5°$ to $157.5°$ only, in order to avoid the counting of any crossover from the other, high transmission part. The apertures insure that there are

no gaps in the polar angle coverage. The analyser voltage varies between 1.9-4950 V which provides the detection of ions in the energy range of 15-38000 eV/e. The deflection voltage is varied in an equidistant logarithmic sweep, a full energy sweep (with 30 contiguous energy channels) is performed 32 times per spin. This way the full 3D ion distribution is obtained over a spacecraft spin cycle.

The continuous transmission of the complete 3D ion distributions sampled at the maximum temporal and angular resolution is impossible (limited downlink telemetry). To overcome this limitation, extensive on board data-processing is a very important aspect of the design. The system responsible for this part of the operation is the Data Processing System (DPS). The DPS controls the data collection of the two CIS (CODIF and HIA) instruments. It formats the data for the telemetry channel, receives and executes commands. The DPS is also the unit which analyses and compresses on board the immense quantity of data. The compressing is done in such a way to maximise the scientific return despite the limited CIS telemetry allocation. The DPS and the CODIF instrument are integrated in one box, CIS-1, while HIA is integrated in the CIS-2 box.
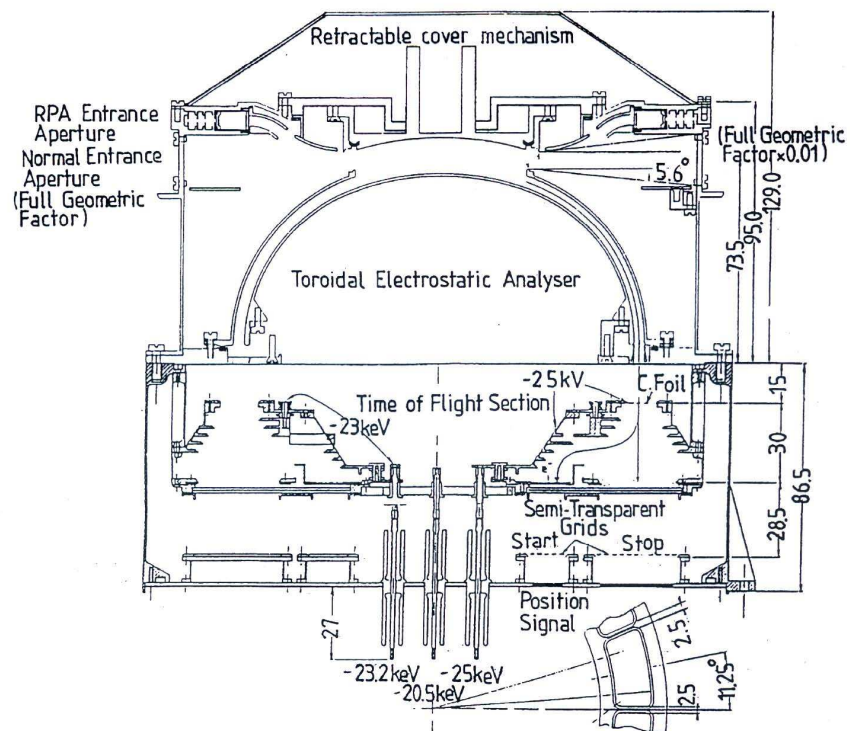
Figure 1.11: Cross-section of the CODIF sensor.

Chapter 2

Spatial Evolution of Diffuse Ion Density in Front of the Earth's Bow Shock

2.1   Introduction

We investigate the diffuse ion behavior in the region upstream of Earth's bow shock by using Cluster data. Cluster, with its multipoint measurement capability, provides ion data simultaneously at different distances from the bow shock. This way the spatial evolution of the diffuse ions can be separated from the temporal evolution.

The diffuse ions in the foreshock region are always observed together with low frequency magnetic waves; these waves were first reported by Fairfield (1969) using Explorer 34 data. Hoppe et al. (1981) demonstrated that there is a one-to-one correlation between the presence of low-frequency waves and diffuse ions in the upstream region, which led to the concept of an intensive interaction between the waves and energetic ions. The waves are thought to play the role of scattering centers for these particles, leading to

a diffusive transport and finally resulting in Fermi acceleration at the shock. The theoretical background for diffusive acceleration has been laid by Axford et al. (1977), Krimsky (1977), Blandford and Ostriker (1978); a detailed description of the diffusive acceleration can be found in reviews by Drury (1983), Scholer (1985) and Forman and Webb (1985).

In a self-consistent model of wave-particle interaction, Lee (1982) explicitly assumes that the magnetic waves are excited by the energetic particle population. Möbius et al. (1987) investigated a few selected upstream ion events and found that the relation between particle and wave energy density derived by Lee (1982) shows good correlation with observations. In general the models based on diffusive acceleration were able to successfully interpret different characteristics of the diffuse ions, such as the directional distribution, spectra and spatial ion distribution in front of the bow shock (Ipavich et al., 1981; Scholer et al., 1981). Despite their indisputable success, these theoretical models rely on additional assumptions. One such assumption is that in order to reproduce the spectral shape of energetic ions there has to be a particle loss. Two possible solutions were suggested: particle loss across a free escape boundary along the interplanetary magnetic field into the upstream direction (Ellison, 1981; Lee et al., 1981) or loss to the flanks of the magnetosphere by diffusion perpendicular to the magnetic field (Lee, 1982). An alternative to particle loss is the assumption of a finite time of connection of the solar wind convected magnetic field lines with the quasi-parallel side of the bow shock (Forman and Drury, 1983). Jokipii (1982) suggested a mechanism, where the shock drift acceleration contributes to the energization process. None of these proposed mechanisms have been proven or disproven by observations.

For the diffusive acceleration to work efficiently, the diffuse ions need to undergo pitch angle scattering without changing the energy of the particles, which leads to a diffusive transport. The signature of spatial diffusion is

that the energetic ion (i.e. diffuse ion) partial density falls off exponentially from the shock into the upstream region along the magnetic field. In order to prove that the diffuse ions truly undergo a diffusive transport, the spatial variation of the diffuse ion partial density needs to be determined. Ipavich et al. (1981) analyzed about 30 upstream ion events and found that the differential ion flux for the 33 keV ions falls off exponentially with distance from the shock. Trattner et al. (1994) extended the work by Ipavich et al. (1981) by performing a statistical analysis of ∼330 diffuse ion events in an energy range between 10 and 67 keV and found that the intensity of the upstream ions falls off exponentially with an e-folding distance between 3 and 11.7 R_e over the investigated energy range.

These studies indeed demonstrate the importance of diffusive transport, but because only one spacecraft was available, they had to be done on a statistical basis. The interplanetary conditions, such us the solar wind velocity and density can vary significantly from event to event, therefore a statistical study can only reveal the general characteristics and behavior of the upstream ions, and can not give detailed information about each particular event.

2.2 Measuring the Gradient of Diffuse Ion Partial Density

2.2.1 On the Importance of Multispacecraft Measurements

The statistical studies performed by Ipavich et al. (1981) and Trattner et al. (1994) resulted in clear evidence that the ions undergo a diffusive transport. These results provide the e-folding distance of the partial ion density in front

of the shock, its value varying between $\sim$2 and $\sim$11 R_e in the 10-67 keV energy range. These studies were based on statistical analysis of several upstream ion events, because one spacecraft can only observe the spatial *and* the temporal variation of the energetic ion density. It is known that the bow shock accelerated energetic ion density is directly correlated with the density of the solar wind (Trattner et al., 1994) and is presumed that the direction of the magnetic field is also an important factor in the production of energetic ions. Even a quiet solar wind presents low-amplitude fluctuations in the plasma density and in the interplanetary magnetic field strength and direction. These fluctuations constantly and instantly influence the energetic ion production and therefore the energetic ion density itself. The energetic ion density produced at the shock might exhibit fluctuations due to changes in the solar wind plasma parameters, therefore it is vital to have measurements at different distances from the shock at the same time. This is the only way how we can assure to separate the spatial variation in partial density of the energetic ions from the temporal one.

2.2.2   Determination of the Individual Spacecraft Distance to the Shock

To measure the distance of a spacecraft to the bow shock along the magnetic field line requires a precise calculation of the bow shock position under different interplanetary conditions. The bow shock position cannot be observed directly; the exact bow shock position can be observed only during spacecraft crossings. Many bow shock models have been developed and are widely used in scientific investigations since the early 1960's (for a complete list of references see Peredo et al., 1995).

A common conclusion of many of these investigations is that the bow shock formed upstream of the Earth is a highly dynamic boundary, which

is controlled by steady and transient variations in solar wind parameters. Therefore choosing the appropriate bow shock model is essential in order to make a correct calculation of the bow shock position. The model needs to incorporate the response to variations in Mach number, solar wind bulk velocity and solar wind density. Taking into account the previously listed requirements, the bow shock model by Peredo et al. (1995) has been chosen. Peredo et al. (1995) analyzed a large set of bow shock crossings (about 1400 events), revealing that among the three Mach numbers (i.e., sonic (M_s), Alfvénic (M_A) and magnetosonic (M_{ms}) Mach numbers) M_A controls the position of the bow shock much stronger than the other two. They derived a three dimensional model for the average shape and position of the bow shock under normalized solar wind conditions (see below).

The normalization takes into account variations of the bow shock position due to the solar wind dynamic pressure. Peredo et al. (1995) normalized all crossings to the average solar wind pressure of their data set according to the relation (e.g. Spreiter et al., 1966, 1968; Fairfield, 1971; Holzer and Slavin, 1978):

$$R_{norm} = R_{obs} \Big(\frac{n_{obs} V_{obs}^2}{n_{avg} V_{avg}^2} \Big)^{1/6} \tag{2.1}$$

where n_{obs}, V_{obs}, n_{avg}, V_{avg} are the observed and averaged solar wind number densities and bulk speeds, respectively. R_{norm} and R_{obs} are the normalised and observed bow shock distances at subsolar point. The average quantities for the Peredo data set are $n_{avg} = 7.76 \text{cm}^{-3}$ and $V_{avg} = 454.18 \text{km/s}$.

According to the Peredo model, the Earth's bow shock can be represented as a general second order surface which is described by the following expression:

$$F(x, y, z) = a_1 x^2 + a_2 y^2 + a_3 z^2 + a_4 xy + a_5 yz + a_6 xz + a_7 x + a_8 y + a_9 z + a_{10} = 0$$
(2.2)

where the x, y and z coordinates are obtained from the GSE (Geocentric Solar Ecliptic) system via transformation, and a_i coefficients are functions of the Alfvén Mach number (M_A):

$$a_1 = 0.0117 - 5.18 \times 10^{-3} M_A - 3.47 \times 10^{-4} M_A^2$$
(2.3)

$$a_3 = 0.712 + 0.044 M_A - 1.35 \times 10^{-3} M_A^2$$
(2.4)

$$a_4 = 0.3 - 0.071 M_A + 3.53 \times 10^{-3} M_A^2$$
(2.5)

$$a_7 = 62.8 - 2.05 M_A + 0.079 M_A^2$$
(2.6)

$$a_8 = -4.85 + 1.02 M_A - 0.048 M_A^2$$
(2.7)

$$a_{10} = -911.39 + 23.4 M_A - 0.86 M_A^2$$
(2.8)

and a_5, a_6 and a_9 are zero and the value of a_2 is one. Note that all the coefficients are determined only by the value of M_A. Horbury et al. (2001) analyzed the magnetic data during shock encounters by the four Cluster spacecraft and found the orientation of the terrestrial bow shock normal to be extremely stable, at least under steady upstream conditions. Furthermore, they point out that the agreement between normals estimated from the Peredo model and those based on four spacecraft magnetic data implies that

even when the shock moves rapidly, the bow shock shape proves to be remarkably stable. In conclusion, the Peredo model provides a three-dimensional bow shock model incorporating the variations of the shock surface shape under different Mach number conditions, which in turn according to Horbury et al. (2001) is extremely accurate and stable even under dynamically changing interplanetary conditions. This makes the Peredo model reliable for the gradient study. However, like any other bow shock model, the Peredo model is based on a large data set of shock crossings. Therefore this model is able to provide only an average bow shock position. In Peredo et al. (1995) Figures 3a and 3b clearly demonstrate, that the individual shock crossings are scattered around the average bow shock position with a standard deviation of $\sim \pm 2R_e$. Such a large error can not be accepted in a case study, where a precise calculation of the spacecraft distance to the bow shock is essential. In order to minimize the errors, we first identified the bow shock crossing coordinates by using the spacecraft data and substituted these coordinate values together with the value of the M_A in Equation 2.2. This way we obtained the equation which describes the bow shock shape and position very accurately at the moment when the spacecraft is crossing it. After this we modified the bow shock position and shape according to Equation 2.1 for the whole time period of interest by using the observed solar wind velocity and number density. To summarize, in determining the spacecraft distance to the shock we used the observed bow shock surface which was continuously adjusted to the actual solar wind conditions. By knowing the actual bow shock position, the position of the spacecraft and the magnetic field direction at the spacecraft, the spacecraft distance to the bow shock along the magnetic field can be easily calculated.

2.3   Observations of Upstream Ions

The Cluster mission provides the opportunity to investigate the spatial evolution of diffuse ions with direct measurements for the first time. The particle data used in this study are from the Cluster Ion Spectrometer (CIS) instrument Hot Ion Analyzer (HIA), since CIS-HIA has a better energy resolution above 10 keV than CODIF. On SC2 and SC4 the HIA analyzer is not available for the time period under investigation. Therefore, in order to derive the gradient, HIA data from SC1 and SC3 is used. The magnetic field data are obtained by the FluxGate Magnetometer (FGM) (Balogh et al., 1997).

In order to have suitable data for the gradient study, a few conditions need to be met:

1. The distances between spacecraft need to be sufficiently large, i.e. of the order of $\sim 1 R_e$,

2. The spacecraft need to observe upstream (diffuse) ions for a substantial period of time (i.e. hours) at various distances from the shock,

3. The difference between the SC1 and SC3 distance from the bow shock along the magnetic field needs to be substantial, i.e. of the order of $\sim 1 R_e$,

4. The ion and the magnetic field data must be free of transient changes, i.e. we need to assure that there are no sudden large changes in the solar wind bulk velocity, solar wind plasma density and magnetic field strength (since we are interested in a steady-state process).

The listed conditions restrict the available data considerably, especially regarding the fact that the condition of large separation distance is only satisfied during the 2002-2003 winter and spring operational time, being optimal in the time period between February and April, 2003. (For a detailed description of the spacecraft separation strategy see subsection 1.2.2 and Figure 1.7.) After carefully analyzing the available data we have chosen two upstream ion events: the events on 18 February, 2003 and on 07 March, 2003. The former

is a high solar wind velocity, the latter is a medium solar wind velocity case.

2.3.1   The Upstream Ion Event on 18 February, 2003

During this time period the Cluster spacecraft were upstream of the bow shock on the inbound leg of their orbit. The period was after the passage of a CME (Coronal Mass Ejection), the magnetic field orientation at all four spacecraft was rather constant, providing connection to the quasi-parallel side of bow shock over the whole time period, i.e. between $\sim$ 12:00-24:00 UT. We emphasize that this upstream event is up to now the only one from the Cluster database, which provides us with a continuous, almost uninterrupted upstream ion presence for $\sim$12 hours. This unique characteristic of this event is the result of the absence of the usual ultra-low-frequency, large-amplitude fluctuations in the interplanetary magnetic field.

The solar wind speed decreased almost linearly from 668 km/s to 584 km/s, which makes this case a high solar wind velocity event (the average solar wind velocity is $\sim$ 450 km/s). M_A was $\sim$ 8.

Figure 2.1 shows from top to bottom the solar wind v_x velocity, the three components of the interplanetary magnetic field as measured by FGM on SC1 and the partial density of upstream ions measured by HIA in the energy range of 24-32 keV (which is the highest energy range available on CIS-HIA). Figure 2.2 shows magnetic field magnitude and partial density at both spacecraft (64 s running averages) from 21:00-24:00 UT, i.e. the time interval including the bow shock crossings. The bow shock crossings are characterized by a sudden increase in the magnetic field strength. There are repeated crossings of each spacecraft through the bow shock.

The time period of the multiple crossings of SC1 is indicated by a horizontal bar. It can be seen that when both spacecraft are in the magnetosheath (to the right of the dashed vertical line), the partial densities track each
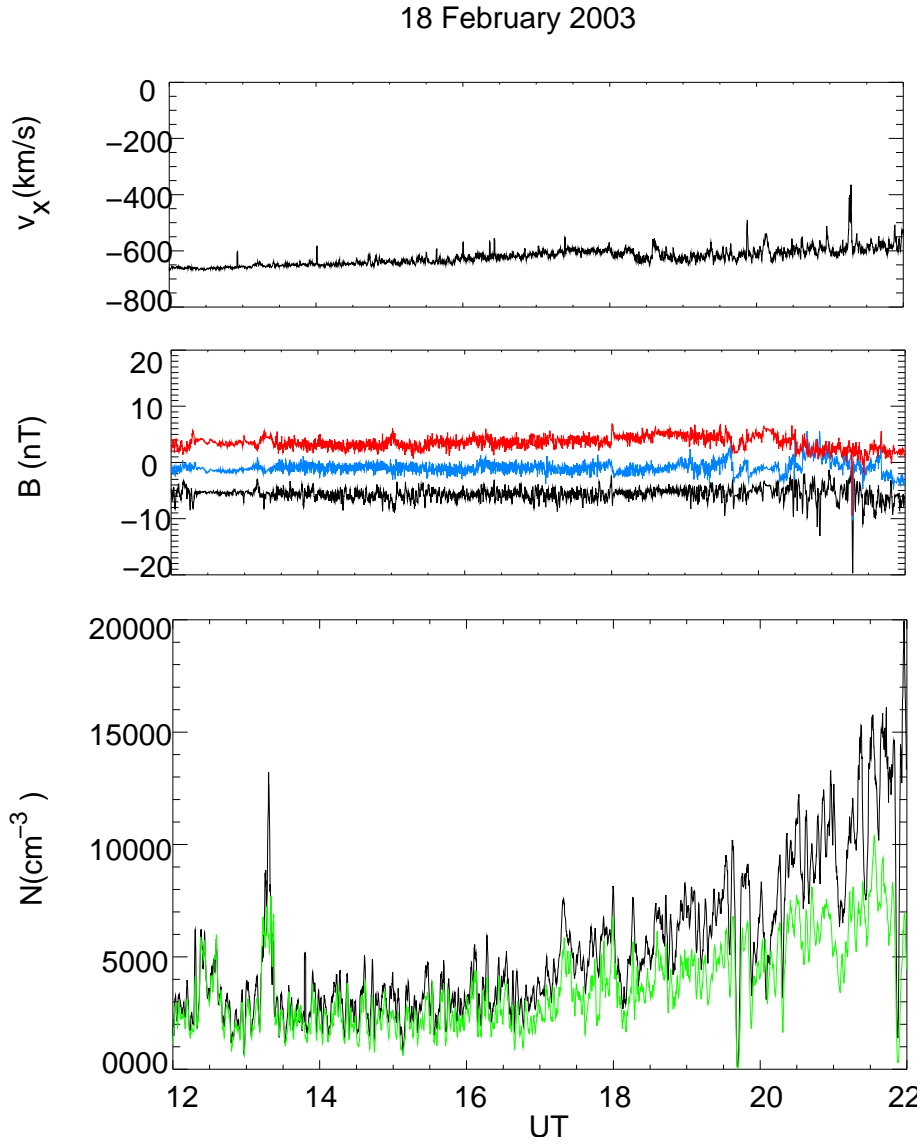
Figure 2.1: From top to bottom: Solar wind velocity v_x and magnetic filed components B_x (black line), B_y (blue line), B_z (red line), as measured on Cluster 1, partial ion density in the 24-32 kev energy range as measured at Cluster 1 (black line) and Cluster 3 (green line).

February 18, 2003
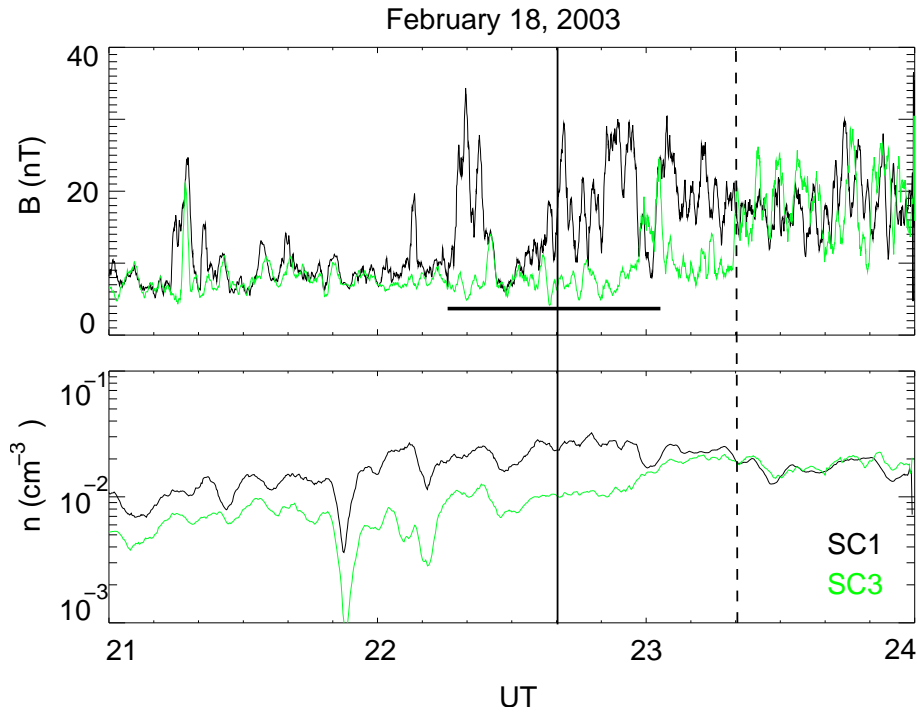
Figure 2.2: The top panel shows the total magnetic field as seen by Cluster 1 (black line) and Cluster 3 (green line), the lower panel presents the partial ion density in the 24-32 keV energy range as measured at Cluster 1 (black line) and Cluster 3 (green line) during the time period when both SC were entering the downstream region, into the magnetosheath. The dashed vertical line shows the time when SC3 crossed the bow shock, the continuous vertical line signals the reference bow shock crossing time for SC1. SC1 crossed the bow shock several times until it finally moved downstream, the time period of the repeated crossings is represented by the horizontal line, in the upper panel.
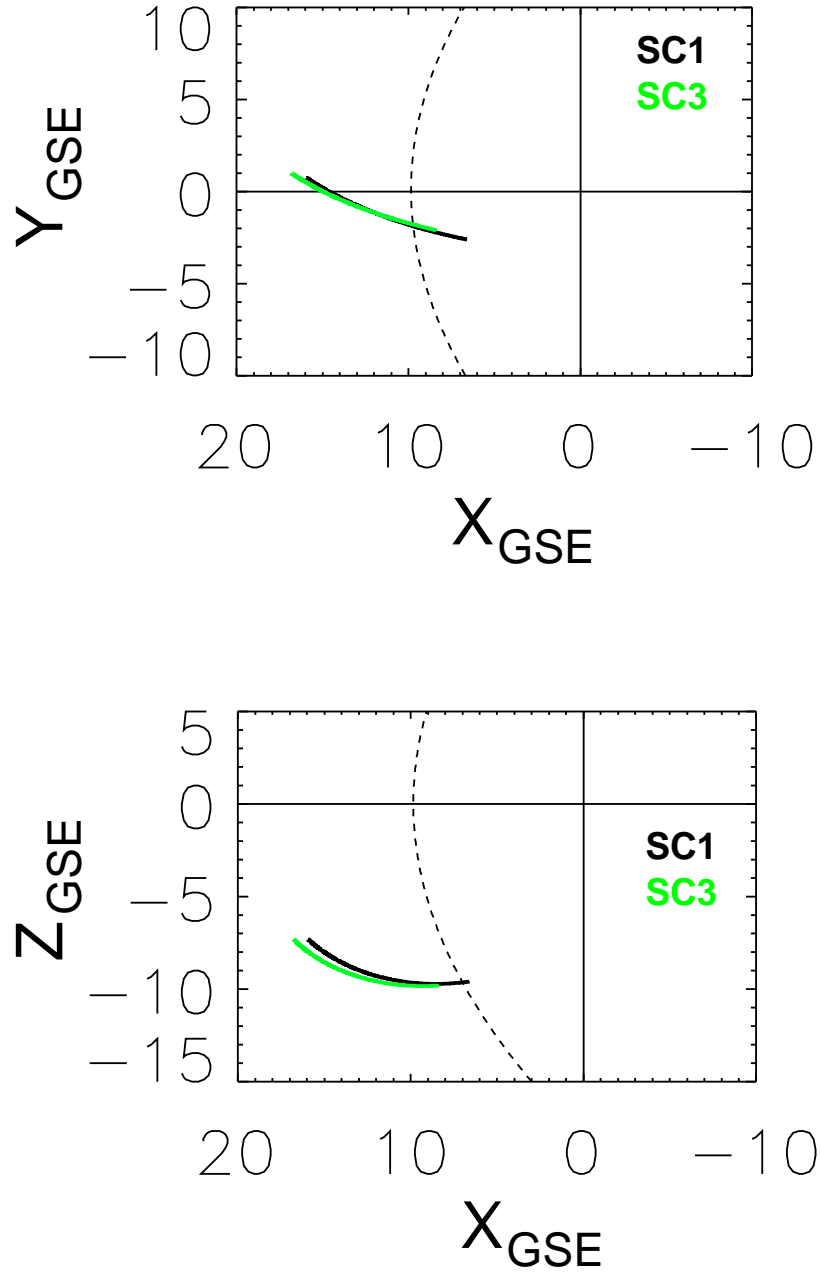
Figure 2.3: Projections of the spacecraft orbits and the bow shock into the GSE (Geocentric Solar Ecliptic) coordinate system x-y and x-z planes, respectively. The bow shock is represented as a curved, dashed line.
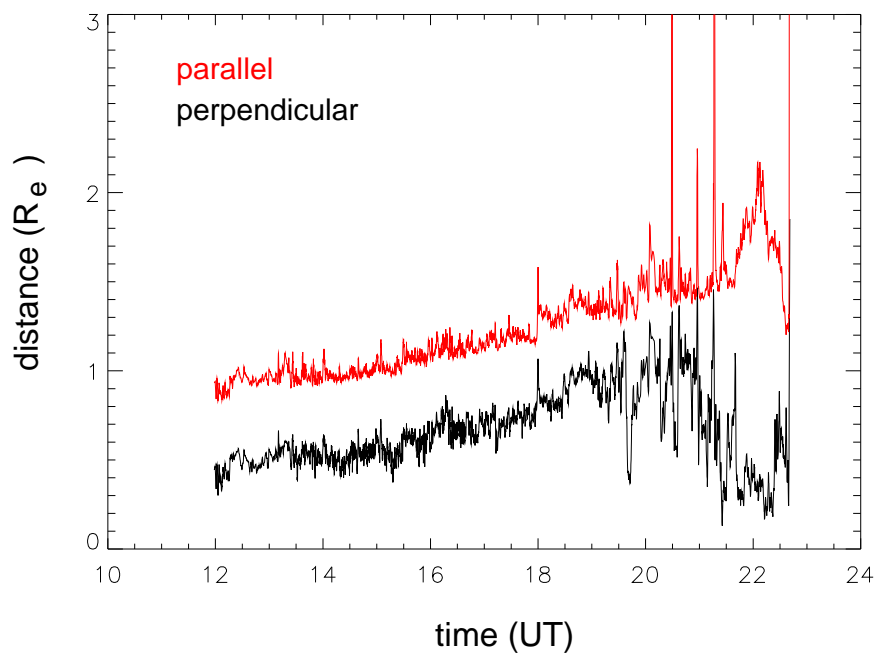
Figure 2.4: Separation distance between SC1 and SC3 perpendicular and parallel to the magnetic field versus time.
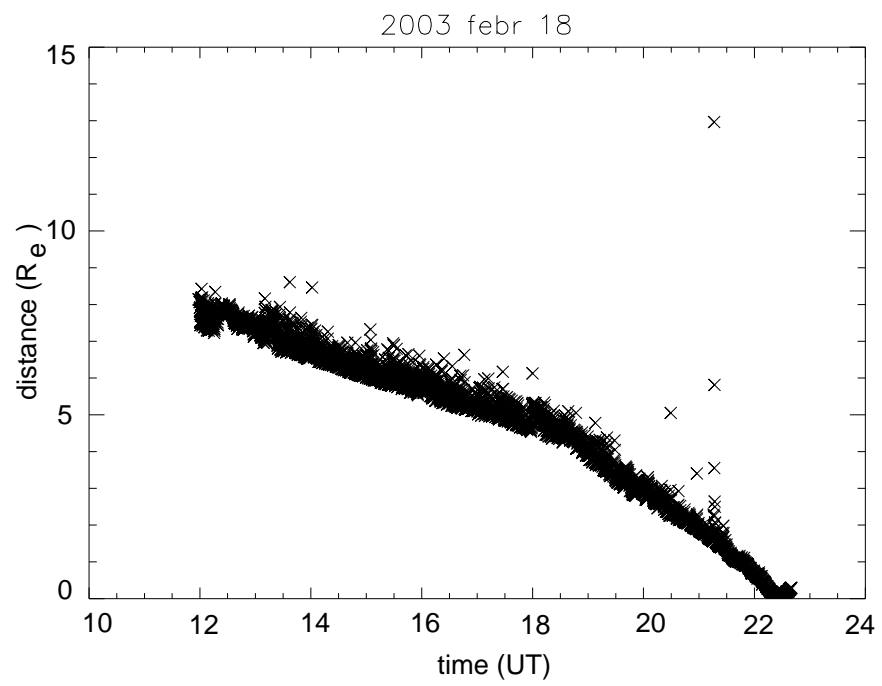
Figure 2.5: The SC1 distance to the bow shock along the magnetic field versus time.

other very well. At both spacecraft the upstream ion partial density reaches its maximum value around the shock crossing, which is in good agreement with the predictions of a steady-state diffusive acceleration theory. In order to determine the average behavior of the upstream particle distribution, we performed a running average of the partial densities and the magnetic field over 8 spins (32 seconds). This eliminates higher frequency fluctuations and reduces the statistical error on the density measurements.

Figure 2.3 shows projections of the spacecraft orbits and the bow shock onto the GSE (Geocentric Solar Ecliptic) coordinate system x-y and x-z planes, respectively. During the time period under investigation SC1 is $\sim$1-$\sim$1.5 R_e closer to the bow shock than SC3. The perpendicular (to the magnetic field) separation of the two spacecraft is between 0.3 R_e and 0.8 R_e, which corresponds to about 1 to 2 ion gyroradii in the energy range considered. Figure 2.4 presents the spacecraft separation distance perpendicular and parallel to the magnetic field versus time. The magnetic field data at SC3 have been used to calculate the intersection point with the model bow shock. The reason for choosing magnetic data from SC3 is that SC1 is situated closer to the shock all the time, therefore its magnetic data, especially the magnetic field direction, can be more disturbed by the high-amplitude magnetic fluctuations which are characteristic in the close vicinity of the quasi-parallel shock.

The distance of the two spacecraft from the bow shock along the magnetic field line has been determined for each 8 spin-averaged time period by the previously described method. Figure 2.5 shows these distances of SC1 from the bow shock along the magnetic field versus time.

The spatial gradient of the partial density of upstream ions was calculated in the four upper energy ranges available on CIS-HIA using the difference of the partial densities at the two spacecraft and the difference of the spacecraft distances along the magnetic field to the bow shock intersection point.

These gradient values were then assigned to the average distance of the two spacecraft from the shock, neglecting perpendicular gradients. During the ~ 10 hour time period we obtained more than 3300 gradient values at various distances. These gradient values were binned in 1 R_e wide bins. Figure 2.6 shows the gradient of the 24-32 keV partial density in units of cm^{-3}/R_e versus distance from the bow shock along the magnetic field in a logarithmic versus linear representation. The horizontal bar represents the distance over which the binning has been performed, while the vertical bar shows the standard deviation from the average partial density value. The data points in this representation can be fitted by a straight line, i.e. the gradient is very well represented by an exponential as a function of distance, which is equivalent to the density falling off exponentially with distance from the bow shock. We obtain an e-folding distance of $L = (2.79 \pm 0.25) R_e$. The procedure described above has been performed for the 4 highest energy channels of the CIS-HIA instrument. The resulting e-folding distances for the partial densities in each of the 4 energy channels are shown in Figure 2.8. As can be seen from Figure 2.8 the e-folding distance of the partial density gradients depends approximately linearly on energy and increases from ~ 0.5 R_e at 11 keV to ~ 2.8 R_e at 27 keV.
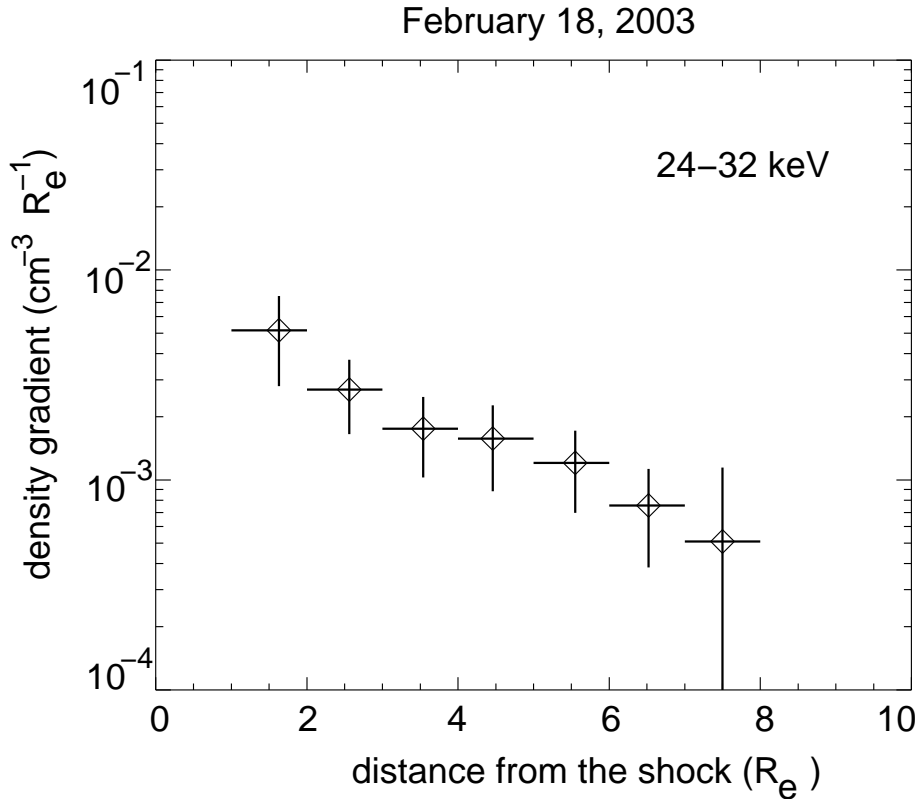
Figure 2.6: The diffuse ion partial density gradient versus distance from the shock for the ions with energies between 24-32 keV. The horizontal bars represent the 1 R_e distances over which the gradient values have been averaged, the vertical bars show the standard deviation of the individual gradient values from the average value of the gradient.

2.3.2   The Upstream Ion Event on 07 March, 2003

For the study of the medium solar wind velocity case the time period between 00:00-12:00 UT has been chosen on 07 March, 2003. This upstream event shows many similarities with the upstream event on 18 February, 2003. For example Cluster was on the inbound leg of its orbit in the upstream region, which made possible the observation of diffuse ions for an extended time period. During this time SC1 was closer to the shock than SC3. The separation distance between the spacecraft was $\sim 1\mathrm{R_e}$ at $\sim$00:00 UT. This distance increased gradually to $\sim 1.5\mathrm{R_e}$ as the spacecraft moved closer to the shock.

The solar wind bulk velocity was fluctuating slightly around ~ 490 km/s, the solar wind number density was ~ 3.5 cm^{-3}. The Alfvén Mach number was ~ 7, close to the value observed during the 18 February, 2003, event when the $\mathrm{M_A}$ was ~ 8. Therefore in both cases we have high Mach number shocks. Figure 2.7 presents from top to bottom the solar wind velocity v_x, the three components of the interplanetary magnetic field as measured by FGM on SC1, and the partial densities of upstream ions in the 24-32 keV energy range at SC1 and at SC3.

The interplanetary magnetic field shows the usual fluctuations which is a characteristic feature of the solar wind. This resulted in a continuous variation of the magnetic field direction. Due to the fluctuations the connection of the spacecraft to the quasi-parallel side of the shock was intermittent. Therefore the energetic ion observation was many times interrupted, as it can be seen from Figure 2.7. Despite the fact that the upstream ion presence at the spacecraft position was not continuous, the Cluster spacecraft recorded energetic ions at different distances to the bow shock for a sufficient period of time to make it possible to derive the diffuse ion gradient in front of the shock.

For the calculation of the gradient the same procedure as for the analysis
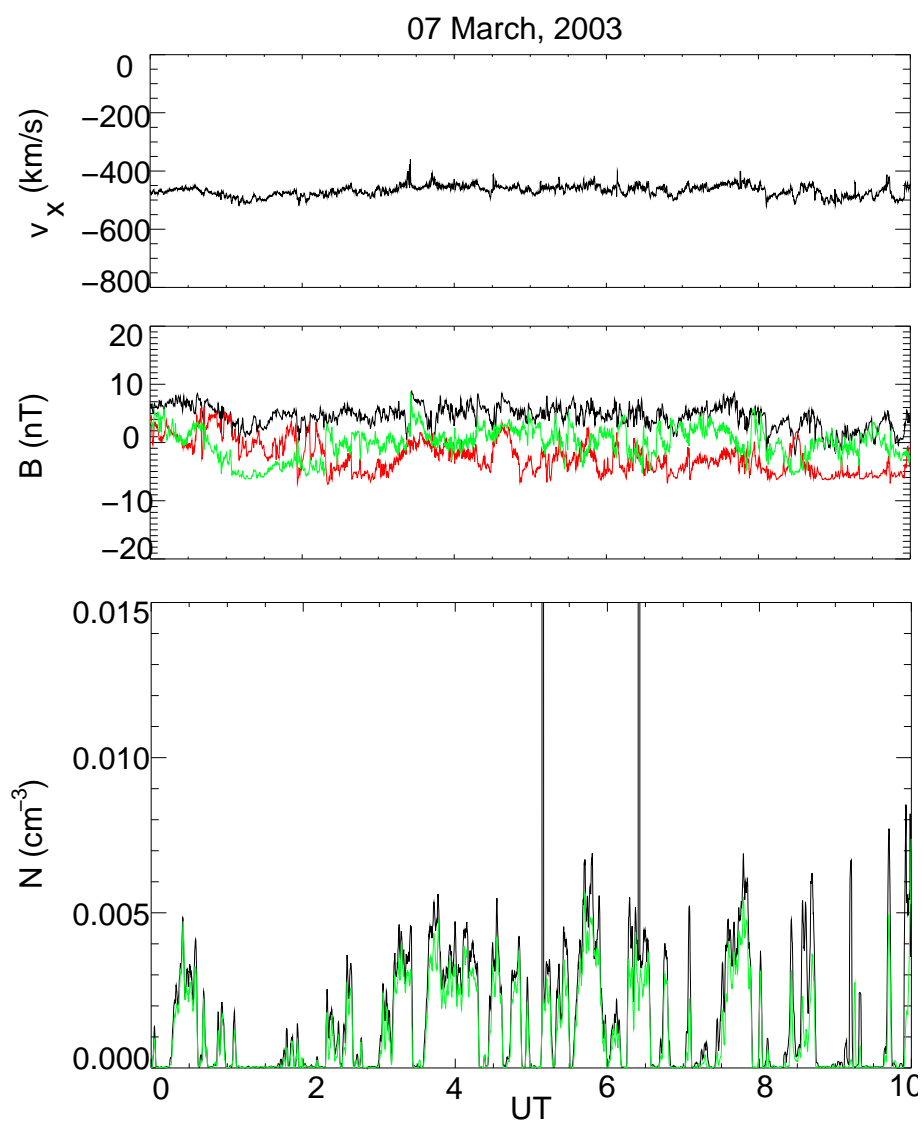
Figure 2.7: From top to bottom: Solar wind velocity v_x, magnetic field components B_x (black line), B_y (green line),B_z (red line), as measured on Cluster 1, partial ion density in the 24-32 kev energy range as measured at Cluster 1 (black line) and Cluster 3 (green line).

of the 18 February, 2003 upstream ion event has been used. Therefore here we only reiterate the important steps. We used the four upper energy channel partial density data provided by the CIS-HIA instrument onboard SC1 and SC3 and the previously described bow shock model in order to calculate the partial density gradient. This derived gradient was assigned to the average distance value of the two spacecraft distances to the bow shock along the magnetic field. The resulting e-folding distances for the partial densities in each of the 4 energy channels are shown in Figure 2.8. The e-folding distance increases with energy from $\sim$1.9 R_e at 11 keV to $\sim$4.0 R_e at 27 keV.

2.4   Determination of the Spatial Diffusion Co-efficient

We have determined directly the spatial gradient of diffuse ions at various distances from the bow shock along the magnetic field using ion and magnetic field data from two Cluster spacecraft. This analysis serves two purposes: first to investigate whether the energetic ions are really subject to a diffusive transport in the upstream region and second, to study the efficiency of ion acceleration at the bow shock.

In order to determine the dependence of the e-folding distance on the solar wind velocity, we analyzed two upstream ion events, a high solar wind velocity upstream event (February 18, 2003; $v_{SW} \sim 640$ km/s, $M_A \sim 8$), and a medium solar wind velocity upstream ion event (March 07, 2003; $v_{SW} \sim 487$ km/s, $M_A \sim 7$). The gradient of the partial densities at both events falls off exponentially with distance in all four energy channels. The e-folding distance increases approximately linearly with energy, $L \propto E$, in accordance with the results by Trattner et al. (1994). For the high solar wind velocity event the e-folding distance at ~ 30 keV is $\sim 3R_e$, which is about half the

value obtained on a statistical basis by Trattner et al. (1994) and Ipavich et al. (1981). At 10 keV the difference appears to be even more striking with their value of 2.9 R_e in comparison with our result of 0.5 R_e at 11 keV.

For the medium solar wind velocity event the e-folding distance at ~ 27 keV is ~ 4 R_e and at ~ 11 keV is ~ 1.9 R_e, these values are more comparable with the results obtained by Trattner et al., (1994).

Figure 2.8 presents the dependence of the e-folding distance on particle energy for the high and the medium solar wind velocity events. The exponential decrease of the energetic ion partial density with distance from the bow shock demonstrates that the ions undergo a diffusive transport. At the same time the dependence of the e-folding distance on solar wind velocity is a further proof of the diffusive transport, since according to the quasi-linear theory the e-folding distance becomes larger when the solar wind velocity is smaller (the important parameter of the diffusion is the diffusion coefficient). We will discuss this in more detail below.

Assuming that diffusion from the shock is balanced by convection with the solar wind, in a steady state the e-folding distance is given by

$$L(E) = \frac{\kappa(E)}{v_{SW}} \tag{2.9}$$

(Giacalone et al., 1993) where $L(E)$ is the e-folding distance, $\kappa(E)$ the diffusion coefficient and v_{SW} is the solar wind bulk velocity. Since

$$\kappa(E) = \frac{\lambda(E) \cdot v}{3} \tag{2.10}$$

where $\lambda(E)$ is the scattering mean free path (or diffusion length) and v is the particle velocity (in the plasma frame). We can write

$$\lambda(E) = 3L(E)\left(\frac{E_{SW}}{E}\right)^{1/2} \tag{2.11}$$
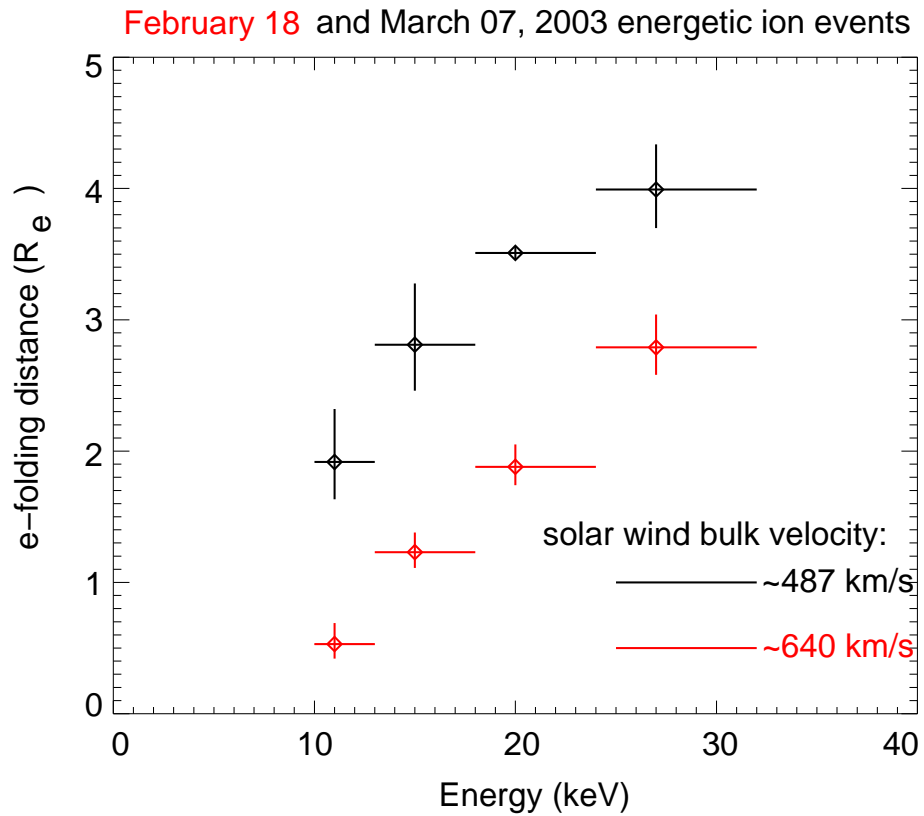
Figure 2.8: The e-folding distance versus energy in the high (red color) and the medium (black) solar wind velocity case. The horizontal bars represent the energy channels, the vertical error bars indicate the 1-sigma uncertainty of the fit.

where E is particle energy and E_{SW} is the bulk energy of the solar wind. After substituting our result of $L(E)$ in Equation 2.11, the scattering mean free path energy dependence can be expressed as

$$\lambda(E) \propto E^{0.5} \tag{2.12}$$

Substituting a value of ~ 640 km/s solar wind velocity for the high solar wind velocity event, we obtain a mean free path of ~ 2.4 R_e for the 30 keV ions. In the case of the medium solar wind velocity event, substituting the solar wind velocity value $\sim$490 km/s, we obtain a mean free path of ~ 2.4 R_e for the 30 keV ions.

The same diffusion length and value of the diffusion coefficient for the 30 keV ions in the case of high and medium solar wind velocity means that in both cases the physical process of diffusion is fundamentally the same. This result is in agreement with the theory, where, as mentioned before, the relation

$$\kappa(E) = L(E) \cdot v_{SW} \tag{2.13}$$

holds for the diffusion coefficient. Therefore, according to the theory, the diffusion coefficient (at a given energy) is a constant of the process, since as the solar wind velocity becomes higher, the e-folding distance becomes smaller.

However, when we compare the diffusion coefficients in the low energy range for the two upstream events, the picture becomes more complicated. Figure 2.9 shows values of the diffusion coefficients for the high (red colour) and medium (black color) solar wind velocity case, respectively, versus energy. At 30 keV the diffusion coefficient is the same for both events (i.e. high and low solar wind velocity events), but in the lower energy ranges there is an increasing difference between the two cases. For example at 10 keV the value of the diffusion coefficient for the high solar wind velocity case is

approximately 40 % of the value observed at the time of the medium solar wind velocity event.

The obtained result does not imply that the diffusive transport theory is wrong; in fact the analysis of the two upstream events demonstrates that the energetic ions truly undergo a diffusive transport. However, the difference between the diffusion coefficients in the two cases shows the limitation of the theory. The model of diffusive transport, which is based on the quasi-linear theory, does not include the compressional waves and the non-linear wave particle effects. Compressional waves, for example, might be able to influence the energetic ion distribution and spatial variation of energetic ion density in front of the bow shock which in turn would result in a modification in the value of the diffusion coefficient. A more detailed discussion related to the compressional wave presence and evolution in front of the shock is presented in Chapter 4. Here we only conclude that the results show the complexity of the foreshock region. To come to a final conclusion requires the investigation of considerably more upstream events, which are presently not available.

2.5   Ion Acceleration at the Earth's Bow Shock

In this section we analyse the efficiency of ion acceleration at the bow shock. Shock acceleration has been studied extensively and several mechanisms were proposed for accelerating particles by collisionless shocks. The two mechanisms that are widely accepted are shock drift acceleration (SDA, Decker 1983; Armstrong, Pesses Decker, 1985) and diffusive acceleration (first and second-order Fermi acceleration), discussed in detail in the review by Jones and Ellison, (1991).

The SDA is the process, whereby particles due to the magnetic field gradient drift along the shock front and gain energy in the motional electric
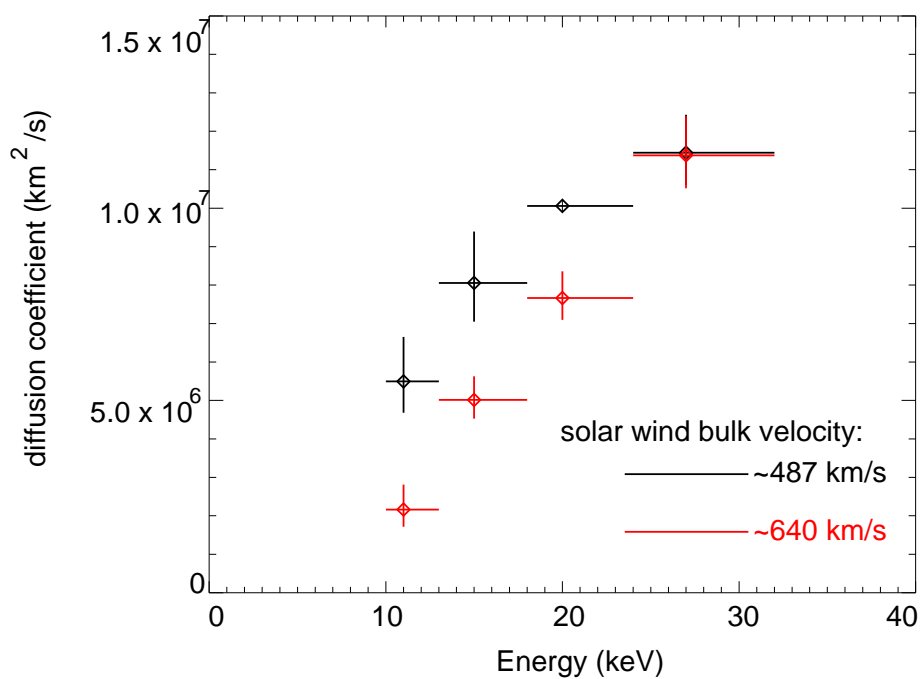
Figure 2.9: The dependence of the diffusion coefficient on energy in the high (red color) and the medium solar wind velocity case. The horizontal bars represent the energy channels, the vertical error bars indicate the 1-sigma uncertainty due to the fitting procedure.

field. In the case of a parallel shock, where the shock normal is parallel to the magnetic field, there is no motional electric field, therefore the shock drift acceleration is unlikely to take place under these conditions.

First order Fermi acceleration occurs when particles diffuse back and forth across the shock front and gain energy by being scattered (i.e., pitch angle scattered) by magnetic waves embedded in the converging plasma flows. Second order Fermi acceleration results when particles are scattered in a region with random magnetic turbulence. The particle that experiences more "head-on" collisions than retreating ones, gains energy.

Jokipii (1982, 1987) and Decker (1988) demonstrated that the rate of energy gain due to the different acceleration processes depends heavily upon the geometry of the shock. They showed that the efficiency of the second-order Fermi acceleration in the foreshock region is small compared to the efficiency of the first-order process. Therefore its contribution to the overall ion energy gain can be neglected in this region. The main acceleration mechanism at the quasi-parallel bow shock is the first-order Fermi acceleration.

An ion gains energy when it is pitch-angle scattered in the upstream region, moves downstream where it is again scattered and finally crosses the shock front in the upstream direction. The particle net energy gain can be calculated as (Drury, 1983):

$$\Delta p = \frac{4}{3} \frac{U_1 - U_2}{v} p \tag{2.14}$$

where Δp is the mean momentum gain, p is the particle momentum, U_1 and U_2 are the upstream and downstream plasma bulk velocities, respectively. For an ion to reach higher energies, the described process needs to be repeated several times. In other words, an already accelerated particle has to be scattered efficiently enough to assure that it will not escape far upstream or move downstream where it is lost for further acceleration.

The results obtained from analysing the two upstream events show that for

the 30 keV energy particles the diffusion mean free path in both cases is ~ 2.4 R_e, this being the distance over which statistically a particle velocity direction is reversed. Assuming a steady-state, the acceleration time from an injection momentum p_i up to p is (e.g. Axford, 1981; Drury, 1983):

$$\tau_{Fermi} = \frac{3}{\Delta U} \int_{p_i}^{p} \left(\frac{\kappa_1}{U_1} + \frac{\kappa_2}{U_2} \right) \frac{dp'}{p'} \qquad (2.15)$$

where κ_1 (κ_2) is the upstream (downstream) diffusion coefficient and $\Delta U = U_1 - U_2$. The timescale of acceleration can be approximated with the following simplified formula (Forman, 1981):

$$\tau_{Fermi} = \frac{4\kappa}{v_{SW}^2} = \frac{4L}{v_{SW}} \qquad (2.16)$$

where v_{SW} is the solar wind bulk velocity and L is the e-folding distance. For 30 keV ions, as derived in subsection 2.3.1, $L \sim 3R_e$. With $L \sim 3R_e$ and $v_{SW} \sim 600$km/s we obtain

$$\tau_{Fermi} \sim 120 s. \qquad (2.17)$$

The small value of the diffusion mean free path and the relatively short time needed for a solar wind ion to reach an energy of 30 keV shows that the ions are scattered very efficiently close to the shock and that the first order Fermi acceleration of the ions is almost unavoidable. Combining these results with the results obtained by Trattner et al. (1994), who show a strong correlation between the energetic ion density and the incoming solar wind density, we conclude that the diffuse energetic particles found in the upstream region are mainly bow shock accelerated solar wind particles.

Chapter 3

Spatial-Temporal Evolution of Energetic Ion Distributions

3.1 Observations

In the previous chapter we analysed the diffuse ion behaviour in the 10-32 keV energy range in front of Earth's bow shock and we demonstrated that the diffuse ions are subject to diffusive transport.

In this chapter, using the data from 18 February, 2003 upstream ion event, we extend our analysis to lower energies in order to study the behavior of the field-aligned beam ions in the foreshock region, in particular the proton population. We focus on the protons, since they are the main component of the solar wind as well as of the energetic ion population. For this study we use the magnetic field data provided by the FGM instrument and the ion data provided by the CIS instrument CODIF analyser. The reason why the CODIF data is used for the analysis is that CODIF is capable to distinguish the protons from other ions.

We perform the analysis over the time period between 11:00-14:00 UT, on 18 February, 2003. The FGM and CODIF data are provided by the SC1,

since this spacecraft has the highest sensitivity ion data during the time period of observations.

Figure 3.1 shows the particle distribution in the $v_\parallel$(velocity component parallel to the magnetic field) versus $v_\perp$ (velocity component perpendicular to the magnetic field) velocity space, a cut of the full 3D distribution in the plane defined by the solar wind bulk velocity vector and the average magnetic field vector (note that the $v_\parallel$ vs $v_\perp$ representation is obtained by rotation of the coordinate system according to the magnetic field direction; therefore $v_\perp$ can have positive and negative values also). The solar wind distribution appears in the figure as an elongated, red-colored patch; this is due to the fact that the CODIF sensor, to avoid saturation and degradation in the high gain section, does not sweep through the whole solar wind distribution, but stops at ~ 2 keV. Because of the limited sweep the solar wind distribution is incomplete, and the color does not represent the real value of the solar wind flux. Outside of the red patch representing the solar wind on this plot other areas of the velocity space present the real value of the ion flux. The angle between the center of the red patch (i.e. the solar wind distribution) and the horizontal axis of the plot (i.e. $v_\parallel$) represents the angle between the solar wind bulk velocity and the ambient magnetic field direction. The distribution is obtained by averaging over 300 seconds; this averaging was necessary in order to smooth the magnetic fluctuations and to obtain the average magnetic field direction, but also to decrease the statistical error in the particle data. In the lower figure the magnetic field vector components are presented in the GSE coordinate system. All the plots containing the distribution and the magnetic field presented in this chapter have the same format and composition as described for Figure 3.1.

In this section five ion distributions and the accompanying magnetic field (i.e. magnetic field vector components) will be presented at different times and spacecraft positions. The major characteristics of the different types
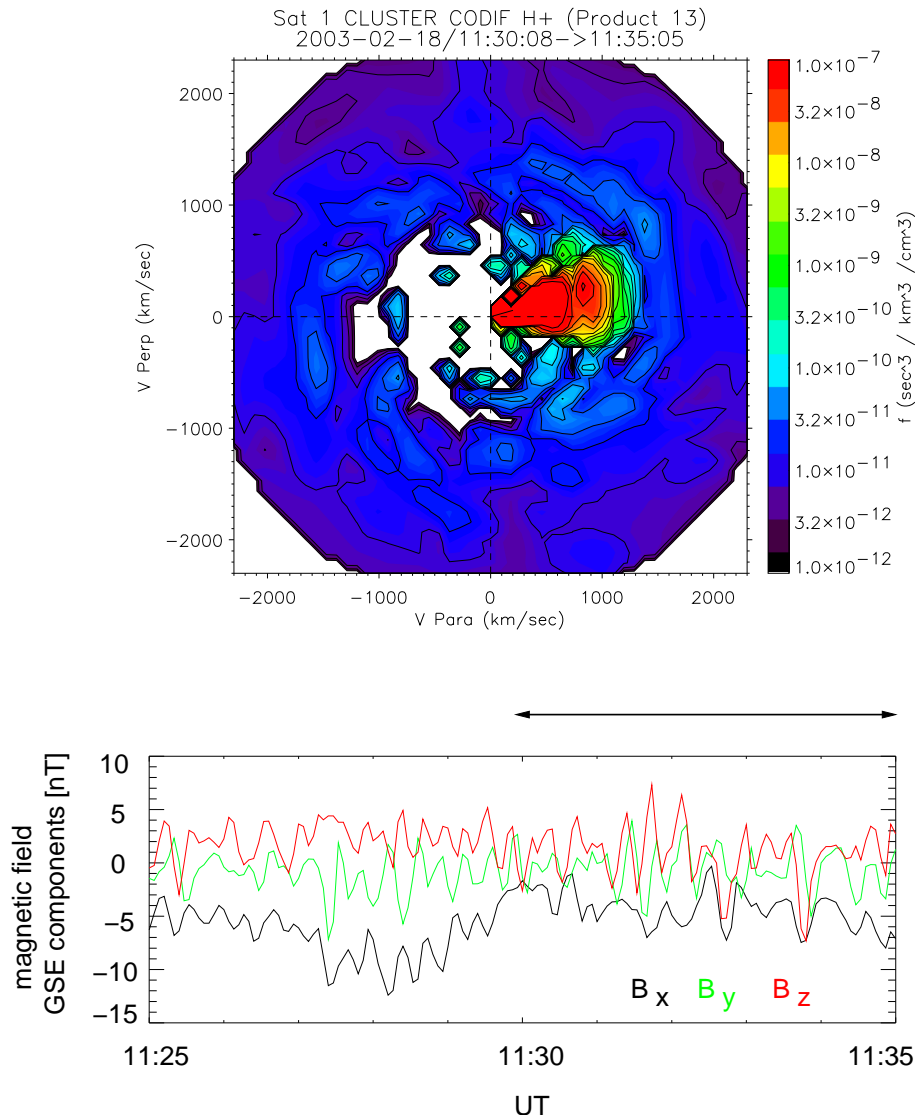
Figure 3.1: The upper figure shows a cut of the 3D ion distribution in the v_{para} vs v_{perp} velocity space, where v_{para} is the velocity component parallel to the magnetic field and v_{perp} is the velocity component perpendicular to the magnetic field. The plane of the cut is defined by the magnetic field and the solar wind bulk velocity vector. The lower figure shows the magnetic field components in GSE coordinates. The horizontal bar above the lower figure shows the time period of averaging to produce the ion distribution. The distribution is typical for diffuse ions, presenting a doughnut shape, a broad ring-like distribution, as a consequence of pitch angle scattering of high energy ions by large amplitude, low frequency waves. These waves can be observed clearly in the lower figure.

of ion distributions and the associated magnetic field fluctuations will be
pointed out, a more complete discussion and an overview of the whole sce-
nario will be provided in the next section.

At 11:25 UT the spacecraft (in the following all references in this chap-
ter to "spacecraft" will refer to SC1) was situated in the upstream region,
the magnetic field lines connecting it to the quasi-parallel bow shock. In
Figure 3.1 the upper figure shows a characteristic diffuse ion distribution,
which has a broad, ring-like shape (Paschmann et al., 1981), the distribution
observed between 11:25-11:30 UT by the spacecraft. The lower figure shows
low-frequency, high-amplitude magnetic fluctuations at the same time; these
fluctuations can always be observed in the presence of diffuse ions (Hoppe et
al., 1982). The magnetic waves propagate in the upstream direction along
the magnetic field with a velocity of $\sim v_A$, but since the speed of wave prop-
agation is substantially lower than the solar wind bulk velocity, these waves
are convected to the shock by the plasma flow. This also means that the
waves are generated in-situ, i.e. they cannot come from the downstream di-
rection (Hoppe et al., 1982). In order to study in detail the evolution of the
energetic ions and the associated waves, the spacecraft position related to the
foreshock geometrical structure needs to be investigated. Figure 3.2, lower
figure, shows the spacecraft position in the x_{GSE} versus z_{GSE} plane every 5
minutes between 11:00 and 14:00 UT. The lines emerging from the spacecraft
symbols correspond to the magnetic field direction. The upper figure shows
the angle between the magnetic field and the x_{GSE} coordinate versus time.

When speaking of the steadyness of the average magnetic field direction,
we refer to the fact that during this time period the magnetic field direction
was not changing significantly or abruptly, however there are slight changes,
as it can be observed from Figure 3.2. Analysing the magnetic field vector
components (for example see Figure 3.1), we note that the main components
are B_x and B_z. The value of B_y is small compared to the other two compo-
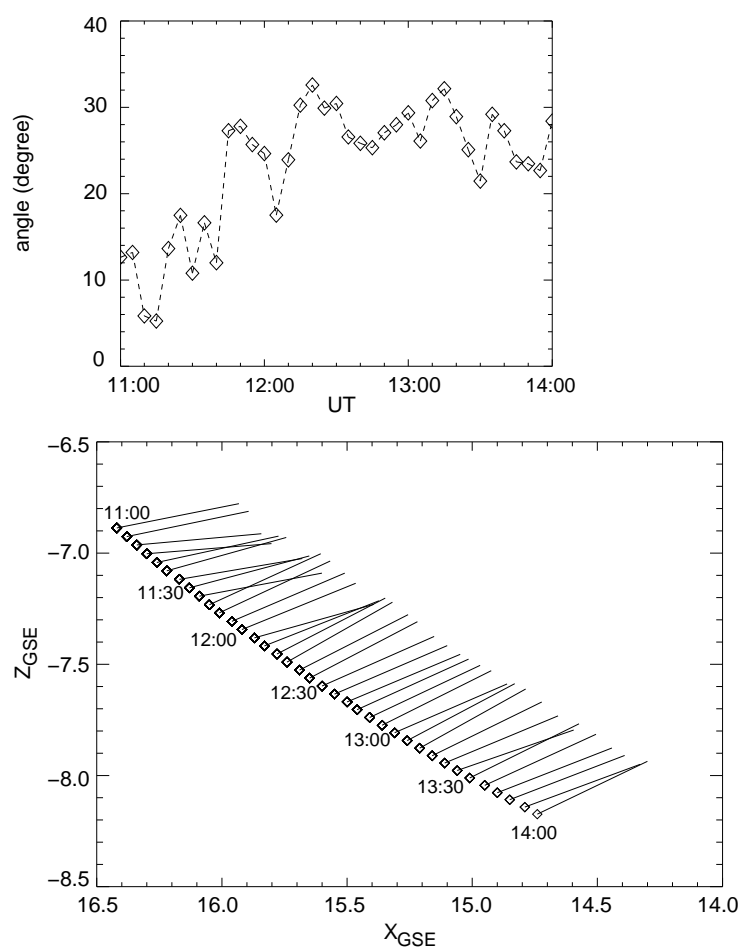
Figure 3.2: The lower figure presents the spacecraft position in the x_{GSE} versus z_{GSE} plane taken in five-minute intervals. The lines emerging from the spacecraft symbols show the magnetic field direction. The upper figure shows the angle between the magnetic field and the x_{GSE} coordinate versus time. Each symbol in the upper figure corresponds to a spacecraft position on the lower figure.

nents, therefore B_x and B_z determine largely the direction of the magnetic field and also the connection point of the spacecraft to the bow shock along the field line. In Figure 3.2 it can be observed that at 11:25 UT the angle between the magnetic field and the x_{GSE} axis is $\sim16°$, meaning that at this time the spacecraft is magnetically connected to the quasiparallel side of the shock. The smallness of the angle is equivalent to the spacecraft being situated deeper in the foreshock region; the foreshock boundary being further upstream of the spacecraft. With time the angle between the magnetic field and the x_{GSE} axis becomes larger and reaches at 12:20 UT the value of $\sim34°$. This change of the magnetic field direction moves the foreshock upper boundary closer to the spacecraft, actually making it possible for the spacecraft to observe the Field-Aligned Beam (FAB).

Figure 3.3 presents the ion distribution and the associated magnetic field for the time period between 12:20-12:25 UT. On the left side of the upper figure the FAB can be identified as a localized, high flux of protons directed into the upstream direction along the magnetic field (since B_x is less than 0, a negative v_{para} corresponds to upstream direction). Thus it can be seen on the opposite side of the solar wind distribution in velocity space. The FAB is a beam of solar wind ions which are reflected at the quasi-perpendicular side of the bow shock and which have a velocity of around twice the solar wind bulk speed (in the solar wind frame). The stream of the FAB ions usually can be observed in the presence of no or very small magnetic fluctuations. This can be seen in the lower part of Figure 3.3, where the magnetic field components are practically free of large amplitude fluctuations, especially between 12:24-12:26 UT. In the distribution plot (upper figure) the right side of the velocity space (except the area occupied by solar wind ions) is mostly empty, showing that there are no backscattered energetic ions. In addition to the FAB ions, we see the presence of higher velocity ions which appear as superposed on the FAB ions. These ions can not be identified as

part of the field-aligned beam since their velocity reaches values higher than 2000 km/s. For a full understanding of this distribution a deeper analysis will be provided in the discussion section. Here we only point out the fact that higher energy ions are observed together with the FAB ion population.

Figure 3.4 presents the particle distribution for the time period between 12:45-12:50 UT. At this time the magnetic field direction is oriented in such a way that the foreshock boundary is situated further upstream of the spacecraft position. The combination of the field direction and of the fact that the spacecraft moved closer to the shock results in a position of the spacecraft deeper in the foreshock region. On the lower figure we can observe that there is strong wave activity at this time. These waves are scattering the particles in pitch angle, the originally focused beam ion population now presents a kidney-shaped distribution. Beside this intermediate distribution of lower energy ions there is superposed an almost complete ring distribution of diffuse ions. As a result of the wave activity the intermediate ions are also partially backscattered (see the right side of the upper figure, showing that some ions have a positive parallel velocity). But as mentioned above, the ring distribution of the diffuse ions is not yet completely closed. This can be due to the limited time available for scattering or due to a smaller energy density of the waves (i.e. the wave amplitude is smaller than observed deeper in the foreshock region). Figure 3.5, 40 minutes later, shows the particle distribution in a more "evolved" phase of the scattering: the diffuse ion ring is already closed and a greater fraction of ions forming the kidney-shaped part of the lower-energy ion distribution are backscattered. Figure 3.6, another 30 min later, shows the final state: the diffuse ions are almost totally isotropic, while the original FAB ions, which earlier formed a kidney-shaped intermediate distribution, at this time present a toroidally gyrating ion distribution: the middle part of the former kidney-shape is missing. This is due to the combination of scattering and convection by the solar wind: the ions which

have a larger parallel velocity oriented upstream have already escaped the region, while the ions with pitch angles closer to 90° are convected deeper into the foreshock.

3.2 Discussion

The upstream event on February 18, 2003, observed by SC1 between 11:00-14:00 UT, provides the possibility to analyse in detail the energetic ion behavior from the ion foreshock boundary deep into the foreshock region as a result of the combination of several key conditions, like the absence of the usual ultra-low-frequency, large-amplitude fluctuations in the interplanetary magnetic field, the unusually high solar wind velocity and the favorable location of the spacecraft. It will be shown how the FAB ion distribution is transformed into an intermediate, and finally into a toroidally gyrating ion distribution as convected by the solar wind plasma. The analysis also reveals important details about the diffuse ion distribution properties at different positions of the foreshock region.

Figure 3.7 presents an overview of the three-hour upstream ion observation. The figure shows the evolution of the ion distributions and the associated magnetic waves over this time period. At ~11:35 UT the spacecraft observes a broad ring-like shaped, typical diffuse ion distribution in the presence of high-amplitude, low-frequency magnetic fluctuations. As we showed in the previous section, at this time the spacecraft is situated deep in the foreshock region. The ion distribution in velocity space has a hole in the middle which means that the intensity of the lower-energy ions in this region is very small.

Later the magnetic field direction changes and the spacecraft is able to observe a field-aligned beam at ~12:25 UT. At this time the wave activity is minimal. It was demonstrated by earlier investigations (Greenstadt et al.,
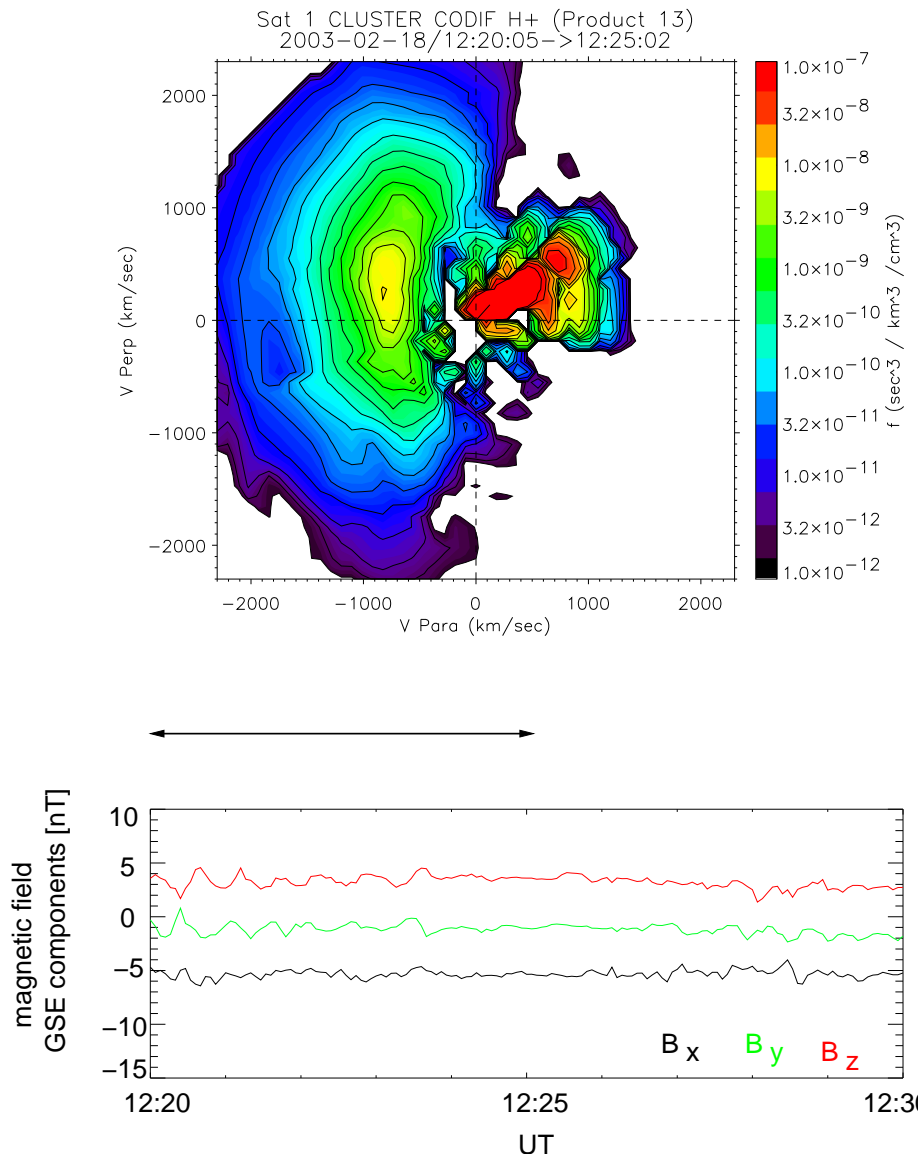
Figure 3.3: (For the general description of figure structure see caption of figure 3.1) The upper figure presents a Field-Aligned Beam (FAB) distribution, observed by the SC1, between 12:20-12:25 UT. In addition to the highly focused flux of beam particles on the left side of the figure (colour code from yellow to green), one can also observe a presence of higher velocity (i.e. larger than 2000 km/s) ions, which show a smaller intensity (dark blue to violet in colour). On the right side of the figure it can be observed that except for the solar wind ions this side is almost empty, showing that there are no backstreaming ions. The lower figure shows very small-amplitude magnetic fluctuations.
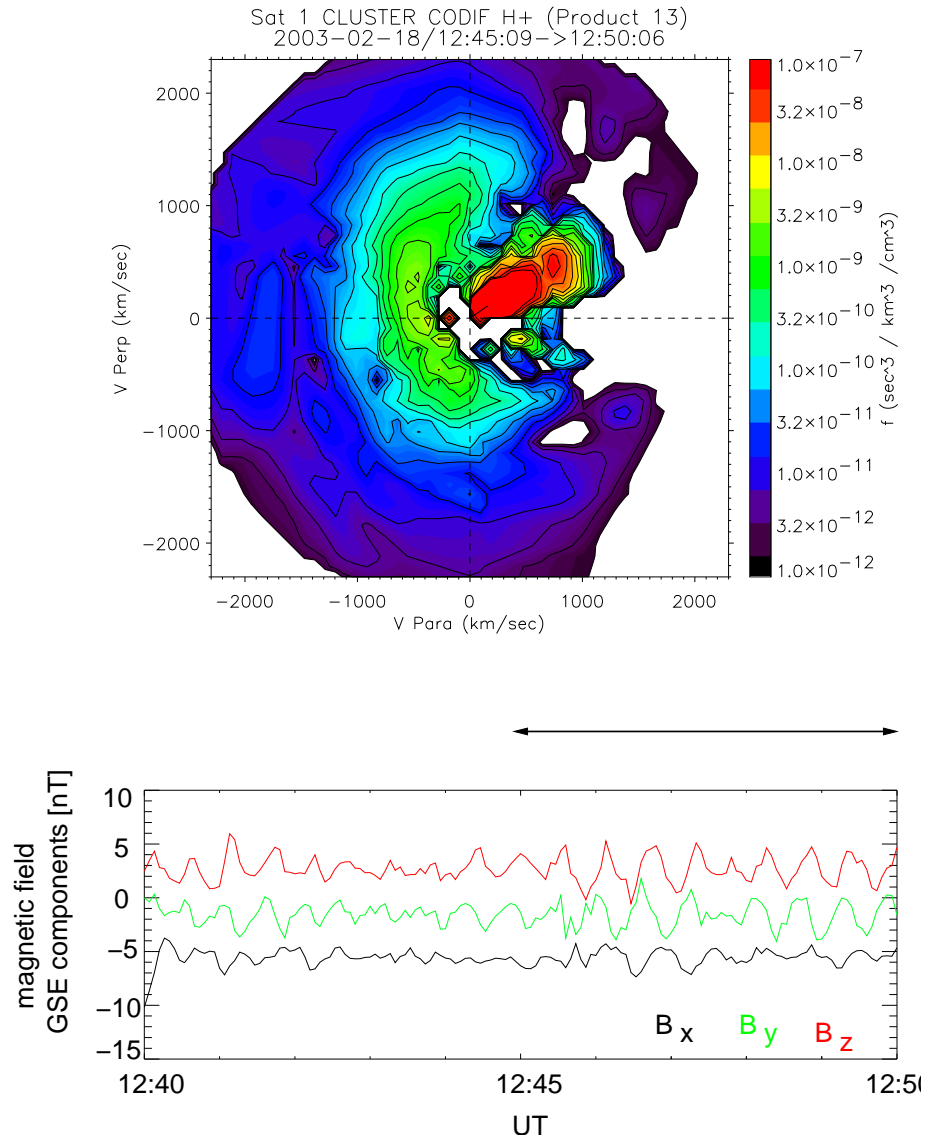
Figure 3.4: (For the general description of figure structure see caption of Figure 3.1) The upper figure presents an intermediate ion distribution between 12:45-12:50 UT. In comparison to the distribution at 12:20 UT, this distribution shows the result of a scattering by waves: the originally FAB ions are pitch-angle scattered, forming a kidney-shape distribution, depicted in green colour (upper figure). Higher velocity ions are also scattered (dark blue to violet in colour), on the right side of the figure it can be observed that a fraction of all ions are even backscattered. The lower figure presents the magnetic field components, showing a wave activity of moderate amplitude.
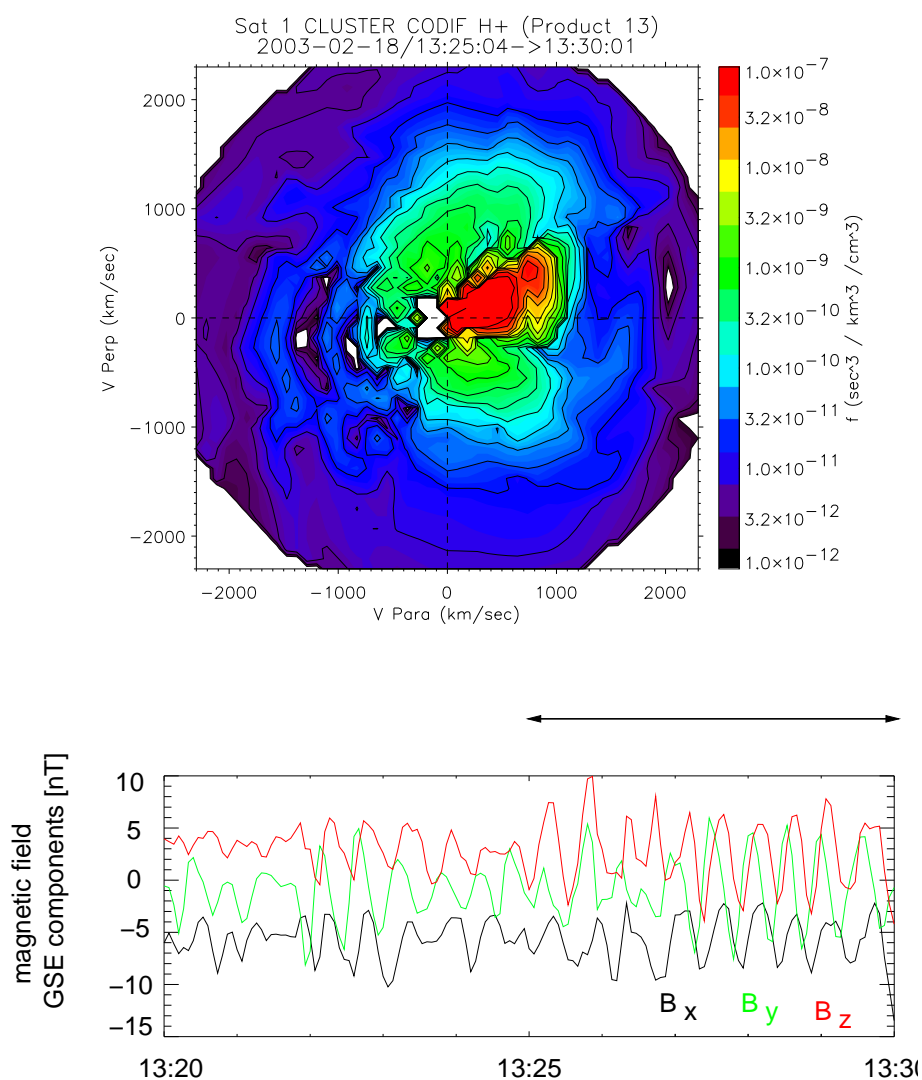
Figure 3.5: (For the general description of figure structure see caption of Figure 3.1) The upper figure presents an intermediate ion distribution between 13:25-13:30 UT. In comparison to the distribution at 12:40 UT, this one shows a more developed phase of the scattering, note that the diffuse ions already form a complete ring distribution, while the lower-energy ions are getting more and more scattered in pitch angle. On the lower figure are presented the magnetic fluctuations in the components of the magnetic field, showing clear, large-amplitude magnetohydrodynamic waves, scattering efficiently the energetic particles.
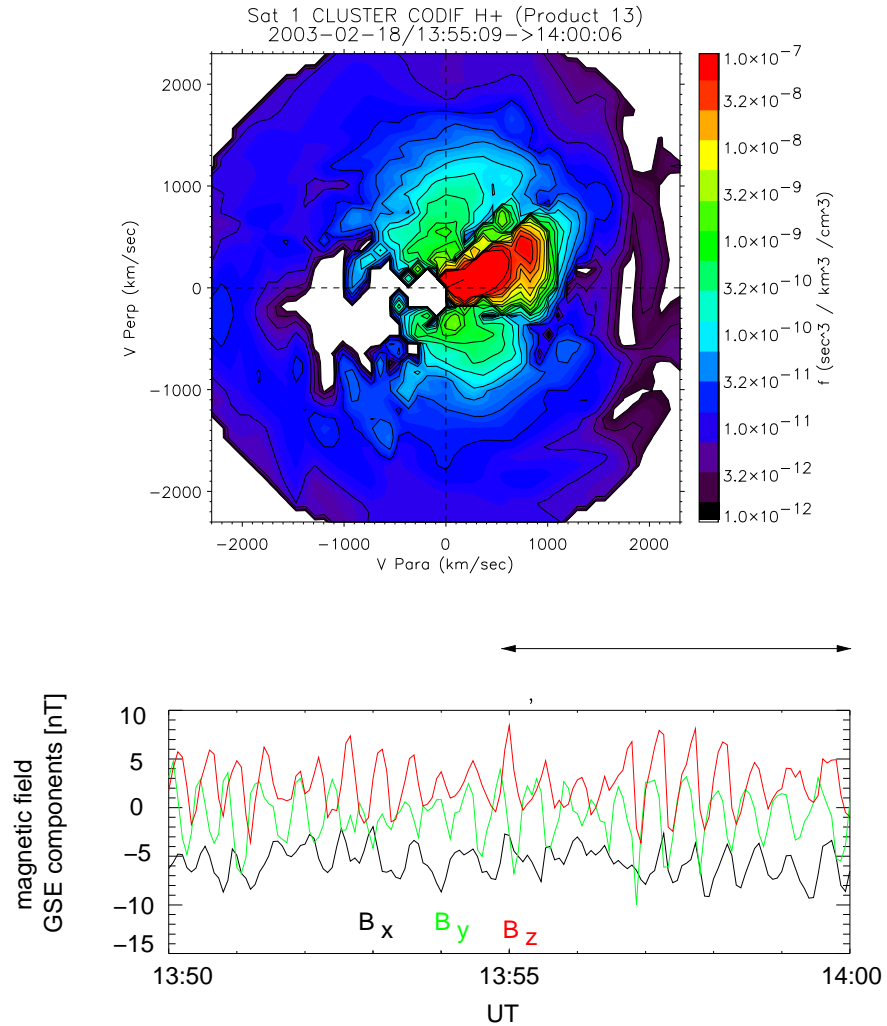
Figure 3.6: (For the general description of figure structure see caption of Figure 3.1) The upper figure presents the ion distribution between 13:55-14:00 UT. The diffuse ion distribution forms an almost totally isotropic, broad ring distribution, while the lower energy ions (former FAB ions) still form a kidney-shape distribution, but at this time the middle of the "kidney" is missing: this is due to the fact that those ions, which have larger parallel velocities oriented upstream, had already escaped from this region, while ions having a pitch angle closer to 90°, are convected deeper into the foreshock region by the solar wind, the remaining ions forming a toroidally-gyrating population.

1980; Thomsen, 1985) that a FAB can be observed in a narrow region near the ion foreshock boundary. The FAB ions are solar wind ions reflected at the quasi-perpendicular side of the bow shock. After their reflection these ions travel in the upstream direction along the magnetic field with a velocity around twice the solar wind bulk velocity (in the plasma frame). The reflection occurs as a result of the "head-on" collision of the solar wind ions with the shock wave. Note that the term "collision" is used as a more general term since the plasma is collisionless. In this case the word collision is used to describe an interaction between the ions and the shock wave which results in reflection. The investigation of the reflection mechanism is not the subject of this study.

In order to verify that the beam observed by the SC1 is indeed a beam formed by reflected ions we need to analyse the beam distribution. In Figure 3.7 (and also in Figure 3.3) it can be observed that the peak value of the beam flux in the velocity space is located at $v_\parallel \sim$-750 km/s and $v_\perp \sim$500 km/s. This gives a total beam ion velocity of $\sim$ 900 km/s. Note that these velocities are observed in the spacecraft frame. It was mentioned before that in the solar wind plasma there is a "frozen-in condition", which means that the magnetic field is convected by the solar wind plasma. Therefore a spacecraft situated in the upstream region is able to observe the particle velocity which is the resultant velocity of the particle movement along the magnetic field and the convection of the field by the plasma. The direction of the magnetic field is known at the time of the observation as well as the velocity and the direction of the plasma convection, the latter is in fact the solar wind bulk velocity. Using these data we (re)computed the beam ion velocity and direction in the plasma frame. Results show that the beam observed at $\sim$12:25 UT by the SC1 is an ion beam which consists of ions which propagate along the magnetic field with a velocity of 1300 km/s in the plasma frame. Since the solar wind velocity at this time is $\sim$650 km/s (i.e.

half the beam velocity) we conclude that the ions forming the beam indeed are reflected solar wind ions.

In order to prove that the beam ions are reflected at the quasi-perpendicular side of the bow shock we need to investigate the constellation between the spacecraft and the bow shock. Figure 3.8 is a reconstruction of the foreshock geometry (i.e. bow shock location, average magnetic field direction, spacecraft position, FAB propagation direction) projected into the $x_{GSE} - z_{GSE}$ plane. It can be seen, that the FAB originates at the quasi-perpendicular side of the shock (i.e. where the magnetic field direction is almost perpendicular to the shock wave normal direction).

In Figure 3.3 and Figure 3.7 besides the peak denoting the FAB, a higher-energy population can also be observed. This latter population can be regarded as a high-energy tail of the FAB ions which most probably consist of Shock Drift Accelerated (SDA) ions coming from the quasi-perpendicular side of the shock. In addition to the beam ions in the distribution we can observe the presence of ~ 30 keV ions (i.e. ions with velocities higher than ~ 2000 km/s). The geometrical configuration of the foreshock region does not allow the spacecraft to be reached by 30 keV energy ions coming from the quasi-perpendicular side of the shock. Instead, the 30 keV particles come from the quasi-parallel side of the shock. This can be seen in Figure 3.8 where the point of origin and the path of propagation is denoted in dark blue for the zero pitch angle 30 keV particles. In the schematic is also denoted the 10 keV particles path and the point of origin on the bow shock surface. The point of origin and the path of the 10 and 30 keV particles has been calculated using the same technique as described previously for the field-aligned beam; i.e., it has been taken into consideration that these particles propagate along the magnetic field lines while the magnetic field is convected by the solar wind plasma flow.

The important feature of this situation is that the spacecraft is able to

observe particles coming from the quasi-parallel and the quasi-perpendicular side of the shock simultaneously, or in other words it can observe the field-aligned beam and higher energy, shock-accelerated ions at the same time. This results in a superposition of the different ion populations and explains why besides the FAB a half-ring of higher-energy ions is present in the distribution.

The region where the FAB is to be found is a wave-free region therefore in this region the ions are not pitch-angle scattered. The lack of waves (and therefore the lack of backscattering) explains why we see only a half-ring of diffuse ions. The half-ring of the diffuse ion distribution is situated on the left side of the velocity space. This means that all these ions forming the half-ring are free to propagate in the upstream direction along the magnetic field; this region in the space act as a free-escape boundary for these ions. Note that the observation is in good agreement with the theory of diffusive acceleration which in order to explain the spectral shape of the energetic ions upstream of the bow shock accepts the concept of a free-escape boundary.

But there is a problem with this explanation. To fully understand the problem we need to recall some elements of the previous results. First, the diffuse ions are most probably bow shock accelerated ions, as we demonstrated it in Chapter 2. Second, the characteristic distribution for the diffuse ions is the broad, ring-like shaped distribution. Third, where diffuse ions are observed there are also low-frequency magnetic fluctuations to be found. In other words, the diffuse ions excite waves and the waves are scattering the ions in pitch angle; this interaction results in the ring-shape distribution of diffuse ions. However in the ion distribution at $\sim$ 12:25 UT (in Figure 3.3 and Figure 3.7) we see a half-ring of diffuse ions superposed to the FAB ions in the presence of no waves. This seems to be in contradiction with what we know about the diffuse ions. To answer the problem posed by this contradiction we need to point out that the region under discussion is the ion

foreshock boundary which is at substantial distance from the quasi-parallel side of the bow shock. At this point of the upstream region the diffuse ion density/flux is so small, that it might not be able to generate waves efficiently. Results show that shock-accelerated ions which can be identified as diffuse ions deeper in the foreshock region are capable of reaching the wave-free upstream boundary and escaping upstream. This fact points into the direction that the generally accepted picture, according to which the diffuse/energetic ions are to be found only deeper in the foreshock region, might not be completely accurate. It seems that one could expect to find (formerly diffuse) higher-energy ions (i.e. above $\sim$ 15-20 keV) even upstream of the field-aligned beam, upstream of the foreshock region. In order to verify this hypothesis more investigation need to be performed based on new spacecraft data. The spacecraft would need high sensitivity plasma instruments and would need to have a more extended orbit than Cluster has.

In the following the discussion concentrates on the FAB ion population, noting that these ions are observed together with a higher-energy ion population and all the distributions are a superposition of ions coming from the quasi-parallel *and* the quasi-perpendicular side of the bow shock.

We have already discussed a few elements of the FAB distribution observed by the spacecraft between 12:20-12:25 UT, and it has been mentioned that the magnetic field associated to the FAB distribution is wave-free. When two plasma beams interact, it is known that waves are produced through ion-ion beam instabilities. These waves are mostly circularly polarized transverse waves propagating along the magnetic field in the upstream direction with a velocity $\sim$ v$_{\text{Alfvén}}$, which in our case is $\sim$ 80 km/s. Since the solar wind velocity is $\sim$650 km/s, it is obvious that the generated waves are immediately convected in the downstream direction with a velocity $\sim$575 km/s (here we have taken into account that the waves are propagating along the magnetic field). This explains why we are able to observe the two plasma beams (i.e.,

the solar wind and the field-aligned beam) but not the generated waves.

At $\sim$ 12:40 UT the spacecraft is situated deeper in the foreshock region (Figure 3.4 and Figure 3.7). It can be seen that in this region there are small amplitude waves. These waves are pitch-angle scattering the FAB ion population around a circle with a center point depicted by the solar wind beam position (since the ion energy is preserved in the solar wind frame). The distribution shows that the originally concentrated ion beam now has a more kidney-shaped distribution meaning that some of the ions started to aquire larger pitch angle values. In addition it can be observed that the former higher-energy ion half-ring started to form a ring (finger-shaped deep blue-violet in color, at the right hand side of the distribution figure), however the ring is not complete at this time. At a later time period, between 13:25-13:30 UT, the spacecraft is situated even deeper in the foreshock region than at 12:45-12:50 UT because its inbound orbit. The large-amplitude waves can be observed in the figure. These waves are efficiently scattering the particles. In Figure 3.5 and 3.7 the diffuse ion distribution is a closed, broad ring-like distribution showing that substantial amount of higher-energy ions are backscattered. The lower energy former FAB ions still have a kidney-shaped distribution, but compared to the distribution observed at 12:45-12:50 UT this distribution has a more elongated kidney-shape, similar to a half-ring. This shows that at this time part of the ions are gyrating (i.e. have a large pitch angle) with positive parallel velocity oriented towards the shock. In velocity space the intensity of ions having pitch angles close to zero (i.e. maximum parallel velocity in the upstream direction) is very low. Evidently, this is a result of the pitch-angle scattering process combined with convection from the solar wind; or in other words is the result of the velocity filter effect. The velocity filter effect spatially separates the ions having different pitch angles but the same energy. Ions with maximum parallel velocity (i.e. with pitch angles close to zero) oriented upstream along the magnetic field lines

are moving out from the region where the ions with larger pitch angles are to be found. The hole in the kidney-shaped distribution shows the spatial separation of ions with different pitch angles.

The final phase of this process can be observed at 13:55-14:00 UT (Figure 3.6) where it can be seen that only toroidally gyrating ions are present at this region of the foreshock. As the large hole at the center of the distribution shows, all former FAB ions with smaller pitch angles are missing. The higher-energy diffuse ions still present a broad, ring-like distribution, a typical distribution of the "deeper" foreshock region.

To summarize, the scenario described above shows how FAB ions are scattered into an intermediate and later into a toroidally gyrating distribution while part of the ions are "lost" in the process. The waves generated by the beam disruption near the foreshock boundary are obviously convected to the shock together with "remnants" of the original field-aligned beam ion population (this is discussed in more details in Chapter 4). These ions already have a higher energy than the solar wind ions, therefore are more likely backscattered upstream after escaping the shock in the upstream direction. In front of the shock these particles can be scattered in pitch angle by the convected waves from the ion foreshock boundary and turned back to the shock. To conclude, our results show that the scattered FAB ions by moving to the shock might play an important role in the acceleration process at the parallel bow shock. In addition it seems that the bow shock accelerated ions by being able to reach the ion foreshock boundary can escape the ion foreshock region through the wave-free region where the FAB is to be found.
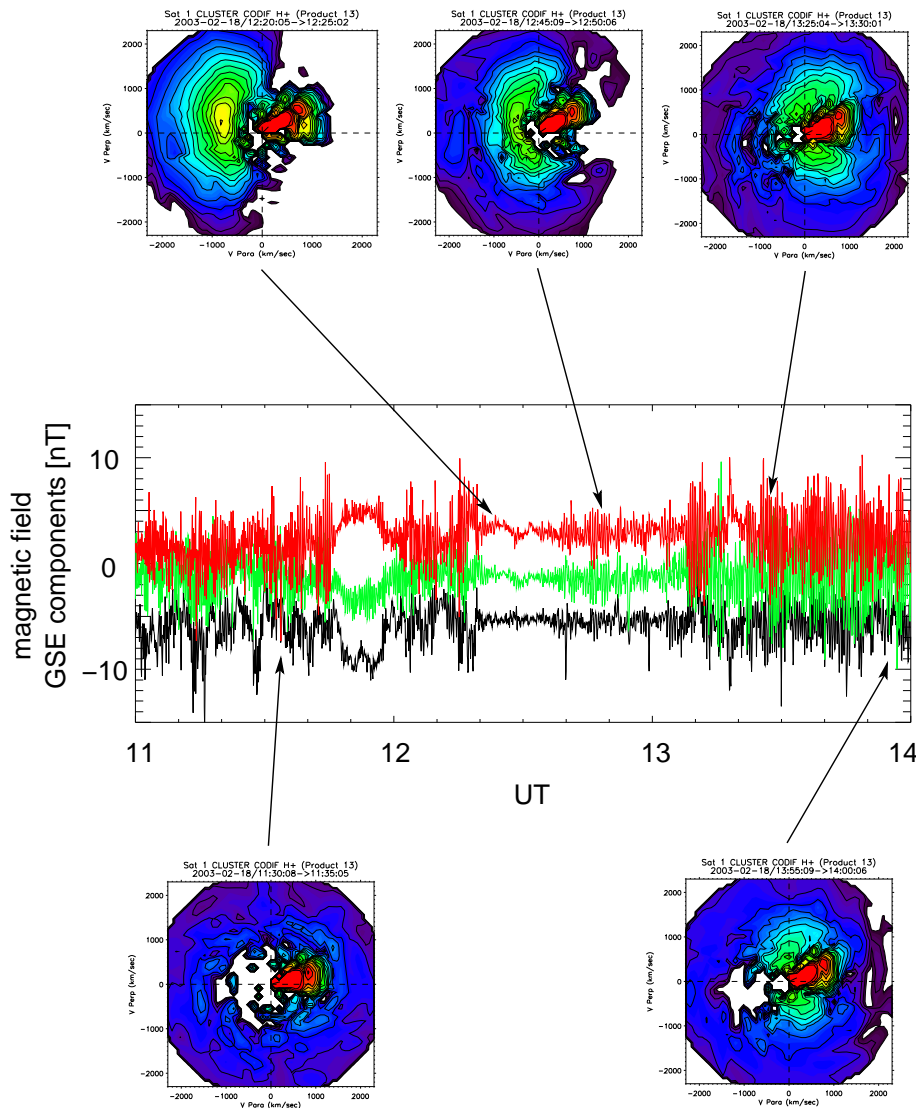
Figure 3.7: On the middle figure are presented the magnetic field components for the time period between 11:00 and 14:00 UT. In the upper and lower panels the relevant ion distributions are shown, the arrows pointing at the associated magnetic field at the time when the distributions are observed. The lowest two distributions present the upstream ion distribution before the observation of the FAB (left) and the ion distribution long after the FAB has been observed. Note the striking similarity between the two distributions; the only difference is that at the right-side distribution a toroidally gyrating distribution is present, the "remnants" of the original FAB.
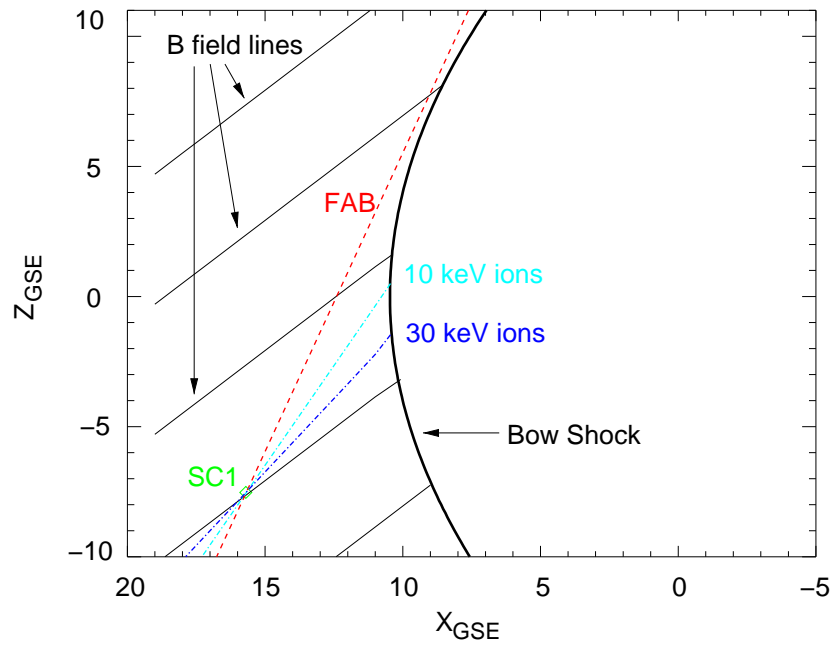
Figure 3.8: The figure shows the foreshock geometry reconstruction at the time when the spacecraft (green diamond) observes the FAB, projected into the x-z plane. It can be seen that the spacecraft can simultaneously observe ions originating at the quasi-perpendicular and the quasi-parallel side of the shock, which results in a superposition of the higher-energy diffuse and the lower-energy FAB ion population.

Chapter 4

Magnetohydrodynamic Waves
in Front of the Bow Shock

4.1   Observations

The continuous magnetic connection of the spacecraft to the quasi-parallel
side of the bow shock during 18 February, 2003 upstream ion event provides
an excellent opportunity to study the low-frequency magnetic waves and their
relation to the upstream energetic particles as a function of distance from the
shock. As mentioned before, the interplanetary magnetic field is unusually
quiet and has a very stable direction. Under normal solar wind conditions
the interplanetary magnetic field usually contains large amplitude, low fre-
quency fluctuations. These fluctuations are absent during 18 February, 2003
upstream ion event. This allows us to study the bow shock related magnetic
waves in much deeper detail. During this event the ion-generated waves can
be identified with much more certainty because we do not have other sources
for waves. It will be shown that the waves are a superposition of waves gen-
erated near the foreshock region by the field-aligned beam (FAB) and waves
generated deeper in the foreshock region by higher energy diffuse ions. The

study reveals important details about the foreshock structure. Based on the obtained results, we were able to identify regions with substantially different coupling between waves and energetic ions.

As it has been shown previously, Cluster encounters the field-aligned beam (FAB) before 14:00 UT. In order to ensure that the spacecraft is situated deep in the foreshock region, the studied time period is set from 15:00 UT to $\sim$ 22:00 UT, the end of the time period being triggered by the time when the SC1 crosses the shock front (at $\sim$ 22:41 UT). The analysis is based on data provided by the FGM and the CIS HIA analyser on SC1. The long, uninterrupted magnetic connection of the spacecraft to the quasi-parallel side of the bow shock allows a detailed study of the magnetic wave activity as a function of distance from the shock front. The spacecraft distance to the shock was calculated in a similar way as described previously for the gradient study, the only difference being that the average distances were calculated for a time period of 10 minutes. Beginning with 15:00 UT, 10 minute time periods were taken, the average distance to the shock was calculated and the wave analysis was performed.

To separate the compressional waves from the transverse ones, the magnetic field was averaged over ten minutes. The averaged magnetic field direction was used to define a new cartesian coordinate system, which has the x axis pointing into the average magnetic field direction, the other two axis, y and z being perpendicular to x and also to each other. In the following this new coordinate system will be referred to as the Averaged Magnetic Field System (AMFS). The 1 spin time resolution magnetic field data (measured in GSE) has been transformed into the AMFS coordinates in the 10 minute time frame where the AMFS is defined by the average magnetic field. The described method proved to be adequate for the study as the magnetic field direction was very steady. After transforming the magnetic field vector components into one compressional and two transverse components, a fast

Fourier analysis (FFT) was performed for each 10 minute time period in order to derive the power spectrum of the magnetic waves. Figure 4.1 presents the total magnetic field spectrum for the time period between 17:00 and 17:30 UT. The plot also presents the power spectrum for the magnetic field measured by the ACE spacecraft Magnetometer Instrument (MAG) (Smith et al., 1998) located far upstream, at a distance of ~ 235 R_e from the Earth. The comparison of the magnetic field power spectra measured by SC1 and ACE clearly demonstrates that the waves observed by SC1 in the foreshock region are generated locally by energetic particles. The wave power at ACE is significantly lower than at SC1.

The fact that the energetic ions and the associated large-amplitude magnetic waves have a one-to-one correlation has been demonstrated many times. According to the quasi-linear theory these waves scatter the particles in pitch-angle, energetic ions are scattered by those waves which have frequencies equal to the resonance frequency of the particles. On the other hand, these waves are produced by the particles. The coupling between waves and energetic ions was described in a self-consistent model by Lee (1982) for the quasi-parallel shock configuration. Lee's theory was verified by Trattner et al. (1994) by performing a statistical analysis over more than 300 upstream ion events. They found that the measured energy density of upstream waves is in excellent agreement with the wave energy density predicted by the model of Lee.

4.1.1   Resonance Frequencies

Let us assume that the waves propagate parallel or antiparallel to the magnetic field. In the case the waves have frequencies below the proton cyclotron frequency, they fulfill the approximate dispersion relation
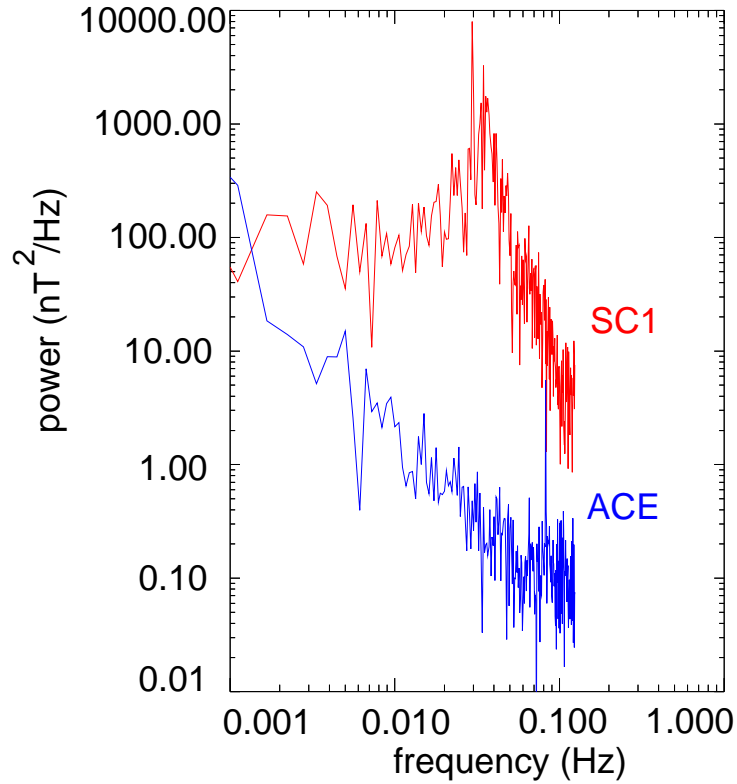
Figure 4.1: The total magnetohydrodynamic wave power observed by SC1 on 18 February, 2003, between 17:00 and 17:30 UT, when the spacecraft was situated deep in the foreshock region (red). To compare the wave intensity in the foreshock region with wave activity in the interplanetary magnetic field recorded far upstream, the figure also presents (blue) the total wave power observed by the ACE spacecraft at the same time period. The very significant difference in the wave intensity between the two locations demonstrates that in the foreshock region the waves are produced locally by energetic particles.

$$\omega = k \cdot v_A \tag{4.1}$$

where v_A is the Alfvén wave velocity. Note that in our case k is negative, since the waves under investigation are propagating in the upstream direction (Hoppe and Russell, 1983) , while the magnetic field vector points towards the shock. The Doppler-shifted frequency is given by

$$\omega^* = k \cdot v_A + \vec{K} \cdot \vec{v}_{sw} \tag{4.2}$$

where the * represents the quantities measured in the spacecraft frame and v_{sw} is the solar wind velocity. This equation can be written as:

$$\omega^* = k \cdot v_A - k \cdot v_{sw}(\vec{b} \cdot \vec{w}) = \omega\left(1 - \frac{v_{sw}}{v_A}(\vec{b} \cdot \vec{w})\right) \tag{4.3}$$

where $\vec{b}$ and $\vec{w}$ are the units vectors pointing in the direction of the magnetic field and the solar wind velocity, respectively.

The resonance condition in the solar wind frame can be written as

$$\vec{v}_R = \vec{v}_\parallel = \left(\frac{\omega + \Omega_{ci}}{k}\right)\vec{b} = \vec{b} \cdot v_A\left(1 + \frac{\Omega_{ci}}{\omega}\right) \tag{4.4}$$

where $\vec{v}_R$ is the resonance velocity, Ω_{ci} is the proton cyclotron frequency and $\vec{v}_\parallel$ is the parallel velocity of the particle.

Expressing the angular frequency ω in terms of the angular frequency in the spacecraft frame, ω^*, we obtain for the resonance frequency

$$\vec{v}_R = \vec{b} \cdot v_A\left(1 + \frac{\Omega_{ci}}{\omega^*}\left(1 - \frac{v_{sw}}{v_A}(\vec{b} \cdot \vec{w})\right)\right) \tag{4.5}$$

Between the frequency and the angular frequency the following relations hold:

$$f_{ci} = \frac{\Omega_{ci}}{2 \cdot \pi} \qquad \text{and} \qquad f^* = \frac{\omega^*}{2 \cdot \pi} \tag{4.6}$$

Using the above relation the resonance velocity can be expressed as:

$$\vec{v}_R = \vec{b} \cdot v_A \left(1 + \frac{f_{ci}}{f_r^*} \left(1 - \frac{v_{sw}}{v_A} (\vec{b} \cdot \vec{w}) \right) \right) \tag{4.7}$$

where f_r^* is the resonance frequency for the ions with parallel velocity equal to $\vec{v}_R$. Taking into account that the particles propagate antiparallel to the magnetic field into the upstream direction, the resonance frequency can be expressed by the following formula:

$$f_r^* = -\frac{f_{ci} \cdot v_A}{v_R + v_A} \left(1 - \frac{v_{sw}}{v_A} (\vec{b} \cdot \vec{w}) \right) \tag{4.8}$$

4.2   Discussion

Equation 4.8 shows that particles with different parallel velocities have different resonance frequencies. In other words, particles with a certain parallel velocity (irrespective of their energy) are pitch-angle scattered by waves of a specific frequency, the resonance frequency being a function of the plasma parameters. The plasma parameters of interest are the solar wind bulk velocity (v_{sw}), the Alfvén speed (v_A) and the proton cyclotron frequency (f_{ci}). For the 18 February, 2003 upstream event these parameters were: $v_{sw} \sim$650 km/s, $v_A \sim$82 km/s and $f_{ci} \sim$0.099 Hz. Taking into account the direction of the solar wind bulk velocity related to the magnetic field direction we obtain $\vec{b} \cdot \vec{w} \sim$0.95. Using the above parameter values the resonance frequency was calculated for the FAB, the 10 keV and the 32 keV energetic ions at zero pitch angle. The FAB ions are protons with a velocity of $\sim$900 km/s in the spacecraft frame (see Chapter 3 for more details) which corresponds to an energy of $\sim$4.2 keV. The obtained resonance frequencies in the spacecraft frame for FAB (i.e. 4.2 keV), 10 keV and 32 keV ions are $\sim$0.038 Hz, $\sim$0.028 Hz and $\sim$0.017 Hz, respectively. Figure 4.2 presents the resonant frequencies versus particle energy. According to Equation 4.8, the resonant frequency is

almost a power law function of the particle energy, decreasing toward higher particle energies.

In Figure 4.1 the peak in the total magnetohydrodynamic wave power observed by SC1 corresponds to the resonance frequency of the FAB ions, ~ 0.035 Hz. In order to separate the waves produced by the FAB ions near the foreshock boundary and the waves produced by the diffuse ions deeper in the foreshock region, two frequency intervals have been choosen: one between 0.03 and 0.05 Hz, and a second between 0.017 and 0.028 Hz. The first frequency interval covers the waves produced by the FAB ions, the second one the waves produced by the diffuse ions with energies between 10 and 32 keV. Over these intervals the wave power was integrated and the wave energy was derived. Figure 4.3 presents the energy of the "peak" (i.e. energy of the waves produced by FAB ions) versus distance from the shock. It can be seen that the wave energy in this frequency range remains fairly constant as the spacecraft approaches the shock. This result is in good agreement with the conclusions of the previous chapter, where it was suggested that the beam produces waves which are convected to the bow shock by the solar wind plasma flow.

The situation is different when considering the wave energy over the frequency range which is in resonance with higher-energy (i.e., diffuse) ions, as it can be observed in Figure 4.4. The compressional wave energy density grows exponentially as the shock is approached, while the transverse wave energy density shows large fluctuations independent of distance from the shock.

Hoppe et al. (1981) demonstrated that the energetic ions upstream of the Earth's bow shock are accompanied by large-amplitude $\delta B \sim B$ magnetic waves of their own making in the range from 0.01 to about 0.3 Hz and showed that the wave power peaks at ~ 0.03 Hz. These waves are mostly transverse but occasionally may have strong compressional components with large fluctuations of the magnetic field strenght and the solar wind density

when the variations have steepened into shocklets. The coupling between diffuse ions and waves was described by Lee (1982) in a self-consistent model for the quasi-parallel shock configuration. One important element of this model is the relation:

$$W_B = 6.57 \cdot \beta^2 \frac{v_A}{v_{sw}} W_p \qquad (4.9)$$

i.e., there is a direct, intimate coupling between the energetic particle and magnetic wave energy density (i.e. W_p and W_B, respectively). The parameter β can be expressed as

$$\beta = \left(\frac{1}{3}\right)\left(1 - \frac{N_{us}}{N_{ds}}\right) \qquad (4.10)$$

where N_{us}/N_{ds} is the ratio of the upstream and downstream plasma density, v_A is the Alfvén velocity and v_{sw} is the solar wind velocity. In expression 4.9 there is a factor of 2 difference compared to that of Lee (1982). As noted by Trattner et al. (1994), the difference is due to an omission of a factor 2 in the denominator of Lee's equation. Möbius et al. (1987), after analysing two upstream ion events observed by the AMPTE/IRM satellite, found good agreement of the predicted and measured wave energy density.

Trattner et al. (1994) extended this study on a statistical basis for the complete set of AMPTE/IRM data upstream of the bow shock and also found a remarkable high correlation of 0.89 between the predicted and observed wave energy density. They also point out that the correlation describes the local coupling between the wave and the foreshock ion energy, i.e. the correlation is independent of the strenght of an event and its position relative to the shock. However, until now there has been no study which investigates the relation between the predicted and observed wave energy density as a function of distance from Earth's bow shock. Because its favorable geometrical configuration, the 18 February, 2003 upstream ion event (i.e. the continous

magnetic connection of the spacecraft to the quasi-parallel shock) allows a detailed investigation of the applicability of Lee's theory as a function of distance from the shock. The upstream ion solar wind number density (N_{us}) during this event is ~2.69 cm^{-3}, while the downstream ion number density (N_{ds}) is ~9.2 cm^{-3}, which results in a compression ratio of ~ 0.3. Substituting this ratio into Equation 4.9 gives ~0.21 for the parameter β. In order to derive the predicted wave energy density the particle energy density needs to be calculated. Figure 4.5 presents the ion energy density as a function of distance from the shock for the ions between 10 and 32 keV. The ion energy density was obtained using the partial ion density data provided by the four upper energy levels of the HIA instrument (i.e. at energies between 10-32 keV). The energy density values were binned over 0.5 R$_e$ distances. As the figure shows, the ion energy density increases exponentially with decreasing distance from the shock; however with a significantly stronger increase for distances ≤3R$_e$. In other words, the e-folding distance of the energetic ion density is smaller close to the shock. According to diffusive transport theory, the exponential decrease of energetic ion density is the result of pitch-angle scattering by self-induced, transverse magnetic waves. Therefore one would expect a larger transverse wave energy density closer to the shock. It should be noted that Equation 4.9 precisely expresses this relation. Our results, however, are in disagreement with this prediction close to the shock, as it can be seen by comparing Figure 4.5 with Figure 4.4. The comparison shows that below ~ 3R$_e$ distance from the shock, i.e., in the region where the particle energy density is increasing considerably, the transverse wave energy density is constant or slightly decreases.

In order to quantify the relation between the predicted and observed wave energy density, the predicted wave energy density has been computed using the relation 4.9 and its ratio to the observed wave energy density has been derived. Figure 4.6 presents the ratio of the predicted and observed trans-

verse wave energy density versus distance from the shock. According to this figure, the area in front of the shock can be divided into two regions. In the region with a distance larger than $\sim 3R_e$ the theory predicts the wave energy density well. In the region below $\sim 3R_e$, the theory breaks down: the observed wave energy density is substantially lower than the predicted one. Hence, this closer region presents a region of high particle energy density. This result is striking, as in the absence of sufficient pitch-angle scattering provided by transverse waves in the appropiate frequency range, the energetic particles should quickly escape the region and yet their behaviour does not reflect this. To conclude, the region closer to the shock exhibits some unique characteristics: trapping of energetic particles in the presence of lower than expected transverse wave activity, while the compressional wave energy density continues to increase exponentially towards the shock to a value similar to the transverse wave energy density. Therefore, this highly compressive region, i.e., the region below a distance of $\sim 3R_e$ from the shock, can be regarded as part of the shock itself, where shock reformation takes place.
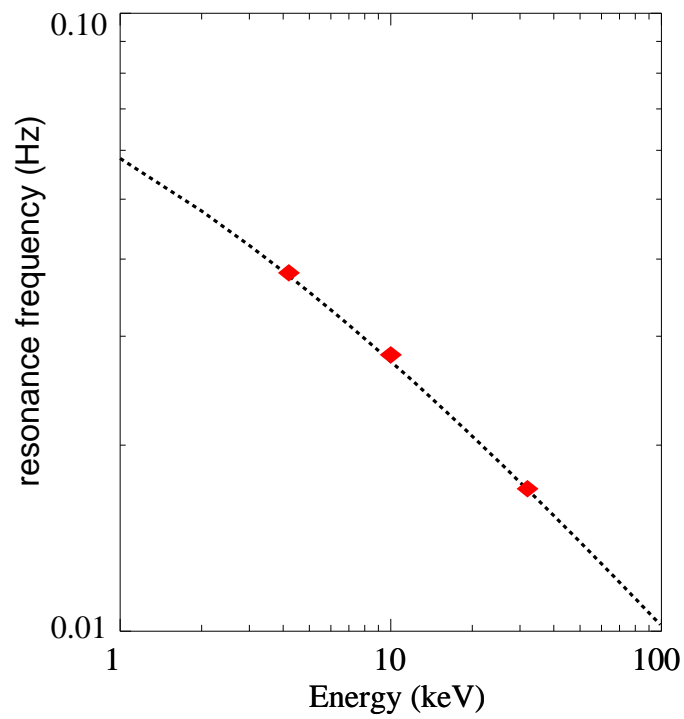
Figure 4.2: Resonant frequency vs energy for backstreaming ions assuming zero pitch angle. The red diamonds show the resonant frequencies for FAB, 10 keV and 32 keV energetic ions.
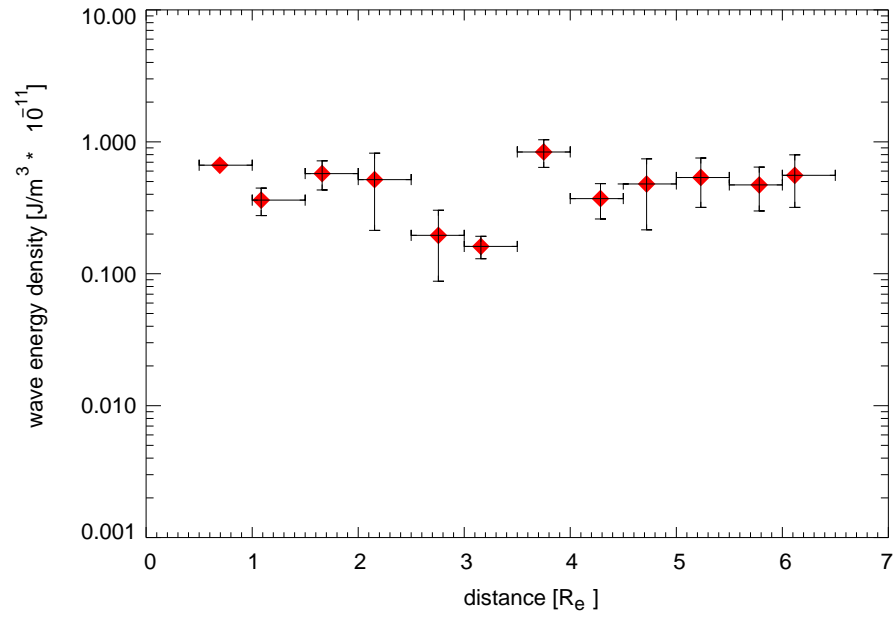
Figure 4.3: In the figure the wave energy is presented in the frequency range which is resonant with the FAB ions vs distance. The wave energy does not show significant variation in its value as a function of distance from the shock. This is taken as evidence that these waves are produced by the beam near the foreshock upstream boundary and are convected by the solar wind plasma to the shock.
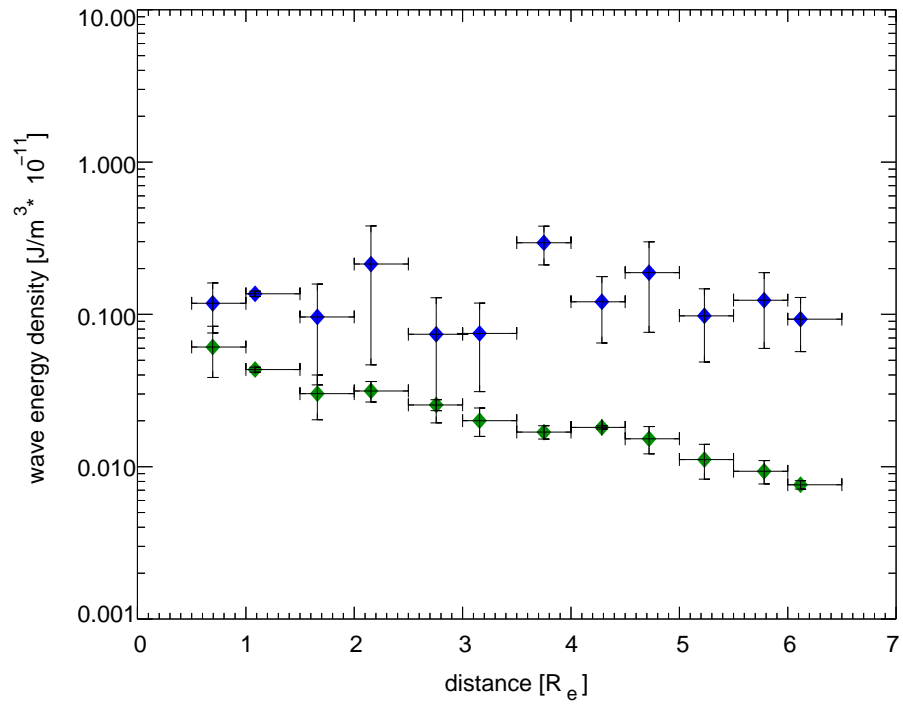
Figure 4.4: The figure shows the transverse (blue) and compressional (green) wave power in the frequency range which is in resonance with ions in the energy range between 10 and 32 keV. It can be observed, that while the compressional wave energy increases exponentially with decreasing distance from the shock, the transverse wave energy density shows large fluctuations independent of distance from the shock.
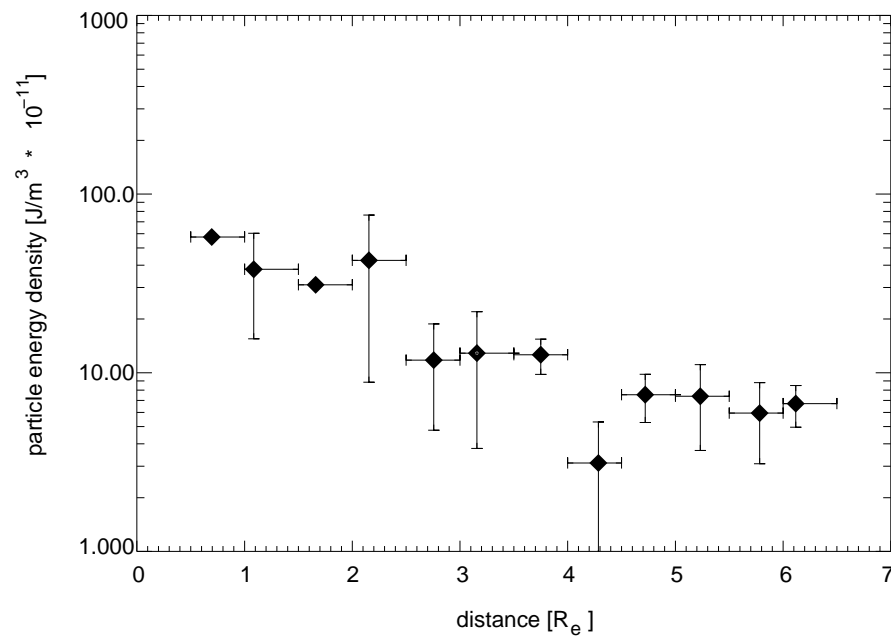
Figure 4.5: The energetic particle energy density versus distance for ions between 10 and 32 keV.
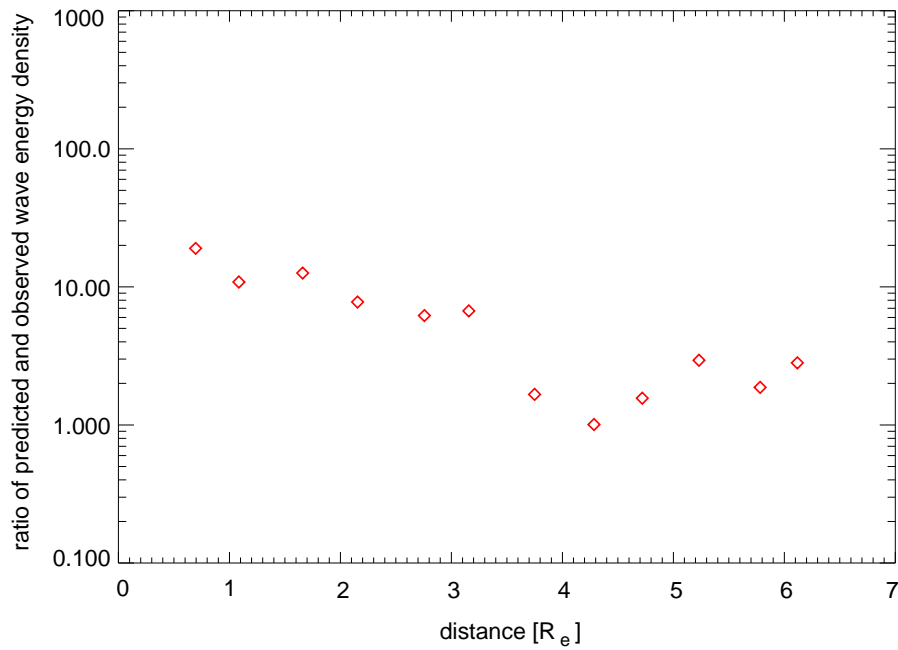
Figure 4.6: The ratio of the predicted and observed wave energy density as a function of distance from the shock. The predicted wave energy density has been derived using Equation 4.9 (Lee, 1982). It can be observed that near to the shock, below $\sim 3R_e$, the observations do not match the prediction, while above $\sim 3R_e$ the agreement is satisfactory.

Chapter 5

Simulation Results

In this chapter we compare the spacecraft observations with results obtained by performing a simulation. The simulation answers the question whether the exponential growth of the compressional wave energy density in front of the quasi-parallel shock observed during the 18 February, 2003 upstream ion event was a unique occurence, or is a general property of a quasi-parallel shock. In addition the simulation provides the opportunity to study in detail how the field-aligned beam ions are scattered in the foreshock region.

5.1 The Hybrid Simulation Code: Basic Assumptions and Equations

The basic principle of a hybrid code is that the ions are treated kinetically while the electrons are regarded as an eletrically neutralising fluid. The different treatments for ions and electrons makes possible the modelling of physical processes in a collisionless space plasma which occur on shorter time and distance scales that can be treated by magnetohydrodynamics, yet do not need an electron scale resolution like electron gyroradius and inverse

electron gyrofrequency. Therefore the hybrid code is well suited to study ion processes in a plasma without using full particle simulation codes which require significantly more time to run and enormous computer capacity.

The relevant scale of the ion processes in a plasma are the ion gyroradius and the ion inertial lenght on the spatial scale and the inverse ion gyrofrequency on the time scale. In real space this corresponds to a length scale from 10's to 100's of kilometers and a timescale of the order of seconds. These spatial and temporal ion scales are resolved by satellite instruments which makes the hybrid code a valuable tool for understanding the data recorded by spacecraft, but also for expanding the general knowledge about plasma ion processes.

In the hybrid model the ions are treated kinetically by using standard particle-in-cell technique (elements of this technique are described below). Each macro-ion with charge q_i and mass m_i is subject to the equation of motion in an electromagnetic field:

$$m_i \frac{d\vec{v_p}}{dt} = q_i \left(\vec{E} + \frac{\vec{v_p} \times \vec{B}}{c} \right) \tag{5.1}$$

$$\frac{d\vec{x_p}}{dt} = \vec{v_p} \tag{5.2}$$

where $\vec{E}$ and $\vec{B}$ are the electric and magnetic fields, $\vec{x_p}$ is the particle position vector and $\vec{v_p}$ is the particle velocity. The field vectors $\vec{E}$ and $\vec{B}$ have values given on a spatial grid and are interpolated to the particle location. After all the particles have been moved according to the equation of motion, the particle information is assembled at the grid points to derive the ion number density n_i, charge density $n_i q_i$, bulk ion flow velocity $\vec{V_i}$ and the ion current $\vec{J_i}$. The ion current is calculated by using the equation:

$$\vec{J_i} = n_i q_i \vec{V_i} \tag{5.3}$$

The electron momentum equation is

$$n_e m_e \frac{d\vec{V_e}}{dt} = -en_e \left(\vec{E} + \frac{\vec{V_e} \times \vec{B}}{c} \right) - \nabla \cdot \underline{\mathbf{P}}_e \qquad (5.4)$$

where $\vec{V_e}$ is the electron fluid velocity and $\underline{\mathbf{P}}_e$ is the electron pressure tensor. Since the electrons are treated as an inertia-less fluid, i.e. $m_e=0$, this implies:

$$n_e m_e \frac{d\vec{V_e}}{dt} = 0 \qquad (5.5)$$

in Equation 5.4.

The electronic effects on the electron Debye length scale are ignored, which implies that the plasma is quasi-neutral, meaning that the ion and the electron charge densities are equal:

$$n_e e = n_i q_i. \qquad (5.6)$$

Here n_e is the electron number density and $-e$ is the electron charge. In addition, in Equation 5.4 $\underline{\mathbf{P}}_e$ is usually taken as a scalar:

$$\underline{\mathbf{P}}_e = p_e \underline{\mathbf{1}} \qquad (5.7)$$

where $\underline{\mathbf{1}}$ is the unit matrix. Here should be noted that the resistive coupling between electrons and ions is left out from the equations, which adds a term $en_e \underline{\eta} \cdot \vec{J}$ to the right-hand side of Equation 5.4, where $\underline{\eta}$ is the resistivity and $\vec{J}$ is the total current.

To conserve the moment, $-e\underline{\eta} \cdot \vec{J}$ needs to be added also to the acceleration term in the equation of motion 5.1. For simplicity in the simulation the resistivity is taken usually as a scalar with constant value.

The electric and magnetic field is solved using Maxwell's equations in the low frequency approximation:

$$\nabla \times \vec{B} = \frac{4\pi}{c}\vec{J} = \frac{4\pi}{c}q_i n_i (\vec{V_i} - \vec{V_e}) \qquad (5.8)$$

and

$$\frac{\partial \vec{B}}{\partial t} = -c(\nabla \times \vec{E}) \tag{5.9}$$

where Equation 5.6 was taken into consideration and the left-hand side of Equation 5.9 is the partial time derivate of the magnetic field vector. These equations form a complete system (i.e., every unknown parameter can be calculated). Equation 5.8 is used to eliminate $\vec{V_e}$ in Equation 5.4 while Equation 5.9 is used to advance the magnetic field in time. The electric field can be obtained directly from Equation 5.4, since $m_e = 0$. The remaining two Maxwell equations are satisfied by boundary conditions and the quasi-neutral approximation (i.e. Equation 5.6):

$$\nabla \cdot \vec{E} = 4\pi(n_i q_i - n_e e) = 0 \tag{5.10}$$

and

$$\nabla \cdot \vec{B} = 0 \tag{5.11}$$

For a more detailed description of further assumptions incorporated in the hybrid code, like the various numerical implementations and time advance techniques see the volume "Space Plasma Simulation" (Eds: J. Büchner, C. T. Dum and M. Scholer).

In a hybrid simulation (because of reasons of convenience) the unit of distance is the ion inertial length (λ_i) and the unit of time is the inverse ion gyrofrequency (Ω_{ci}^{-1}), where Ω_{ci} is the ion gyrofrequency. The ion inertal length can be expressed as:

$$\lambda_i = \frac{c}{\omega_{pi}} \tag{5.12}$$

where c is the speed of light and ω_{pi} is the ion plasma frequency.

The simulation domain, or as it is sometimes called, the simulation box, is divided by a grid into unit cells. The size of a unit cell is comparable to the ion inertial length, usually the cell size is 0.5 λ_i. The time-step over

which each particle is moved and the field values are recalculated according to the new position of the particles, is taken as a fraction of the time unit; in most cases the timestep is set as 0.01-0.1 inverse ion gyrofrequency. This is necessary in order to avoid the appearance of numerical fluctuations during the simulation run.

5.2 Interaction of Field-Aligned Beam Ions with the Shock Wave

In order to study the electromagnetic waves in front of the quasi-parallel shock we performed a 1D (i.e. one-dimensional) hybrid simulation. The parameters of the simulation were set to provide a shock with $M_A \sim 8$ and $\Theta_{BN} \sim 20°$, similar to the values of the shock observed by Cluster on 18 February, 2003. During the 18 February, 2003 upstream ion event, SC1 recorded an exponential growth in compressional wave energy as it moved closer to the shock. We will compare the compressional wave growth observed by SC1 with the simulation results.

The simulation domain consists of 5000 cells in x direction, each cell has a dimension of 0.5 λ_i. In real space one ion inertial length corresponds to ~ 144 kilometers in our case, or in other words ~ 44 ion inertial lengths are equivalent to 1 R_e. The initial system consists of 800000 particles. This corresponds to $\sim$160 particles per cell. At each timestep a number of particles are injected at the left-hand side (LHS) of the system with a velocity of v=$6.15v_A$, modelling the solar wind (note that all the velocities are normalized to the Alfvén velocity). The right-hand side (RHS) of the system is a rigid wall. All the particles reaching the RHS are reflected. The reflected particles interact with the incoming "solar wind" particles through a self-consistent electromagnetic field resulting in a shock wave. The shock wave

moves in the negative direction (i.e. towards the LHS) with a velocity of $\sim$ -1.86 v_A, which results in a shock velocity equivalent to $\sim$ 8 M_A relative to the incoming particles. The LHS of the simulation domain is a free-escape boundary: each particle reaching the LHS is eliminated from the system. The simulation run time has been set to 675 Ω_{ci}^{-1}. During a test run, it was determined that after $\sim$ 337 Ω_{ci}^{-1} the low frequency electromagnetic waves are fully developed on the left side to the shock wave, i.e. in the upstream region. Figure 5.1 shows the magnetic field in the simulation box at 337 Ω_{ci}^{-1} after the beginning of the simulation. The shock at this time is located at $x \sim 1800\lambda_i$.

We performed an analysis of the magnetic waves at t=337 Ω_{ci}^{-1} when the upstream magnetohydrodynamic wave field was fully developed. The upstream region was divided into overlaping intervals of $500\lambda_i$ each. The interval size of 500 λ_i was necessary in order to examine the low frequency waves which are resonant with the high energy diffuse ions. The whole upstream region is $\sim 1500\lambda_i$ wide, the shock at this time is at $x \sim 1500\lambda_i$. The overlaping of the intervals made possible a wave analysis at five distances from the shock. The intervals over which the analysis was performed are between 0-500, 250-750, 500-1000, 750-1250 and $1000\text{-}1500\lambda_i$.

After the separation of the waves into transverse and compressional components, the frequencies were decomposed by a Fast Fourier Transformation (FFT) and the wave power was calculated. The wave power of the transverse and compressional components was numerically integrated over the frequency range which is resonant with ions having at least twice the solar wind bulk velocity. This way we obtained the magnetic wave energy over the frequency range of interest. The wave analysis was performed in a similar way as described in Chapter 4, where the magnetic data observed by SC1 is examined. In Figure 5.2 both the compressional and transverse waves grow almost exponentially with decreasing distance from the shock. This suggests that the
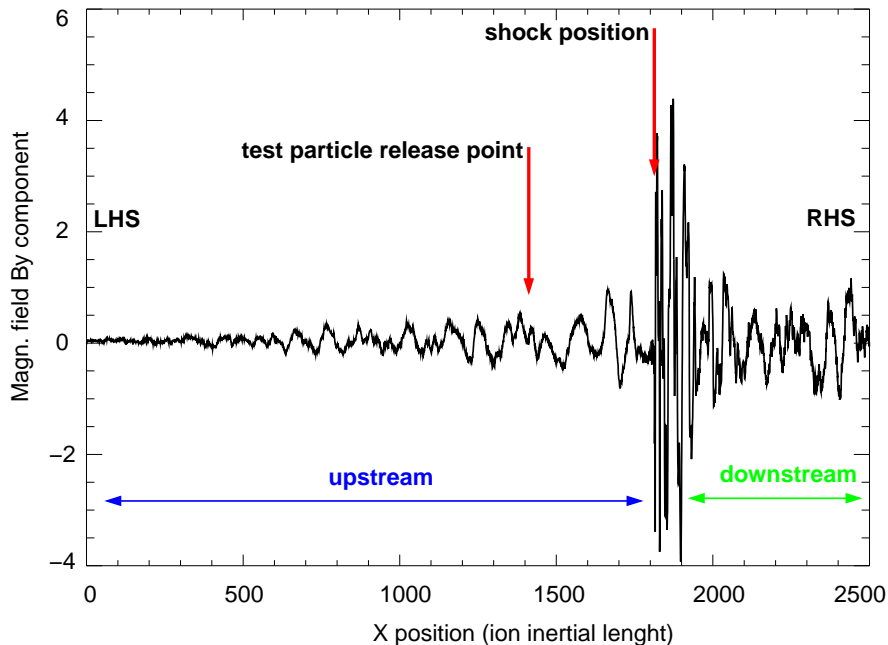
Figure 5.1: The figure shows the magnetic field B_y component after a time of
$337\ \Omega_{ci}^{-1}$ from the beginning of the simulation, when the test particles have
been released in the region in front of the shock.

compressional wave growth is a characteristic feature of the quasi-parallel
shock.

In addition to investigate electromagnetic waves upstream of the shock,
the purpose of the simulation is to investigate how an ion beam develops in
the upstream magnetic wave field. Therefore we examine the distribution
of beam ions at different distances from the shock. The field-aligned beam
in real space consists of reflected ions at the quasi-perpendicular side of the
bow shock. These ions travel into the upstream direction along the magnetic
field with a velocity of approximately twice the solar wind bulk velocity.
Because the magnetic field is convected by the solar wind, the FAB ions are
also convected into the foreshock region (i.e., to the quasi-parallel side of
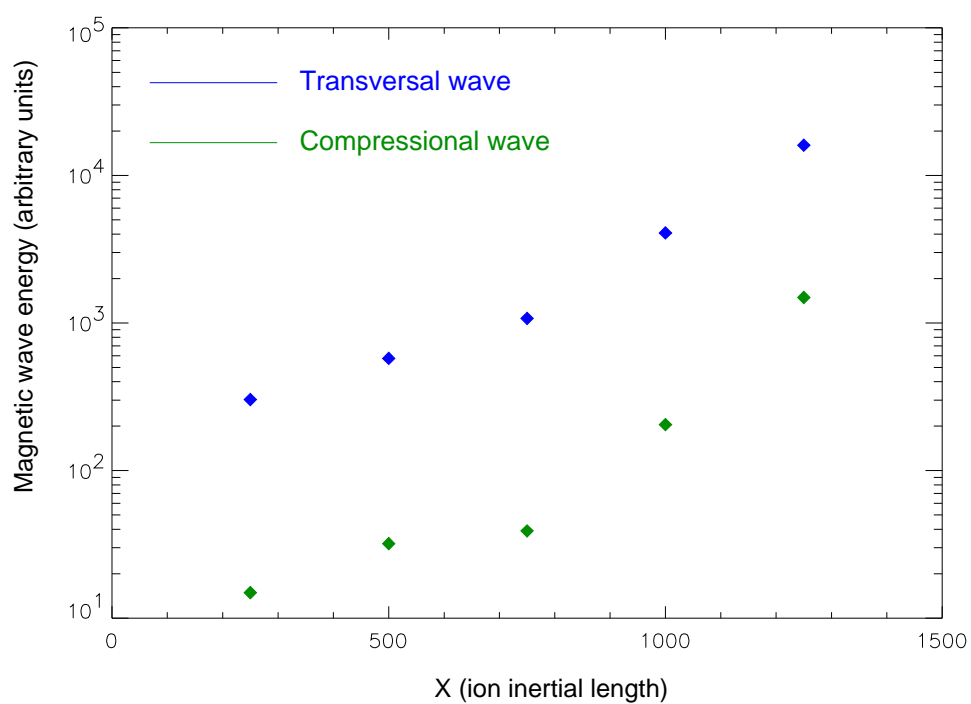
Figure 5.2: The figure presents the almost exponential growth of the magnetic wave energy in front of the shock in the frequency range which is resonant with the ions having at least twice the solar wind velocity.

the shock). To simulate the appearance of FAB ions upstream of the quasi-parallel shock, additional test particles were introduced in the simulation box with velocities characteristic of field-aligned beam ions. As mentioned before, at t=337 Ω_{ci}^{-1}, the shock and the upstream magnetic wave field was developed in a self-consistent way. At this time 12000 test particles have been released at $x \sim 1400$ λ_i in front of the shock, which is equivalent to $\sim$ 7 R_e distance from the shock in real space. The test particles were released with a velocity of $\sim$-12.7v_A parallel to the magnetic field in the upstream direction. (In the following we will refer to test particles as beam particles.)

The beam particles were followed after their release until the end of the simulation. The beam particles were also used to study how many of these particles move downstream and what is the percentage of particles involved in Fermi-acceleration at the shock; i.e. the effectiveness of Fermi-acceleration of these particles.

Figure 5.3 presents the beam particle number evolution over time in the different regions of the simulation domain. The released beam particles are scattered in pitch angle by the already existing waves. The scattering in velocity space also leads to scattering in real space, since the particles can move away from the shock or they can move closer to it, depending on their parallel velocity. When the beam particles reach the shock they can be accelerated and scattered back into the upstream region or they can travel downstream. Those particles which travel deep into the downstream region have a very small probability to reenter into the upstream region because of the high amplitude magnetic turbulance in the shocked downstream region; an obstacle which is very difficult to overcome. Therefore the particles need to stay close to the shock on the downstream side, or in other words they need to be efficiently scattered in pitch-angle in order to reenter into the upstream region.

Particles accelerated and backscattered into the upstream region are again
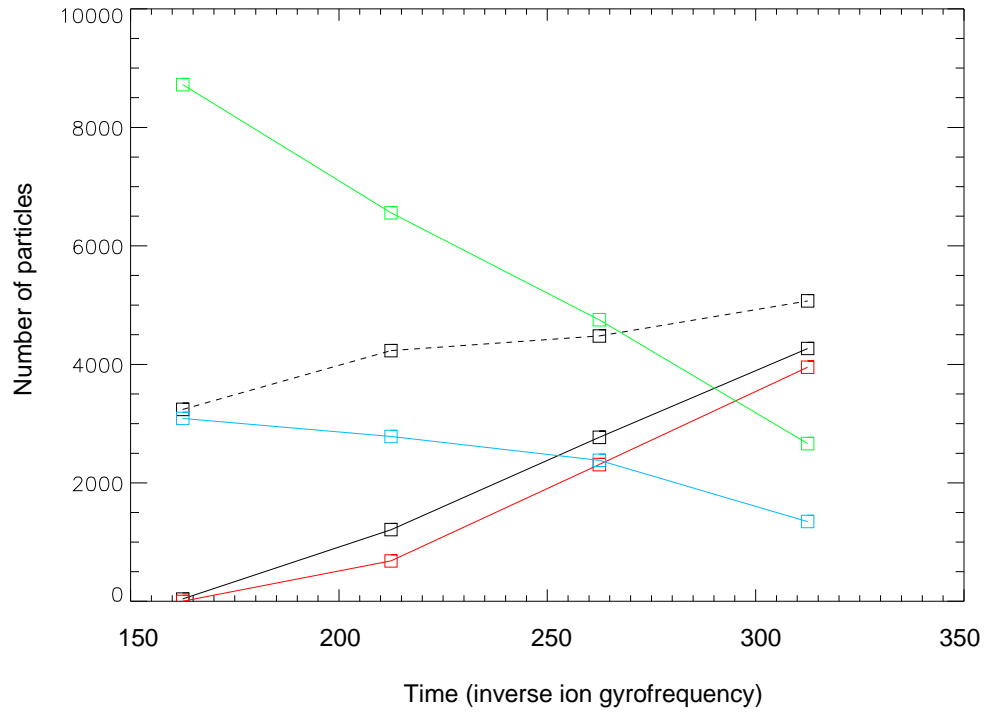
Figure 5.3: The graph presents the evolution of the particle number versus time. The colour refers to test particles with initial velocity located upstream (green), accelerated upstream (blue), downstream convected (bashed black), escaped on the LHS (black), and finally particles accelerated and escaped on the LHS (red). The unit of time is the inverse ion gyrofrequency (Ω_{ci}). The zero value of time marks the moment when the test particles have been released.

subject to scattering by waves and might be backscattered again to the shock where they can continue to move downstream or they can be injected into another acceleration process. The accelerated particles, especially particles with higher velocities, can propagate far from the shock into the upstream region and eventually might escape the system on the LHS of the simulation domain.

To summarize, the beam particles can:

1. leave the system on the LHS without being accelerated, i.e. without getting in contact with the shock

2. move downstream after crossing the shock

3. become accelerated at the shock and backscattered into the upstream region (these particles will have higher energies than before meeting the shock)

4. become accelerated at the shock, move far away from it into the region with small magnetic fluctuations and leave the system at the LHS

The advantage of such a simulation is that the beam particles can be followed in time, which provides the possibility to investigate the details of their behaviour. In data provided by spacecraft, the origin of the different ion populations cannot be determined through direct observation. Figure 5.3 shows that the total number of beam particles found in the upstream region decreases almost linearly with time together with beam particles which have been accelerated at the shock. On the other hand, the number of beam particles which moved downstream increases together with particles which have already left the system on the LHS. The LHS of the simulation domain is a free-escape boundary, beam particles reaching this far from the shock are removed from the system.

Figure 5.3 demonstrates the ratio of test particles found in different regions of the simulation box. After a time period of ~ 312 Ω_{ci}^{-1} ~ 42 % of the 12000 initially upstream-released beam particles have already moved downstream, ~ 22 % are to be found still in the upstream region, while ~ 35 % have left the system on the LHS. Taking into account only those particles which have been accelerated to a velocity of at least ~ 18.2 v_A (corresponding to the velocity of a 10 keV diffuse ion on spacecraft data) and which have escaped or are in the upstream region, we conclude that ~ 44 % of the beam particles have been accelerated at the shock and escaped the shock in the upstream direction.

In other words, based on the simulation result, ~ 44 % of the original field-aligned beam ions become diffuse ions after being scattered and accelerated at the shock. The high percentage suggests that the field-aligned beam ions might play an important role in the production of diffuse ions at the quasi-parallel shock.

Figure 5.4 shows the distribution of beam particles in $v_\perp - v_\parallel$ velocity space at different distances from the shock after 337 Ω_{ci}^{-1} from their release. At this time the shock was at $x \sim 1500$ λ_i. The foreshock region was divided into intervals of 250 λ_i. The panels show the distributions of the beam particles found in the respective interval. In every panel the particles are scattered in pitch angle along a circle. However, the amount of scattering differs substantially in each panel. The less scattered population is the farthest from the shock. Here all the particles have negative $v_\parallel$ values (i.e., they move towards the LHS boundary). As the distance to the shock decreases, the scattering becomes larger. In front of the shock the particles form an almost complete circle or narrow shell.

Especially in panel F, but also on panel E we can observe particles outside the scattering circle, most of them moving in the upstream direction. These are particles which have already reached the shock, were accelerated at the

shock and backscattered into the upstream region.

Note that on panel F among the particles situated on the circle, more particles have pitch angles close to 90 degree, and fewer have pitch angles close to zero. This shows the limitations of the quasilinear theory since it is assumed that every particle is scattered the same way irrespective of their pitch angle; in which case the distribution of particles over the scattering circe would be more isotropic. In order to describe more precisely the scattering process of the particles by waves an improved model is needed. These results show that the scattering efficiency over pitch angle might be a function of the pitch angle itself. This effect can be observed in every panel in Figure 5.4; however it is more obvious closer to the shock, where the magnetic wave energy is higher.

Another limitation of the quasilinear theory is that it does not explain the exponential growth of compressional waves in front of the shock. The compressional waves can be described as a periodical fluctuation of magnetic field intensity, which in fact forms a row of magnetic bottles. It is known that from the magnetic bottle only those particles can escape which have pitch angles less then the angle of the loss cone. Therefore the magnetic bottles are able to trap the particles very efficiently.
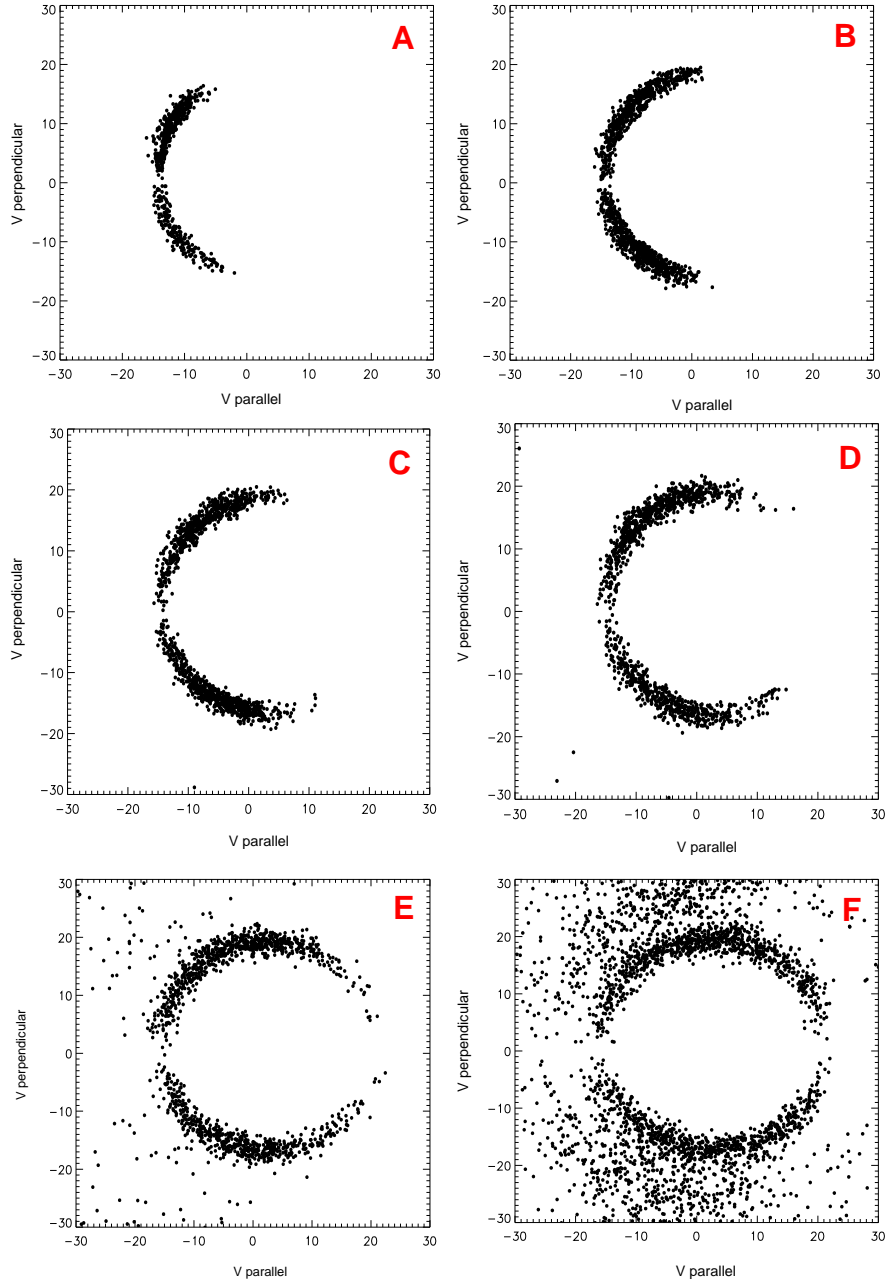
Figure 5.4: The beam particle distributions at different distances from the shock after 337.5 Ω_{ci}^{-1} from the release of beam particles in the upstream region. The letter A denotes the 0-250 λ_i interval, the farthest from the shock, while the letter F denotes the 1250-1500 λ_i interval, the region just in front of the shock; all the other letters are denoting succesively the other intervals.

Chapter 6

Summary

The Earth and its magnetosphere is immersed in the supersonic solar wind plasma flow. When the solar wind, which is a tenous, magnetised and collisionless plasma, reaches the magnetosphere of the Earth, a standing shock wave is generated. This is the bow shock of the Earth. At the bow shock the solar wind plasma is decelerated and heated, while its density and the magnetic field magnitude increases. The main challenge posed by the existence of a collisionless bow shock is to understand how the dissipation takes place in a practically collision-free medium, i.e., where the mean free path for Coulomb collisions is larger than the size of the system.

The region upstream of the Earth's bow shock is rich in wave and particle phenomena. The characteristics of these phenomena strongly depend on whether the region is magnetically connected to the quasi-parallel or to the quasi-perpendicular side of the bow shock (magnetic field-shock normal angle Θ_{BN} smaller or larger than 45°, respectively). In front of the quasi-parallel shock is the ion foreshock. The ion foreshock region is dominated by energetic ions with broad angular distributions. These so-called diffuse ions can have energies up to 200 keV and are accompanied by large-amplitude, low frequency waves.

The goal of this study was to provide a detailed analysis of the energetic ion behavior in the region in front of Earth's quasi-parallel bow shock, which was not possible until now. In order to achieve this goal we used the ion and the magnetic field data provided by the Cluster multispacecraft mission. Cluster provides for the first time simultaneous measurements with 4 spacecraft at different distances from the bow shock. Thus it becomes possible to separate spatial processes from temporal ones in the Earth's foreshock region. We have chosen two upstream ion events for our investigation: on 18 February, 2003 and on 07 March, 2003. The former is a high solar wind velocity event, while the latter is a medium solar wind velocity event. For both cases we demonstrated that the energetic ions undergo a diffusive transport in front of the quasi-parallel shock. The signature of the diffusive transport is the exponential decrease of the energetic ion partial density with distance from the shock along the magnetic field. The exponential dependence of the energetic ion partial density with distance from the shock has been previously demonstrated only indirectly on the basis of a statistical analysis of several upstream ion events from single-spacecraft data.

With the newly developed procedure (and with the Cluster multispacecraft data) we demonstrated for the first time from direct measurement that the energetic ion partial density gradient falls off indeed exponentially into the upstream direction. The new method also assures that the exponential slope of the energetic ion density in front of the shock is a spatial effect. Using the energetic ion partial density gradient values at different distances from the shock we calculated the e-folding distances in four ion energy ranges between 10-30 keV. The obtained e-folding distances in the case of the 18 February, 2003 upstream ion event are significantly smaller then the e-folding distances obtained from previous investigations based on statistical analysis. At the same time the e-folding distances in the case of the 07 March, 2003 upstream ion event are more comparable with the previously obtained re-

sults. This fact demonstrates that the e-folding distance heavily depends on the solar wind velocity. Using the gradient values we calculated the energetic ion scattering mean free path during the two upstream events and we found that the mean free path for the 30 keV ions is in both cases ~ 2.4 R$_e$. This shows that the mean free path does not depend on the solar wind velocity. In addition we calculated the diffusion coefficients at different ion energies and we found that in both cases the value of the diffusion coefficient is increasing with the ion energy. The diffusion coefficient values are the same for the 30 keV ions in both cases, however, at lower ion energies the diffusion coefficient values differ significantly.

Using the obtained diffusion coefficient value we calculated the time needed for a solar wind particle to reach an energy of 30 keV by acceleration at the shock. The acceleration time of t$\sim$120 seconds combined with the small mean free path value (~ 2.4R$_e$) shows that diffuse acceleration at the shock is unavoidable.

We extended the investigation of the 18 February, 2003 upstream ion event to cover also upstream ions with energies below 10 keV. In addition we investigated the upstream magnetohydrodynamic wave field during the same event. We studied in detail the Field-Aligned Beam (FAB) ion behavior in the upstream region. The FAB ion distribution, which consists of reflected solar wind ions at the quasi-perpendicular bow shock, was observed at different distances from the foreshock boundary; i.e., from the ion foreshock boundary deep into the foreshock region. The observations show how the initial beam distribution is scattered into an intermediate, and later into a toroidally gyrating ion distribution while part of the ions forming the original beam distribution are lost in the scattering process. This is due to the fact that the foreshock region acts as a velocity filter for the FAB and deep in the foreshock region only those FAB ions are to be found which acquired the largest pitch angles. On the other hand this also means that part of the

ions originally forming the FAB move to the shock and they can be involved in the acceleration process. These ions have a larger probability of getting involved in the acceleration process since they already have a larger energy compared with the solar wind ion energy. Therefore they might be additional seed particles for the diffuse ions.

The study also shows that the ion distribution observed by the spacecraft deeper in the foreshock region is in fact a superposition of reflected and diffuse ion distributions. Because of the convection of the magnetic field by the solar wind plasma the spacecraft observes ions coming from the quasi-parallel and the quasi-perpendicular side of the shock at the same time and at the same location. The fact that ions originating at different sides of the bow shock can be observed at the same location in the foreshock region points out that studying only the distribution of the ions is not sufficient. In order to have a correct interpretation of a distribution one needs to calculate the point of origin for different ions with different energies. Only this procedure combined with the distribution analysis is able to provide the correct interpretation of the ion data.

As we showed, part of the ions forming the FAB move to the shock where they can be further involved in a diffusive shock acceleration process. Ions cannot be tracked individually from spacecraft data: this is due to the fact that a spacecraft observes the ion population but it cannot provide direct information about the history of the particles, i.e., where are they coming from, in what processes were they involved, etc. In order to investigate in detail the behavior of the former FAB ions in the upstream region we used the hybrid simulation technique. We performed a 1D hybrid simulation where we used simulation parameters (i.e., the direction of the upsteam magnetic field and the solar wind velocity) which closely correspond to the parameter values observed during the 18 February, 2003 upstream ion event. After the shock and the upstream magnetic field was developed in a self-consistent way

(i.e., as a result of interaction between the particles and the electromagnetic field), we introduced in the simulation additional test particles with velocities corresponding to the velocity of the field-aligned beam particles. After their release we followed the beam (i.e., the test) particles individually until the end of the simulation. The result shows that more than 40% of the original FAB ions reach to the shock, become accelerated and move back into the upstream region with typical energies of diffuse ions. Thus the beam ions indeed are very efficiently accelerated at the shock and they might play an additional role in the production of diffuse ions.

Another important topic related to the foreshock region is the relation between magnetohydrodynamic waves and energetic particles. The waves scatter the energetic particles in pitch angle. On the other hand these waves are excited locally by the energetic ions; the intimate coupling between the waves and the particles is described in a model by Lee (1982). Previous observations showed that Lee's model describes in a satisfactory way the relation between the wave energy density and the energetic particle energy density. However, until now there has been no study which would investigate the predictions of Lee's model as a function of the distance from the bow shock. We investigated the relation between the predicted and the observed wave energy density and we found that at larger distances from the shock the model describes the observed wave energy in a satisfactory way. However, close to the shock the prediction of the model brakes down, since the observed wave energy density is an order of magnitude lower than the predicted one. At the same time the compressional wave energy density in front of the shock grows exponentially, a feature which can not be explained by Lee's model. At larger distances from the bow shock, where the compressional wave energy is small compared with the transverse one, the model describes the physical process apparently well. However, close to the shock where the compressional wave energy density becomes comparable with the transverse

wave energy density, a rather different physical process takes place: in this region the pitch-angle scattering does not dominate anymore, but rather the ability of the compressional waves to trap the energetic particles like a row of magnetic bottles. This highly compressive region in front of the shock can be regarded as part of the shock itself.

In order to investigate whether the observed exponential growth of the compressional waves is a characteristic feature of the quasi-parallel shock in general, we performed a wave analysis of the waves in the upstream region of the 1-D hybrid simulation. The exponential growth of the compressional wave energy density in the simulation demonstrates that this effect is indeed a characteristic feature of the quasi-parallel bow shock.

Acknowledgements

First I would like to thank Prof. Manfred Scholer and Dr. Berndt Klecker for being true "Doktorfathers" to me. They were always helpful and available; I could ask for any kind of advice, anytime. I also would like to thank Prof. Rudolf Treumann for his continuous support and encouragement. Frau Leistner and Hans Vaith helped me with the technical problems, Jasmine Zanker-Smith was the person to address with all kinds of other problems, a warm thank you for them. In fact every colleague at the Institut contributed to the birth of this thesis; Adrian Blagau, Dr. Octav Marghitu, Dr Matthias Förster, Dr. Frédéric Pitout, Dr. Stein Haaland and Edita Georgescu, thank you for your friendship. I thank Dr. Götz Paschmann for the conversations, Dr. Harald Kucharek for the remote assistance and Dr. Gyula Szokoly for the proofreading. And last but not least, I thank my family for the patience and support during these years.

Bibliography

[1] Armstrong, T.P., Pesses, M.E., Decker, R.B., 1985. Shock drift acceleration. In: Tsurutani, B.T., Stone, R.G. (Eds.), Collisionless Shocks in the Heliosphere: Reviews of Current Research, Geophysics Monography Series, Vol. 35. AGU, Washington, DC, 271.

[2] Asbridge, J.R., Bame, S.J., Strong, I.B., 1968. Outward flow of protons from the Earth's bow shock. J. Geophys. Res. 73, 5777.

[3] Axford, W.I., Leer, E., Skadron, G., 1977. The acceleration of cosmic rays by shock waves. Proc. Int. Conf. Cosmic Rays 15th, 11, 132.

[4] Axford, W.I., 1981. Acceleration of Cosmic Rays by Shock Waves. Proc. Int. Conf. Cosmic Rays 12th, 12, 155.

[5] Balogh, A., Dunlop, M.W., Cowley, S.W.H., Southwood, D.J., Thomlinson, J.G. et al., 1997. The Cluster Magnetic Field Investigation. Space Sci. Rev. 79, 65.

[6] Blandford, R.R., Ostriker, J.P., 1978. Particle acceleration by astrophysical shocks. Astrophys. J. 221, L29.

[7] Bonifazi, C., Moreno, G., 1981. Reflected and diffuse ions backstreaming from the Earth's bow shock, 1, Basic properties. J. Geophys. Res. 86, 4397.

[8] Burgess, D., 1989. Cyclic behavior at quasi-parallel collisionless shocks. Geophys. Res. Lett. 16, 345.

[9] Cornilleau-Wehrlin, N., Chauveau, P., Louis, S., Meyer, A., Nappa, J.M., Perraut, S., Rezeau, L., Robert, P., Roux, A., De Villedary, C., De Conchy, Y., Friel, L., Harvey, C.C., Hubert, D., Lacombe, C., Manning, R., Wouters, F., Lefeuvre, F., Parrot., M., Pincon, J.L., Poirier, B., Kofman, W., Louarn., Ph., 1997. The Cluster Spatio-Temporal Analysis of Field Fluctuations (STAFF) Experiment. Space Sci. Rev. 79, 107.

[10] Decker, R.B., 1983. Formation of shock-spike events at quasi-perpendicular shocks. J. Geophys. Res. 88, 9959.

[11] Décréau P.M.E., Fergeau, P., Krannosels'kikh, V., Lévêque, M., Martin, Ph., Randriamboarison, O., Sené, F.X., Trotignon, J.G., Canu, P., Mögensen, P.B., 1997. Whisper, a Resonance Sounder and Wave Analyser: Performances and Perspectives for the Cluster Mission. Space Sci. Rev., 79, 157.

[12] Domingo, V., Fleck, B., Poland, A.I., 1995. SOHO: The Solar and Heliospheric Observatory. Space Sci. Rev. 72, 81.

[13] Drury, L.O., 1983. An introduction to the theory of diffusive shock acceleration of energetic particles in tenuous plasmas. Rep. Prog. Phys., 46, 973.

[14] Ellison, D.C., 1981. Monte Carlo simulation of charged particles upstream of the Earth's bow shock. Geophys. Res. Lett. 8, 991.

[15] Escoubet, P.C., Schmidt, R., Goldstein, M.L., 1997. Cluster - Science and Mission Overview. Space Sci. Rev. 79, 11.

[16] Fairfield, D.H., 1969. Bow shock associated waves observed in the far upstream interplanetary medium. J. Geophys. Res. 74, 3541.

[17] Fairfield, D.H., 1971. Average and unusual locations of the Earth's magnetopause and bow shock. J. Geophys. Res. 76, 6700.

[18] Fairfield, D.H., 1974. Whistler waves observed upstream from collisionless shocks. J. Geophys. Res. 79, 1368.

[19] Forman, M.A., 1981. First-order Fermi acceleration of the diffuse ion population near the Earth's bow shock. Proc. Int. Conf. Cosmic Rays 17th, 3, 467.

[20] Forman, M.A., Drury, L.O., 1983. Time dependent shock acceleration: approximations and exact solutions. Proc. Int. Conf. Cosmic Rays 17th, OG 6-16, 267.

[21] Forman, M.A., Webb, G.M., 1985. Acceleration of energetic particles. In: Stone, R.G., Tsurutani, B.T. (Eds.), Collisionless Shocks in the Heliosphere: A Tutorial Review, Geophysics Monography Series, Vol. 34. AGU, Washington, DC, 91.

[22] Giacalone, J., Burgess, D., Schwartz, S.J., 1993. Ion injection and acceleration at parallel shocks: comparison of self-consistent plasma simulations with existing theories. Astrophys. J. 402, 550.

[23] Gosling, J.T., Asbridge, J.R., Bame, S.J., Paschmann, G., Sckopke, N., 1978. Observations of two distinct populations of bow shock ions in the upstream solar wind. Geophys. Res. Lett., 5, 957.

[24] Gosling, J.T., Thomsen, M.F., Bame, S.J., Feldman, W.C., Paschmann, G., Sckopke, N., 1982. Evidence for specularly reflected ions upstream from the quasi-parallel bow shock. Geophys. Res. Lett. 9, 1333.

[25] Greenstadt, E.W., Green, I.M., Inouye, G.T., Colburn, D.S., Binsack, J.H., Lyon, E.F., 1970a. Dual satellite observations of Earth's bow shock. I: The thick pulsation shock. Cosmic Elect. 1, 160.

[26] Greenstadt, E.W., Green, I.M., Inouye, G.T., Colburn, D.S., Binsack, J.H., Lyon, E.F., 1970b. Dual satellite observations of Earth's bow shock. II: Field-aligned upstream waves. Cosmic Elect. 1, 279.

[27] Greenstadt, E.W., Russell, C.T., Hoppe, M., 1980. Magnetic field orientation and suprathermal ion streams in the Earth's foreshock. J. Geophys. Res. 85, 3473.

[28] Greenstadt, E.W., 1985. Oblique, parallel, and quasi-parallel morphology of collisionless shocks. In: Tsurutani, B.T., Stone, R.G. (Eds.), Collisionless Shocks in the Heliosphere: Reviews of Current Research, Geophysics Monography Series, Vol. 35. AGU, Washington, DC, 169.

[29] Gurnett, D.A., Huff, R.L., Kirchner, D.L., 1997. The Wide-Band Plasma Wave Investigation. Space Sci. Rew. 79, 195.

[30] Gustafsson, G., Boström, R., Holback, B., Holmgren, G., Lundgren. A., Stasiewicz, K., Ahlén., L., Mozer, F.S., Pankow, D., Harvey, P., Berg, P., Ulrich, R., Pedersen, A., Schmidt, R., Butler, A., Fransen, A.W.C., Klinge, D., Thomsen, M., Fälthammar, C.-G., Lindqvist, P.-A., Christenson, S., Holtet, J., Lybekk, B., Sten, T.A., Tanskanen, P., Lappalainen, K., Wygant, J., 1997. The Electric Field and Wave Experiment for the Cluster Mission. Space Sci. Rew. 79, 137.

[31] Holzer, R.E., Slavin, J.A., 1978. Magnetic flux transfer associated with expansions and contractions of the dayside magnetosphere. J. Geophys. Res. 83, 3831.

[32] Hoppe, M.M., Russel, C.T., Frank, L.A., Eastman, T.E., Greenstadt, E.W., 1981. Upstream hydromagnetic waves and their association with backstreaming ions populations: ISEE-1 and ISEE-2 observations. J. Geophys. Res. 86, 4471.

[33] Hoppe, M.M., Russell, C.T., 1983. Plasma rest frame frequencies and polarizations of the low-frequency upstream waves: ISEE 1 and 2 observations. J. Geophys. Res. 88, 2021.

[34] Horbury, T.S. et al., 2001. Cluster magnetic field observations of the bow shock: Orientation, motion and structure. Ann. Geophys. 19, 1399.

[35] Ipavich, F.M., Galvin, A.B., Gloeckler, G., Scholer, M., Hovestadt, D., 1981. A statistical survey of ions observed upstream of the Earth's bow shock: Energy spectra, composition and spatial variations. J. Geophys. Res. 86, 4337.

[36] Johnstone, A.D., Alsop, C., Burge, S., Carter, P.J., Coates, A.J., et al., 1997. PEACE: a Plasma Electron and Current Experiment. Space Sci. Rew. 79, 351.

[37] Jokipii, J.R., 1982. Particle drift, diffusion and acceleration at shocks. Astrophys. J. 255, 716.

[38] Jokipii, J.R., 1987. Rate of energy gain and maximum energy in diffusive shock acceleration. Astrophys. J. 313, 842.

[39] Jones, F.C., Ellison, D.C., 1991. The Plasma Physics of Shock Acceleration. Space Sci. Rev. 58, 259.

[40] Krimigis, S.M., Venkatesan, D., Barichello, J.C., Sarris. E.T., 1978. Simultaneous measurements of energetic protons and electrons in the distant magnetosheath, magnetotail and upstream in the solar wind. Geophys. Res. Lett. 5, 961.

[41] Krimsky, G.F., 1977. A regular mechanism for the acceleration of charged particles on the front of a shock wave. Dokl. Akad. Nauk SSSR 234, 1306.

[42] Lee, M.A., Skadron, G., Fisk, L.A., 1981. Acceleration of energetic ions at the Earth's bow shock. Geophys. Res. Lett. 8, 401.

[43] Lee, M.A., 1982. Coupled hydromagnetic wave excitation and ion acceleration upstream of the Earth's bow shock. J. Geophys. Res. 87, 5063.

[44] Leroy, M.M., Goodrich, C.C., Winske, D., Wu, C.S., Papadopoulos, K., 1981. Simulation of a perpendicular bow shock. Geophys. Res. Lett., 8, 1269.

[45] Leroy, M.M., Winske, D., Goodrich, C.C., Wu, C.S., Papadopoulos, K., 1982. The structure of perpendicular bow shocks. J. Geophys. Res. 87, 5081.

[46] Leroy, M.M., 1983. Structure of perpendicular shocks in collisionless plasma. Phys. Fluids 26, 2742.

[47] Lin, R.P., Meng, C.-I., Anderson, K.A., 1974. 30- to 100-keV protons upstream from the Earth's bow shock. J. Geophys. Res. 79, 489.

[48] Lin, R.P., et al., 1995. A Three-dimensional Plasma and Energetic Particle Investigation for the Wind Spacecraft. Space Sci. Rev. 71, 125.

[49] Mattok, C. (ed.), 1995. Proceedings of the Cluster Workshop on Physical Measurements and Mission Oriented Theory. ESA SP-371.

[50] Möbius, E., Scholer, M., Sckopke, N., Lühr, H., Paschmann, G., Hovestadt, D., 1987. The distribution function of diffuse ions and the magnetic field power spectrum upstream of the Earth's bow shock. Geophys. Res. Lett. 14, 681.

[51] Ness, N.F., Scearce, C.S., Seek, J.B., 1964. Initial results of the IMP-1 magnetic field experiment. J. Geophys. Res. 69, 3531.

[52] Paschmann, G., Sckopke, N., Papamastorakis, I., Asbridge, J.R., Bame, S.J., Gosling, J.T., 1981. Characteristics of reflected and diffuse ions upstream from the Earth's bow shock. J. Geophys. Res. 86, 4355.

[53] Paschmann, G., Sckopke, N., 1983. Ion reflection and heating at the Earth's bow shock. In: Haerendel, G., Battrick, B. (Eds.), Topics in Plasma-, Astro-, and Space Physics. Max-Planck-Institut für Physik und Astrophysik, Garching, Germany, 139.

[54] Paschmann, G., et al., 1985. The Plasma Instrument for AMPTE IRM. IEEE Trans. Geosc. Remote Sens. GE-23, 262.

[55] Paschmann, G., Melzner, F., Frenzel, R., Vaith, H., Parigger, P., Pagel, U., Bauer, O.H., Haerendel, G., Baumjohann, W., Scopke, N., et al., 1997. The Electron Drift Instrument for Cluster. Space Sci. Rew. 79, 233.

[56] Peredo, M., Slavin, A., Mazur, E., Curtis, S.A., 1995. Three-dimensional position and shape of the bow shock and their variation with Alfvénic, sonic, and magnetosonic Mach numbers and interplanetary magnetic field orientation. J. Geophys. Res. 100, 7907.

[57] Rème, H., et al., 1987. The Giotto Electron Plasma Experiment. J. Phys. E: Sci. Instrum. 20, 721.

[58] Rème, H., et al., 2001. First multispacecraft ion measurements in and near the Earth's magnetosphere with the identical Cluster Ion Spectrometry (CIS) experiment. Ann. Geophys. 19, 1303.

[59] Riedler, W., Torkar, K., Rüdenauer, F., Fehringer, M., Pedersen, A., Schmidt, R., et al., 1997. Active Spacecraft Potential Control. Space Sci. Rew. 79, 271.

[60] Sarris, E.T., Krimigis, S.M., Armstrong, T.P., 1976. Observation of magnetospheric bursts of high-energy protons and electrons at $\sim$35 R$_{\rm E}$ with IMP 7. J. Geophys. Res. 81, 2341.

[61] Sarris, E.T., Krimigis, S.M., Bostrom, C.O., Armstrong, T.P., 1978. Simultaneous multispacecraft observations of energetic proton bursts inside and outside the magnetosphere. J. Geophys. Res. 83, 4289.

[62] Sckopke, N., Paschmann, G., Bame, S.J., Gosling, J.T., Russell, C.T., 1983. Evolution of ion distributions across the nearly perpendicular bow shock: specularly and nonspecularly reflected gyrating ions. J. Geophys. Res. 88, 6121.

[63] Scholer, M., Gloeckler, G., Ipavich, F.M., Hovestadt, D., Klecker, B., 1979. Pitch angle distribution of energetic protons near the Earth's bow shock. Geophys. Res. Lett. 6, 707.

[64] Scholer, M., Ipavich, F.M., Gloeckler, G., Hovestadt, D., 1980. Conditions for acceleration of energetic ions $\geq$30 keV associated with the Earth's bow shock. J. Geophys. Res. 85, 4602.

[65] Scholer, M., Ipavich, F.M., Gloeckler, G., Hovestadt, D., 1981. Simultaneous observations of energetic protons close to the bow shock and far upstream. J. Geophys. Res. 86, 186.

[66] Scholer, M., 1985. Diffusive acceleration. In: Tsurutani, B.T., Stone, R.G. (Eds.), Collisionless Shocks in the Heliosphere: Reviews of Current Research, Geophysics Monography Series, Vol. 35. AGU, Washington, DC, 287.

[67] Smith, C.W., L'Hereux, J., Ness, N.F., Acuna, M.H., Burlaga, L.F., Scheifele, J., 1998. The ACE Magnetic Field Experiment. Space Sci. Rev. 86, 613.

[68] Sonnerup, B.U.Ö., 1969. Acceleration of particles reflected at a shock front. J. Geophys. Res. 74, 1301.

[69] Spreiter, J.R., Summers, A.L., Alksne, A.Y., 1966. Hydromagnetic Flow Around the Magnetosphere. Planet. Space Sci. 14, 223.

[70] Spreiter, J.R., Alksne, A.Y., Summers, A.L., 1968. External aerodynamics of the magnetosphere. Carovillano, R.L. (Ed), Physics of the Magnetosphere. Springer-Verlag, New York, 301.

[71] Thomsen, M.F., 1985. Upstream suprathermal ions. In: Tsurutani, B.T., Stone, R.G. (Eds.), Collisionless Shocks in the Heliosphere: Reviews of Current Research, Geophysics Monography Series, Vol. 35. AGU, Washington, DC, 253.

[72] Trattner, K.J., Möbius, E., Scholer, M., Klecker, B., Hilchenbach, M., Lühr, H., 1994. Statistical analysis of diffuse ion events upstream of the Earth's bow shock. J. Geophys. Res. 99, 13389.

[73] Wilken, B., Axford, W.I., Daglis, I., Daly, P., Güttler,W., et al., 1997. RAPID. The Imaging Energetic Particle Spectrometer on Cluster. Space Sci. Rew. 79, 399.

[74] Wilkinson, W.P., Schwartz, S.J., 1990. Parametric dependence of the density of specularly reflected ions at quasi-perpendicular collisionless shocks. Planet. Space Sci. 38, 419.

[75] Woolliscroft, L.J.C., Alleyne, H.ST.C., Dunford, C.M., Sumner, A., Thompson, J.A., et al., 1997. The Digital Wave-Processing Experiment on Cluster. Space Sci. Rew. 79, 209.

Lebenslauf

von

Árpád Kis

Geburtsdatum	30. Mai, 1969
Geburtsort	Cluj (Klausenburg, Kolozsvár), Rumänien.
Nationalität	Ungarisch
Familienstand	verheiratet

Schulbildung

1975-1979 Grundschule, Scoala Generala Nr15, Cluj, Rumänien.

1979-1987 Gymnasium, Liceul Mat-Fiz Nr3 Cluj-Napoca, Rumänien.

1987 Diplom "Bacalaureat" Abschlussnote: 7.39 (Bewertungsskala:1-10), Hauptfächer: Mathematik, Physik, Literatur und Praktisches Training als Mechaniker.

Hochschulausbildung

1994-2001 MSc in Geophysik, Eötvös Universität, Budapest, Ungarn
Betreuer: Prof. Dr. Csaba Ferencz

2002-2005 Max-Planck-Institut für extraterrestrische Physik, Garching, Deutschland, Doktorand

2002-2005 Promotionsstudium an der Fakultät für Geophysik der Ludwig-Maximilians-Universität München